

Copyright

by

Jameson Parker Gips

2014

**The Thesis Committee for Jameson Parker Gips
Certifies that this is the approved version of the following thesis:**

Shale Characterization Using TGA, Py-GC-MS, and NMR

**APPROVED BY
SUPERVISING COMMITTEE:**

Supervisor:

Mukul M. Sharma

Hugh Daigle

Shale Characterization Using TGA, Py-GC-MS, and NMR

by

Jameson Parker Gips, B.S. Ch.E.

Thesis

Presented to the Faculty of the Graduate School of

The University of Texas at Austin

in Partial Fulfillment

of the Requirements

for the Degree of

Master of Science in Engineering

The University of Texas at Austin

December 2014

Dedication

To my best friend and wife, Colleen.

Acknowledgements

This work is the accumulation (and the omission) of a great deal of work performed by a great number of people. It started on a very hot June day while working on a completely unrelated project, and wouldn't be possible without the guidance and wisdom of Dr. Sharma. He mentioned the sheer lack of adequate measurements that could be performed on shales, and its huge potential effect on the valuation of shale plays and the companies involved in them. He gave me a list of petrophysical measurements (producibile oil in place, saturation, and porosity) and said if I could find a way to accurately measure just one of these, it would be sufficient work for a PhD. Foolishly, I decided to attempt all three.

There were a number of very important people involved throughout the research and writing process. Qiang Liu and Benny Freeman are responsible for introducing TGA to the shale group, as well as running a number of samples. Jin Lee has graced the building with friendliness, and made procuring services and parts simple. Evan Gilmore has been a wonderful sounding board for ideas both good and bad. Chang Min Jung, Junhao Zhou, Wei Wei Wu, Pratik Kakkar, and Peng Zhang have all made our shale group seem more like a group of friends than research team. Rod Russel has rotated between mentor, reading group leader, master experimentalist, shop mechanic, and most importantly, friend. Dr. Hugh Daigle has offered support above and beyond the call of duty. He's given me advice, knowledge, read a number of my papers, and encouraged me to publish a paper. I'm truly grateful and consider him a friend. Lastly and most importantly, my wife Colleen has read and grammar nazi'd every word I've written in the

past two years, put up with late nights at the lab and writing, and has given me more emotional support than I can imagine. Thank you dear, and I love you more than anything.

Abstract

Shale Characterization Using TGA, Py-GC-MS, and NMR

Jameson Parker Gips, M.S.E.

The University of Texas at Austin, 2014

Supervisor: Mukul M. Sharma

Many of the current analytical techniques originally developed to characterize conventional reservoir rocks and fluid cannot adequately measure shale and source rocks. An example of this is Retort, where it is not feasible to get sufficient fluid from source rock to make useful measurements. The primary interest of this thesis is the exploration of other analytical techniques, two of which are previously unused in the oil and gas industry. These are Thermal Gravimetric Analysis (TGA), Pyrolysis-Gas Chromatography-Mass Spectrometry (Py-GC-MS), and Nuclear Magnetic Resonance (NMR).

The techniques proposed offer valuable insight into the properties of the rock. TGA gives accurate weight of a sample as temperature is increased, Py-GC-MS is useful for identifying exact molecules in vaporized fluid, and NMR can be used to characterize viscosity and hydrocarbon chain length. The methods using these techniques can be utilized to further confirm mineralogy of a sample, identify the fluid constituents and quantify their weight, analyze changes in a sample between two different states, and calculate the free fluid saturations of oil and gas in shales. Procedures and results for each of these are presented in this thesis to show methodology and give the reader an idea of its useful applications.

Table of Contents

Table of Contents	viii
1 Introduction.....	1
1.1 Background and Motivation.....	3
1.2 Research Objective.....	4
1.3 Overview of Chapters.....	5
2 Thermal Gravimetric Analysis (TGA).....	6
2.1 Introduction to Thermal Gravimetric Analysis	6
2.2 Pyrolysis-Rock-Evaluation.....	6
2.3 TGA Basics	9
2.3.1 General Method Explanation	9
2.3.2 Description of Various Thermal Events	15
2.3.3 The Effects of Clays on TGA Signals.....	19
2.4 Qualitative Analysis of Various Shales using TGA.....	20
2.4.1 Experimental Procedure.....	21
2.4.2 Identification of Optimized Sample Size.....	23
2.4.3 Comparison of TGA Results to XRD Mineralogy	28
2.5 Quantitative Analysis using TGA	34
2.5.1 Estimation of Carbonate Content.....	35
2.5.2 Estimation of Free Fluid Content.....	38
2.5.3 Estimation of Overall Free Fluid Content by Subtracting Clays	41
2.6 TGA Conclusions.....	46
3 Pyrolysis-Gas Chromatography-Mass Spectroscopy (Py-GC-MS).....	47
3.1 Py-GC-MS Basics	47
3.1.1 Procedure for Linking Py-GC-MS with TGA to Get Vaporized Fluid Concentration Relative to the Overall Sample Size.....	49
3.2 Py-GC-MS Results for Multiple Temperature Steps	52
3.2.1 Results and Discussion	52
3.3 Conclusions	55
4 Nuclear Magnetic Resonance (NMR).....	57
4.1 Introduction	57
4.1.1 Governing Physics	57
4.1.2 Use of NMR in Unconventionals.....	66
4.1.3 “Single-Scan” vs. “Multi-scan” NMR Techniques.....	69

4.2	Characterizing Fluids in Shales with NMR and Py-GC-MS	70
4.2.1	Experimental Method.....	72
4.2.2	Experimental Results and Discussion.....	76
4.2.3	Conclusions.....	83
5	Using Multiple Techniques for Petrophysical Calculations in Shales.....	84
5.1	Py-GC-MS to Determine Producing Fluid Saturations.....	84
5.1.1	TGA and Low Temperature Range Selection.....	84
5.1.2	Py-GC-MS and Conversion to wt. %.....	85
6	Conclusions.....	90
	Appendices.....	93
	A1: Hydrocarbon Boiling Points	93
	A2: Structures of Gibbsite and Silica Sheets and The Arrangement for Different Clays	97
	A3: TGA Results for All Shales	99
	A4: TGA results for clay combinations	104
	A5: NMR – Temperature Step T ₁ & T ₂ 2D-Maps	105
	Bakken	106
	Eagle Ford.....	109
	Utica.....	113
	References.....	117

1 Introduction

The rise of unconventional resources in the United States has been rapid in the last several years. Shale plays that were completely ignored only a decade ago are now the new frontier for both oil and gas production. Global demand for energy is rising at a rapid pace, and is greater than 500 quadrillion BTUs, and shales are expected to become a large contributor of the energy supply. Gas from shales represented only 16% of production in the U.S. in 2009, but is expected to increase to 47% by 2035 (Energy Information Administration (EIA), 2009). This represents a major change in the projections of hydrocarbon production in the U.S., which conventionally showed a steady decline with no major upticks. This trend has been bucked, with oil and gas production surging domestically, leading many to call it the “Shale Revolution.” This is displayed superbly in Figure 1.1, showing the rapid increase in crude oil production due to shales in the lower-48. One of the greatest implications may be the reduction in the import of foreign energy into the country, which has consequences globally, as the U.S. will be less reliant on oil production from the Middle East. Figure 1.2 shows this drastic change in recent years and a projection into the future by the EIA.

Shale plays exist throughout the world, and are expected to play an increasingly important role to satisfy increasing energy demand. One of the primary problems with projecting the production from shale plays, however, is understanding the basic petrophysics associated with them. Even the most basic figures, such as the amount of original oil in place (OOIP), and concentrations of oil and water (oil and water saturations) are elusive.

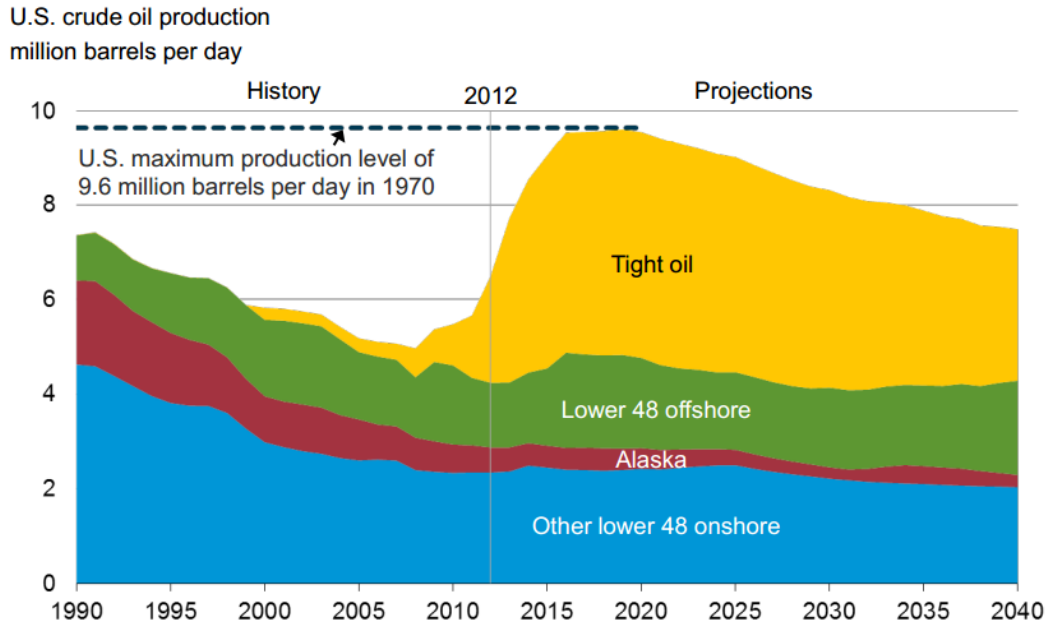


Figure 1.1: U.S. petroleum fuels by source (EIA, Annual Energy Outlook 2014 Early Release)

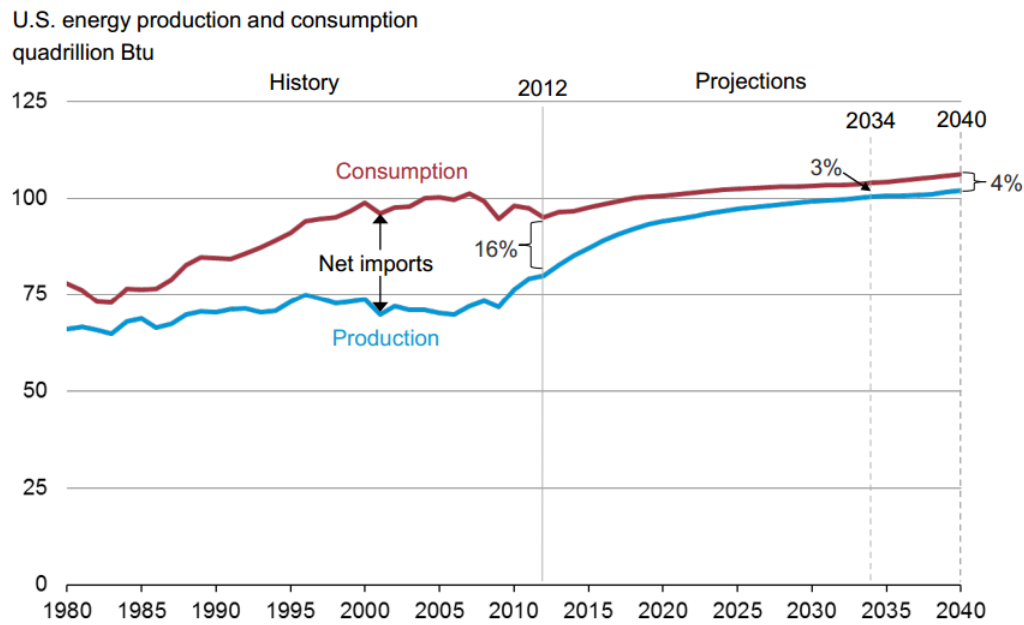


Figure 1.2: U.S. energy production and consumption (quadrillion BTUs) (EIA, Annual Energy Outlook 2014 Early Release)

1.1 Background and Motivation

The determination of oil and water saturations and OOIP has been performed empirically using core samples for many years. This is often a simple task for conventional reservoirs, and can easily be measured in the lab at the macro scale. These techniques include (but are not limited to):

1. Retort – The thermal heating of large core plugs, distilling the vaporized fluid, and then measuring the quantity of fluid compared to the overall volume of the sample.
2. Rock Pyrolysis Evaluation – This is also a method utilizing thermal heating of a core sample. However, the vaporized fluid is analyzed as it evolves using a Flame Ionization Detector (FID).

With the dramatically lower permeability and porosity in shales, conventional lab techniques often prove to be useless. This is especially true in the case of retort, where the amount of time it would take for all of the producible fluid to permeate through the sample and be collected is on the order of weeks, and the amount would be too small to offer a reliable measurement (Hardwerger, 2012). Another issue with this technique lies in the fact that much of the hydrocarbon mass in shales is still contained in kerogen and bitumen. Allowing heating to take place for this long would allow substantial amounts of kerogen to mature which would distort the measurement of vaporized liquid.

Rock-Pyrolysis-Evaluation (Rock-Eval) is more promising in that very small, crushed samples can be utilized. Additionally, the amount of hydrocarbon expected to be producible can be calculated based on temperature! At first glance, Rock-Eval seems to

be the ideal solution. However, on closer inspection, one finds that the primary issue with the method is that it misses other component pieces, namely the amount of water. Rock-Eval utilizes a flame ionization detector which is only capable of measuring organics. Additionally, newer models of Rock-Eval machines may contain infrared detectors to accurately detect the amount of carbon dioxide generated from carbonate decomposition (Vinci Rock-Eval Manual, 2009). Overall, the method is quite powerful for determining currently producible and potential hydrocarbons in the formation, but not for determining saturations, or characterizing the type of hydrocarbon itself. Therefore, it is necessary to find methods and techniques capable of providing this information.

1.2 Research Objective

Thus, the objective of this work is to explore new geochemical analytical techniques in order to provide a better understanding of some of the basic petrophysical parameters which govern the production of hydrocarbons from shales. Specifically, the techniques addressed in this thesis have the following objectives:

1. Determine the amount of producible oil in a given core sample of shale or tight rock.
2. Determine the oil and water saturations of the free fluid (producible fluid).
3. Estimate the porosity (free and bound) of the rock sample
4. Characterize the producible fluid.

1.3 Overview of Chapters

The following chapter introduces an analytical technique that has not been applied to the analysis of even conventional rock, Thermal Gravimetric Analysis (TGA). It begins by explaining its basic processes and comparing it to a similar technique already used in the industry, Pyrolysis-Rock-Evaluation. From there we show the various thermal events that can affect TGA signals and then show several methods of both qualitative and quantitative analysis that can be performed utilizing this data.

The third chapter introduces Pyrolysis-Gas Chromatography-Mass Spectrometry, a method useful for identification of molecules vaporized from the rock sample. Here again, we discuss the basic technique, and then a method of analysis for utilizing the data as well as potential uses for it.

The final technique we discuss is Nuclear Magnetic Resonance (NMR), which needs no introduction. A discussion of the governing physics of NMR is followed by its use in both conventional and unconventional reservoir evaluation. Then, a “proof of concept” is shown utilizing NMR to characterize fluid changes in the rock, and its potential application in laboratory use.

The fifth chapter details a method in which both TGA and Py-GC-MS can be utilized together to calculate oil and water saturations in the free fluid portion of shales. As far as we know, this has not been done before in shales.

Lastly, we go over some of the conclusions of this work and compare it to the research objectives. Additionally, we look at where the technology may best be utilized and what future work may be most beneficial.

2 Thermal Gravimetric Analysis (TGA)

2.1 Introduction to Thermal Gravimetric Analysis

Thermal gravimetric analysis (TGA) is a method in which a small crushed sample between 10 and 50 mg in size is heated at a continuous rate over time and is precisely weighed throughout the experiment. The derivative of the weight as it changes over temperature can then be calculated and analyzed. This method is desirable for several key reasons. First, the sample size required for a single test is very small (less than 1 g) and can be repeated many times without using up substantial amounts of core. Second, it is relatively cheap, fast, and automated, again allowing for multiple tests to be performed at relatively low cost. Third, and most important, is the quantitative data that is generated. The information can be used to quantify the amount of free fluid in the sample, utilized to determine hydrogen and oxygen indices if total organic carbon (TOC) is known, and can help to identify mineralogy or confirm it from other sources. Additionally, the mass data can be paired with other analytical methods which identify chemical compounds to yield the chemical composition of the fluid that has been volatilized from the sample. Most TGA machines are precise to ± 0.001 mg throughout the entire temperature range; therefore with proper calibration, the technique renders very accurate, precise, and repeatable results with very little error.

2.2 Pyrolysis-Rock-Evaluation

The method is similar to Rock-Pyrolysis-Evaluation (Rock-Eval), a classical method for evaluating source rocks which is commonly used to measure hydrogen index, oxygen index, and kerogen maturity. Both techniques continuously heat the rock in an

oxygen free environment, and the analysis relies on assigning what material is volatilizing based on temperature.

The most useful information that can be generated from rock-eval is the overall hydrocarbon potential of the rock, hydrogen and oxygen indices. Figure 2.1 shows an example readout from rock-eval. The middle curve, showing S₁, S₂, and S₃, is comparable to the derivative curve in TGA, in that the area under it corresponds to mass. One problem with this method, however, is that this curve must be calibrated to represent mass, whereas in TGA mass is directly measured. The S₁ peak is the theoretical maximum amount of hydrocarbon that exists in free pore space per mass of rock sample. S₂ represents the pyrolysis of kerogen to other hydrocarbons, and S₃ is the release of trapped CO₂ from the oxidation of the kerogen. Together, S₂ and S₃ could give hydrogen and oxygen indices respectively when divided by the total organic content of the sample, as shown in the equations section of Figure 2.1. Lastly, the location of the peak of S₂, often called T_{max}, gives a relative indicator of the maturity level of the kerogen. If the peak is further to the left, it is more immature and thus has more hydrocarbons to expel than one with a peak further to the right.

The primary difference between the two techniques is the manner in which the measurement is performed. Rock-eval utilizes flame ionization detectors and thermal conductivity detectors (FID & TCD, respectively) to selectively measure the hydrocarbons, CO₂, and CO throughout the temperature range. This has shortcomings and pitfalls, namely that the calibration for the entire calculation method is only valid for most machines up to a mineral carbon concentration of 12 wt. % (Vinci Rock-Eval 6 Manual, 2009). This means that if carbonates are present in large quantities, they are

often indistinguishable from kerogen as they register in the CO₂ release in S₃. It is only recently that rock-eval machines are capable of determining the difference between “pyrolyzable carbon,” or that associated with kerogen, and “mineral carbon” associated with carbonates. Even the newest techniques still have difficulty making this determination in formations with high dolomite concentrations.

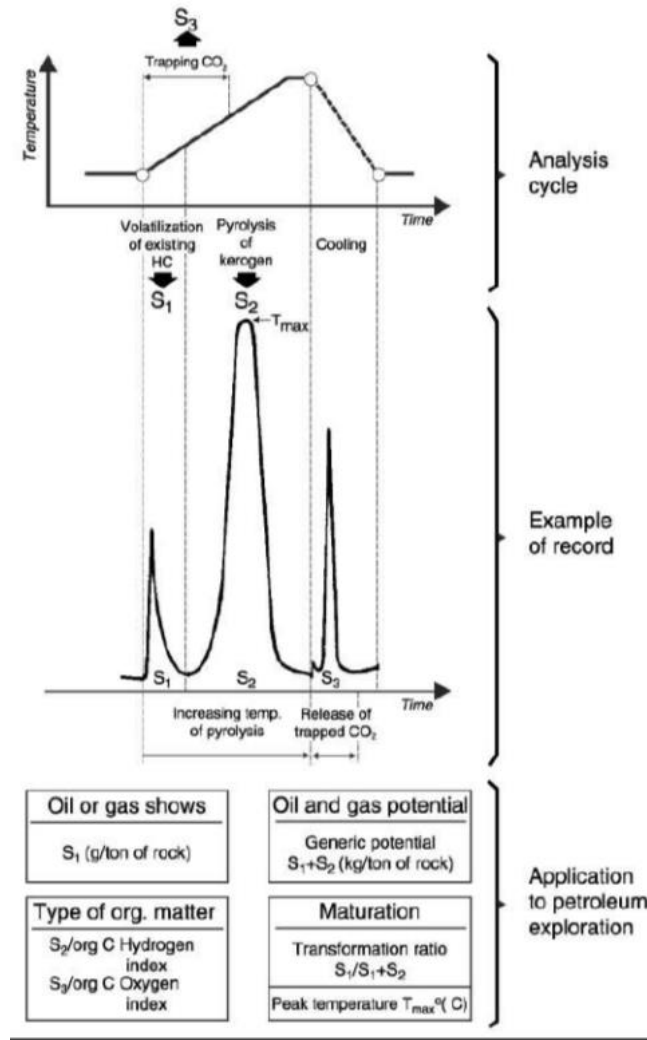


Figure 2.1: Example record of Pyrolysis-Rock-Evaluation, and how it is interpreted (Jarvie, 2001)

There are additional problems associated with the calibration and utilization of the FID and TCD without knowing the exact hydrocarbon components that will be

volatilized. The TGA, however, simply weighs the sample directly, allowing for very reliable data.

Another advantage of TGA is its potential for use in the field. The footprint and weight of the machine is quite minimal (2 ft² and 100 lbs, respectively), it is quite easy to operate, and requires only a small mass of crushed sample. Therefore, it is quite conceivable that a portable TGA for use on drill cuttings could provide valuable information using otherwise discarded samples for a relatively low cost.

2.3 TGA Basics

2.3.1 General Method Explanation

Specifically, the crushed sample is placed in a highly calibrated pan made of suitable inert material (quite often platinum). The pan is certified from the manufacturer to not change in weight over the entire range of temperatures used in the machine, which is often 1000° C or greater. Diligence in transferring the sample is important to reduce the free vaporization of fluids from the sample during this time, although this is quite minor compared to the overall fluid volatilized during the heating process. Tweezers are used to transfer the sample to avoid adding or removing material from the sample. Sample preparation is an important component in these tests, and specific techniques used are discussed in detail in Section 2.4. One important note is the use of preserved core. The core storage technique plays a critical role in these tests as the free water and hydrocarbons can readily vaporize in ambient conditions. Thus, properly storing the core (and preparing it for the experiment) should involve minimal exposure to air and keeping the core pieces in a humidity controlled environment.

The pan with the sample is placed over a hook which is attached to a high precision scale, responsible for weighing the sample throughout the process. This is directly above the heating chamber, which consists of electrical heating coils, ceramic insulation, and a metal cover. Additionally, the top ring of the chamber is exposed ceramic and forms a sealing surface with ceramic on the underside of the scale. Figure 2.1 and Figure 2.2 show this in greater detail. By manual or automated means, the entire chamber raises up around the pan and hook and completely encloses them. The chamber is then purged with inert gas at a low flow rate to eliminate any oxygen in the apparatus (Figure 2.2).

Data recording begins shortly thereafter with a constant inert purge flowing through the chamber. At this point, the user executes a usually pre-programmed test routine which changes the temperature at various rates and the type of purge gas.

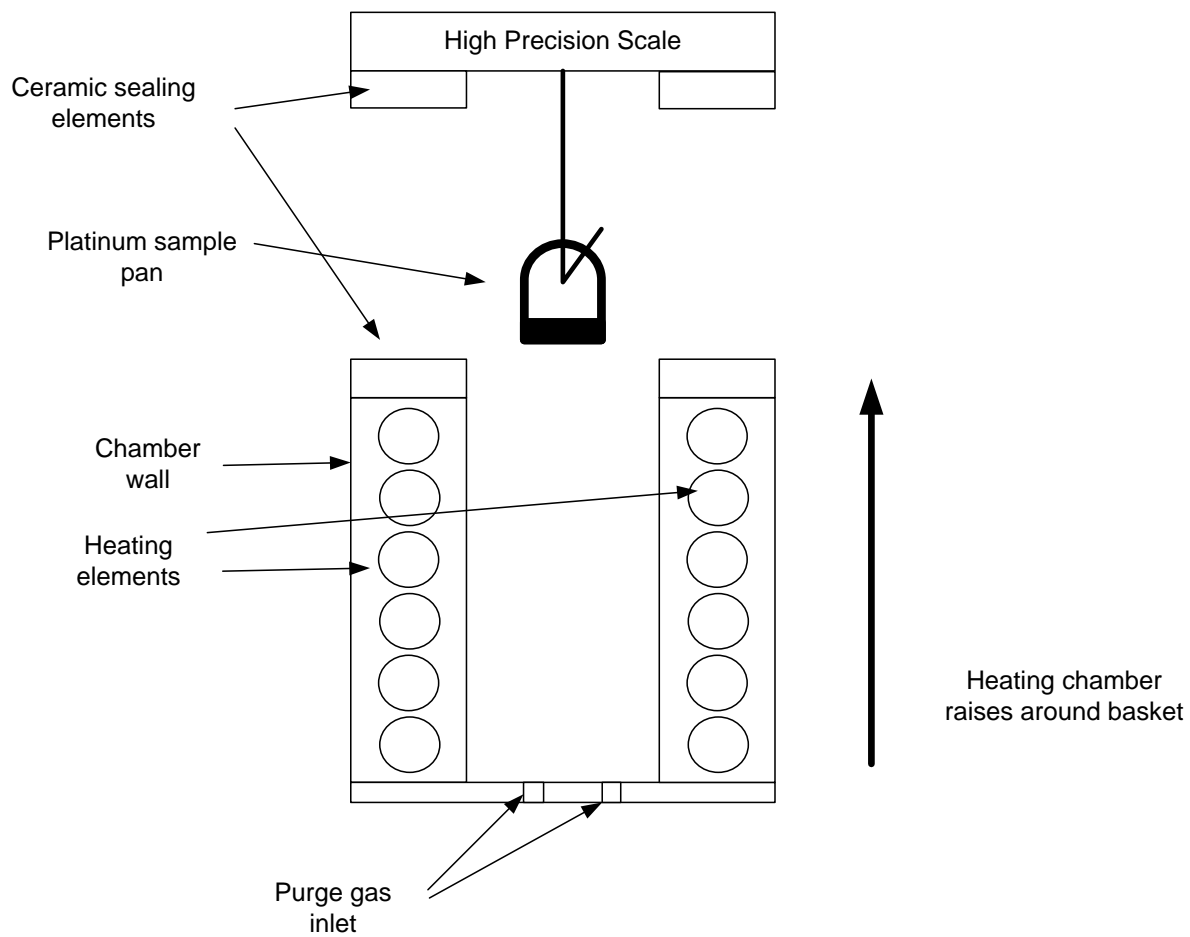


Figure 2.2: Diagram of TGA apparatus

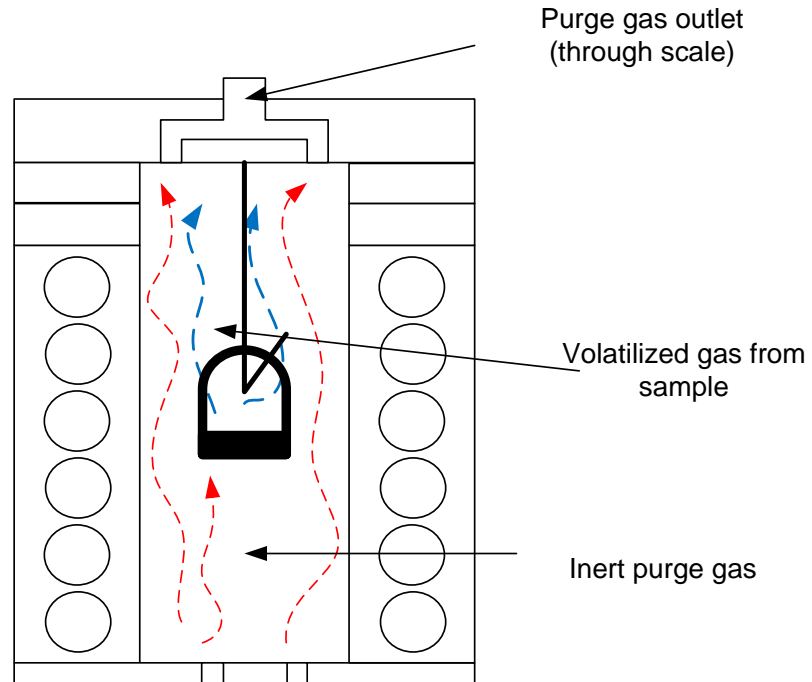


Figure 2.3: Diagram of TGA apparatus in operation

The data recovered from the test is a plot of the exact weight and temperature of the sample as a function of time. Quite often, temperature is set to increase constantly with time, and therefore, the weight of the sample can be measured as a function of temperature itself; this was done with all experiments in this work and is illustrated in Figure 2.3.

The rate of heating plays an important role because time can play a significant role in the mechanics of when the fluid vaporizes, leaves the sample, and thus is no longer being weighed. This is especially true in the case of carbonate decomposition and kerogen maturation, where the limiting factor is driven by reaction kinetics and a molecule's proximity to void pore space where it can freely move out of the sample. Ideally, the kinetic based effects can be minimized by simply reducing the rate of temperature increase over time. However, this has the unfortunate side-effect of causing

the experiment to take extremely long times to complete. The amount of time for a molecule to move out of the way of other molecules using the same "access routes" of the voided pore space can be minimized by making the surface to volume ratio of all components of the rock larger. This is done effectively in bulk by simply crushing the sample material to the smallest size possible. This too has drawbacks. As the sample mesh size gets smaller, it begins to resemble less and less the in-situ state of the rock in terms of fluid content, distribution of minerals, etc. It is beyond the scope of this paper to go into this in great detail, but this work assumes that larger sample pieces are more indicative of in situ conditions.

Since both of these actions have serious consequences, experiments were performed to optimize both temperature rate and sample grain size. This is shown in greater detail in Section 2.3.2.

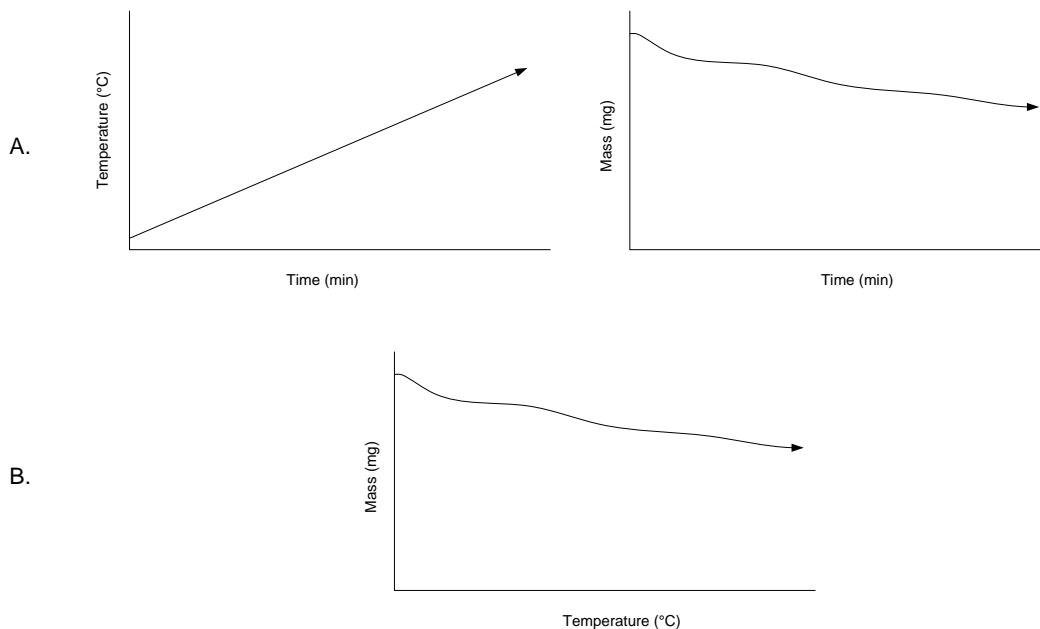


Figure 2.4: A) Typical TGA output where sample temperature and mass must be shown separately or on different scales B) If temperature is increased linearly with time, temperature itself can stand as the X-axis and be directly related to mass

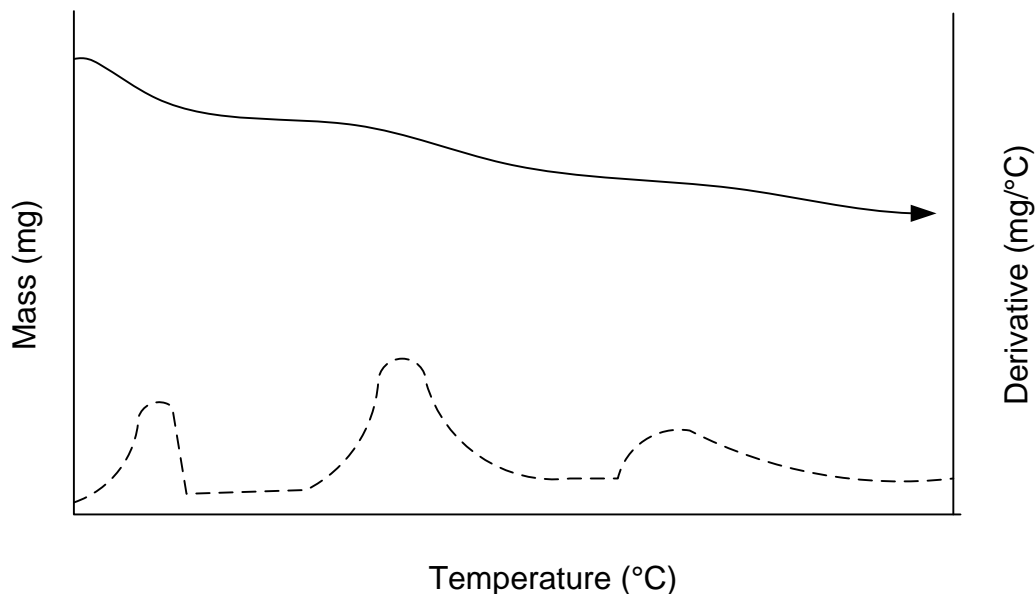


Figure 2.5: Illustration of TGA output with calculated derivative

Analysis of the sample can then be performed by taking the derivative of the sample weight with respect to time or temperature. This derivative for each point along the curve is given by Equation 2.1:

$$D_i = -\frac{M_{i+1} - M_i}{T_{i+1} - T_i} \quad (2.1)$$

Where D is the derivative in mg/°C, M is the mass of the sample in mg, and T is the temperature of the apparatus in °C.

This results in a new curve which can be placed on the same chart as the mass, and can be used for further analysis. The area underneath the derivative curve represents the total mass loss, and the peaks represent the local maxima for where mass loss was at its greatest. This is illustrated in Figure 2.4. Each peak, inflection point, or other type of

change in the derivative represents a thermal event. This term will be used to describe the various processes that occur within a set temperature range. For example, the vaporization of free fluid such as oil or water at the lowest temperatures peaks at around 100°C, and then the derivative would fall back to zero once it has all been vaporized, thus representing a single thermal event.

2.3.2 Description of Various Thermal Events

There are a number of processes that take place throughout a single TGA run, the simplest being the vaporization of free fluid shown above, and the most complicated being multi-hydrocarbon reactions at higher temperatures. In general, they can be divided into several categories: 1) the vaporization of free fluids, 2) the vaporization of clay-bound fluids, 3) the degradation of clays, 4) the decomposition of carbonates, and 5) the maturation of more viscous organics (kerogen & bitumen). Table 2.1 shows a list of the various processes and the temperature ranges in which they can occur.

Event Description	Temperature Range
Vaporization of free water	30° - 100° C
Vaporization of producible hydrocarbons*	30° - 175° C
Vaporization of clay-bound fluids	65° - 150° C
Vaporization of medium viscosity (non-producible) hydrocarbons	100° - 215° C
Degradation of kaolinite, illite	500° - 550° C
Degradation of chlorite	580° - 625° C
Degradation of smectite	700° - 800° C
Decomposition of siderite	425° - 520° C
Decomposition of dolomite	625° - 720° C
Decomposition of calcite	780° - 840° C
Kerogen and bitumen pyrolysis	>350°

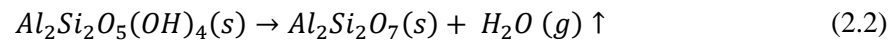
Table 2.1: Various thermal processes and their respective temperature range. *Note: A full list of hydrocarbons considered for this range and their respective boiling points can be found in the appendix.

Free water and oil begin to vaporize immediately into the chamber even at lower temperatures and continue all the way to their respective boiling points. Producible hydrocarbons are assumed to be chain lengths of 5-21 carbon atoms, with the vast majority being toward the shorter end. The maximum temperature for the range in which they vaporize was estimated after seeing many TGA runs, all of which show the derivative peak dropping sharply or returning to zero before 175°C. Many long chain hydrocarbons with boiling points much greater than this have been identified to exist in the pore space of these samples; however, they are in sufficiently small quantities to be negligible.

Vaporization of clay-bound fluids mainly refers to water trapped between layers of montmorillonite and mixed-layer clays. This dehydration of the clay occurs at a higher temperature than free water due to the strong attraction between the water molecules and

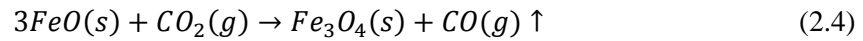
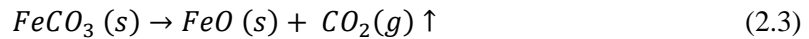
the clay layers. The structures of the gibbsite and silica sheets and their arrangements for the various clays can be found in Appendix 2. Santos et al. noted that by simply changing the portions of the clay content, the temperature for the peaks of dehydration and degradation can change dramatically (Santos et al., 1997). This in general was not observed throughout our experiments, and the dehydration peak was often quite isolated within a range of 100°-200°C.

Clay degradation is referred to by many terms: loss of crystalline water, interstitial water dehydration, dehydroxylation, and more. This work specifically refers to the loss of covalently bonded OH ions to the crystalline structure of the octahedral sheet for all of these terms. This chemical reaction is shown in Equation 2.2.



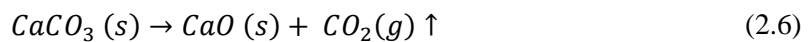
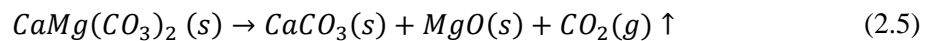
This reaction occurs for all clays but at different temperatures. It occurs first for kaolinite and illite around 500°C, chlorite around 580°C, and smectite at nearly 700°C (Santos et al., 1997). It should be noted, however, that the dehydration of the clay-bound water previously mentioned is a much more prominent TGA peak for swelling clays.

The decomposition of carbonates is typically at the higher end of the temperature spectrum (>550° C). One noticeable exception is the case of siderite, which can begin to pyrolyze as low as 400°C but is often observed in the range of 425°-520°C. Siderite is uncommon among most carbonate sequences, but is found more commonly in source rocks (Vinci Rock Eval 6 Manual, 2009), and therefore, its presence cannot be discounted. It observes a sequence of reactions under pyrolysis which is characterized by:



The first process, shown by Equation 2.3 begins at 400°C, and the second, shown by Equation 2.4 takes place at approximately 850°C. However, the second does not occur in the case of TGA as all of the carbon dioxide gas released in the first reaction is swept by purge gas out of the chamber.

Dolomite, the second most prevalent carbonate, also undergoes a two-stage decomposition: first the release of magnesium oxide and CO₂ leaving only calcite, and then the complete decomposition of calcite itself. These occur at around peak temperatures of 650°C and 820°C, respectively. Unlike siderite, both of these reactions are observed in TGA and are characterized by the following equations:



Calcite, often the most dominant form of carbonate, is characterized by only the reaction described by Equation 2.5 and shows as a single peak around 800°C. Calcite, dolomite, and siderite have signals that can readily be identified by TGA in isolation, and

sketches of these signals are shown in Figure 2.6. Unfortunately, they are rarely observed in isolation in source rocks and are overlapping with various other thermal events.

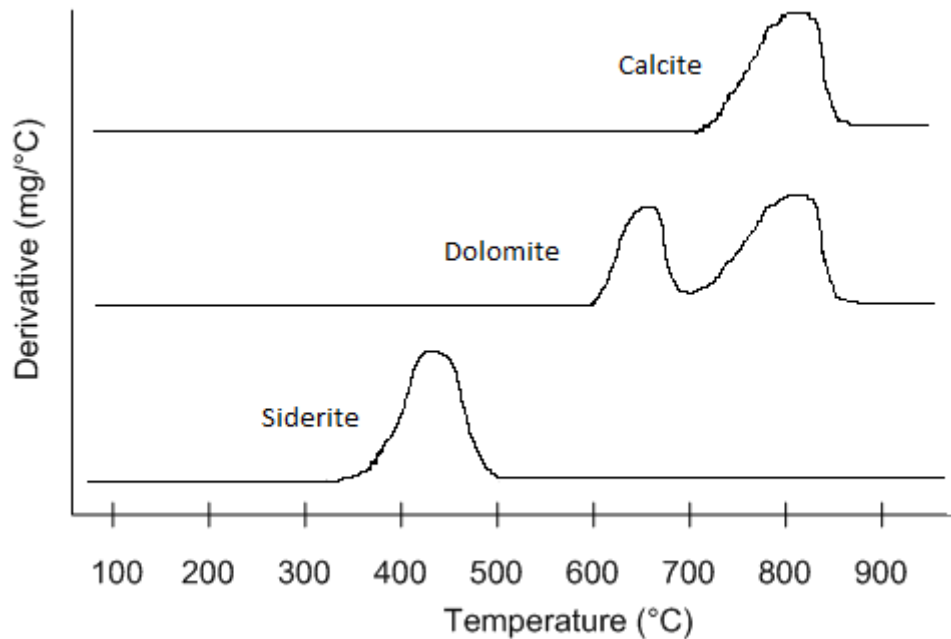


Figure 2.6: Typical TGA signatures for calcite, dolomite, and siderite

2.3.3 The Effects of Clays on TGA Signals

Like carbonates, clays can be readily recognizable in a TGA signal if they are isolated, and they exhibit very predictable signatures. This is noted in Santos et. al., and Figures 2.6 and 2.7 below show the use of TGA to identify the type of clay content within non-source rock shales (Santos et al., 1997). Additionally, free vs. interlayer water can be readily identified via the shape of the very first curve. With much of the free water evaporating at $\sim 30^{\circ}\text{C}$, a small inflection (or sometimes a very large one) will occur from 60° - 110°C . However, quantification of the two is still difficult from this method.

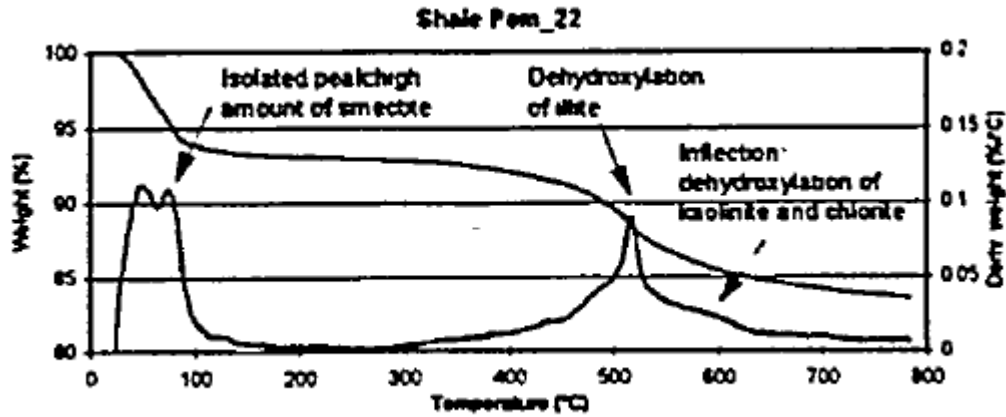


Figure 2.7: TGA showing difference between free and interlayer water (Santos, 1997)

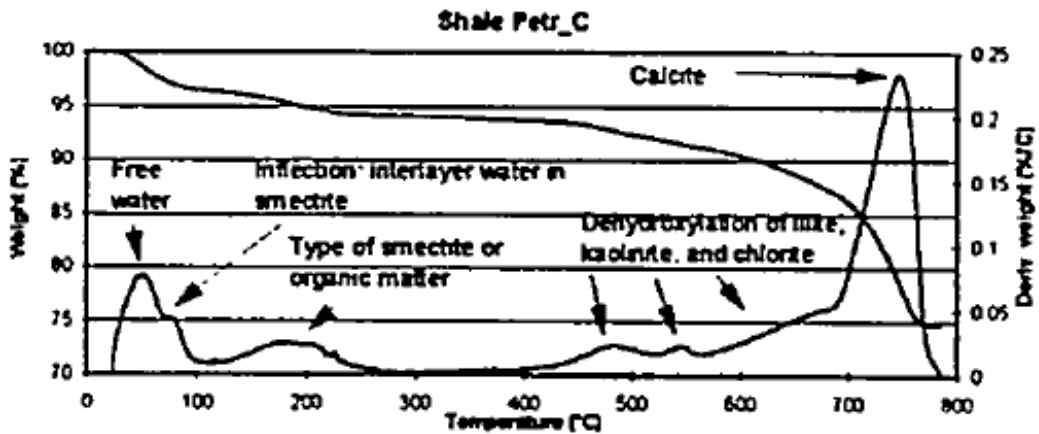


Figure 2.8: TGA showing free water, interlayer water, dehydroxylation of all clay types, and calcite decomposition

2.4 Qualitative Analysis of Various Shales using TGA

Several preserved shale samples were selected to be analyzed with TGA qualitatively and then compared with other characterization techniques in order to determine the usefulness of the technique. The shales selected were the Eagle Ford in the “oil window” (and is thus expected to have abundant longer chain hydrocarbons), Utica in the gas window, and then the middle Bakken (a non-source rock, but still tight) sample. The samples were compared to XRD mineralogy results. Another goal of these

experiments was to optimize the two factors controlling the accuracy and length of a single TGA run, the sample mesh size and heating rate.

2.4.1 Experimental Procedure

Sample Preparation

Preparing a single sample for a TGA run consists of the following steps:

1. Select ~100 g of sample pieces from preserved core.

Note: These pieces will preferably be from fully preserved core still encased in wax from when it was first extruded. An alternative acceptable storage method is keeping the shale in mineral oil. However, this is less preferable and requires drying the sample pieces with hydrocarbon solvent. All samples prepared in Section 2.3 of this thesis are directly from the wax-encased core.

2. Place sample pieces in sealed plastic bag, and crush.
3. Pour crushed pieces into sieve and separate to the desired mesh size.

Note: For our samples, a mesh size between 0.6-1.0 mm was chosen based on testing detailed in Section 2.4.2.

4. Place the adequately sized pieces into a sealed container (a small 4 mm vial was used), and place the larger pieces back into the bag used for crushing.
5. Repeat steps 3 and 4 until no large pieces of sample are remaining.
6. Place the small container with the adequately sized pieces in a humidity - controlled desiccator based on native water activity experiment for the given shale (Zhou, 2013). The container should be left open to the desiccator humidity.

7. Allow the samples to equilibrate to the native humidity state for 48 hours. This allows the shale to regain water that may have been lost during the crushing process.
8. Remove the sample from the desiccator, and immediately cap/seal the container leaving minimal headspace. In all cases, the sample was analyzed via TGA within 48 hours after removing from the desiccator.

TGA Heating Procedure

As previously mentioned, the TGA procedure can be pre-programmed to follow a series of changes in heating rate and purge gas. The following procedure represents the optimized program based on experiments detailed in Section 2.3.

1. Load ~50 mg of crushed sample into the platinum pan using tweezers (this is approximately 5-10 pieces of 0.6-1.0 mm sample)
2. Place pan onto loading station and immediately run TGA
3. TGA Program
 - a. Start purge gas: nitrogen @ 40 mL/min
 - b. Raise heating chamber
 - c. 10 min: Allow sample to equilibrate @ 30°C controlled temperature
 - d. Ramp temperature @ 10°C/min to 1100°C

Note: Some samples shown are heated only to 1000°C for time savings, as data above this temperature is of little use for analysis.

- e. Hold temperature @ 1100°C, switch purge gas to air for 30 min @ 40 mL/min

Note: The purpose of this step is to burn off any residue that may be remaining on the pan.

- f. Reduce temperature to ambient
- g. Lower heating chamber, remove sample remnants

2.4.2 Identification of Optimized Sample Size

The ideal sample mesh size was ascertained by running different sizes using the TGA procedure outlined in Section 2.3.1 and then identifying the largest sample mesh size that still had identifiable derivative peaks. Only the middle Bakken sample was used for this experiment due to resource limitations. For more thorough analysis, it is highly recommended to perform this optimization for each formation.

The mesh size ranges tested were 0.106-0.177 mm, 0.177-0.600 mm, 0.600-1.000 mm, 1.000-1.180 mm, and 1.180-1.440 mm. The results of these tests are shown in Figure 2.9. The 0.106-0.177 mm and the 0.177-0.600 mm mesh sizes do not show the initial drop which exists in the three larger mesh sizes. It is believed that this is due to the sample being crushed so greatly that all fluid that could readily be volatilized at room temperature did so during the crushing process. Additionally, the first peak on both of the smallest mesh sizes is considerably smaller than for the 0.600-1.000 mm mesh size. This further implies that with smaller mesh sizes, a greater amount of the free fluid is lost in sample preparation than with larger mesh sizes. In fact, the 0.106-0.177 mm and 0.177-0.600 mm mesh sizes are almost identically shaped throughout the entire derivative curve, with the smallest mesh size having slightly smaller peaks. Another small

difference is a small peak that appears around 940°C on the 0.177-0.600 mm mesh size. This extra peak is at such a high temperature that it is typically ignored for analysis.

The 0.600-1.000 mm mesh size was chosen as optimal as it still retains the entirety of the curve detail of the smallest mesh sizes, but still includes the initial drop of the largest two mesh sizes. The largest two, the 1.000-1.180 mm and 1.180-1.440 mm mesh sizes are very similar in overall weight loss, indicating that there is no component discriminately left out from the samples. However, they show less precise peaks, and the weight loss is spread out over a greater range of temperatures, making identification of components much more difficult. This is shown exceptionally well with the 1.180-1.440 mm sample as the inflection point ranging from 400°-600°C observed in every other TGA signal appears to be just part of the larger carbonate peak.

After these tests, the 0.600-1.000 mm mesh size was chosen as the ideal mesh size for further sample preparation.

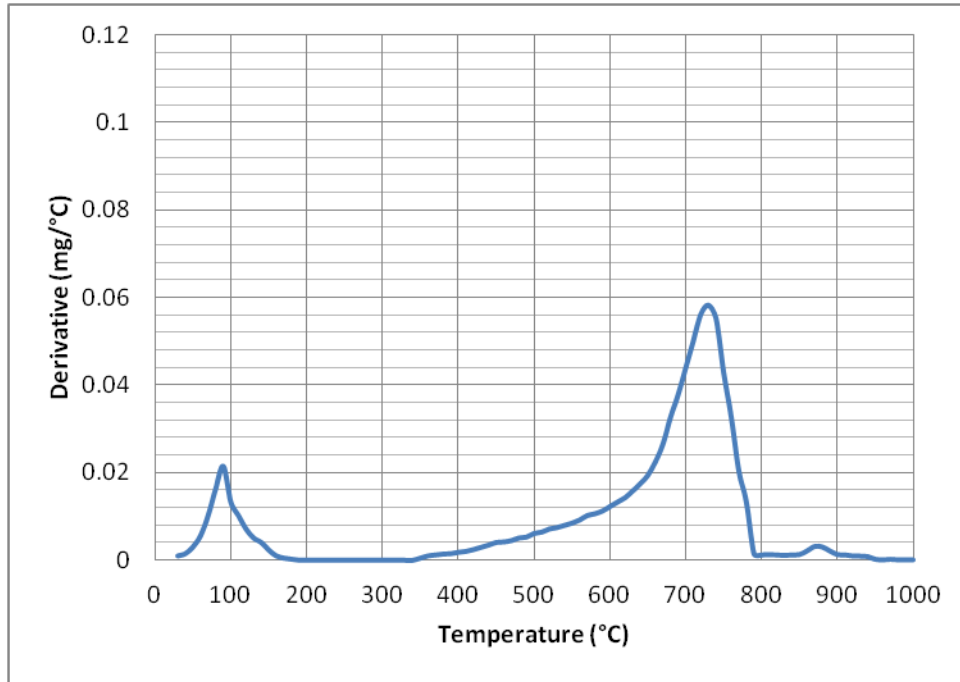


Figure 2.9: Derivative analysis of 0.106-0.177 mm mesh size

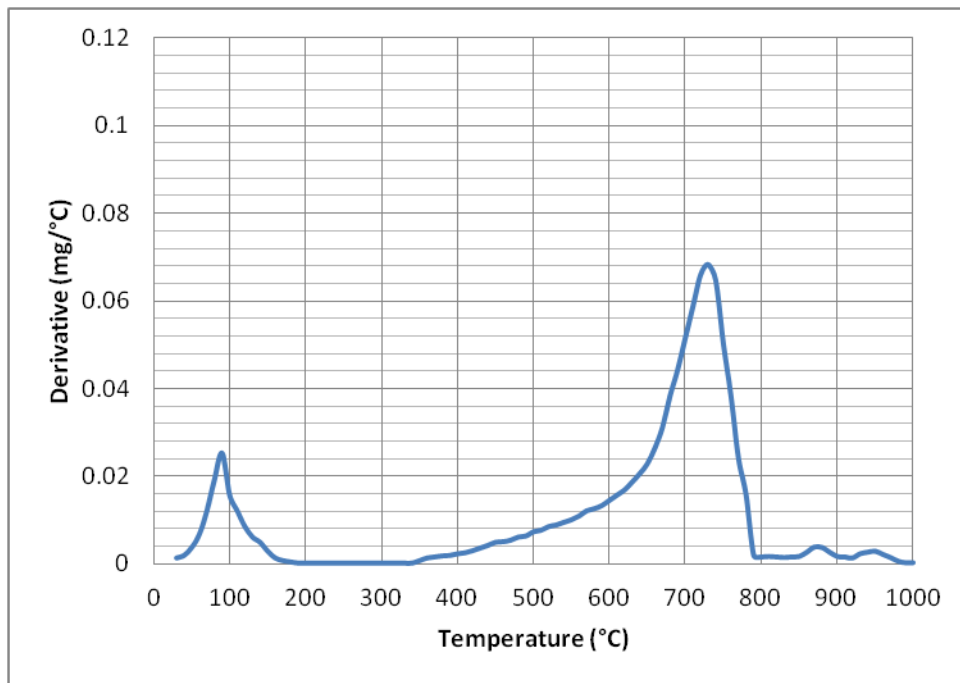


Figure 2.10: Derivative analysis of 0.177-0.600 mm mesh size

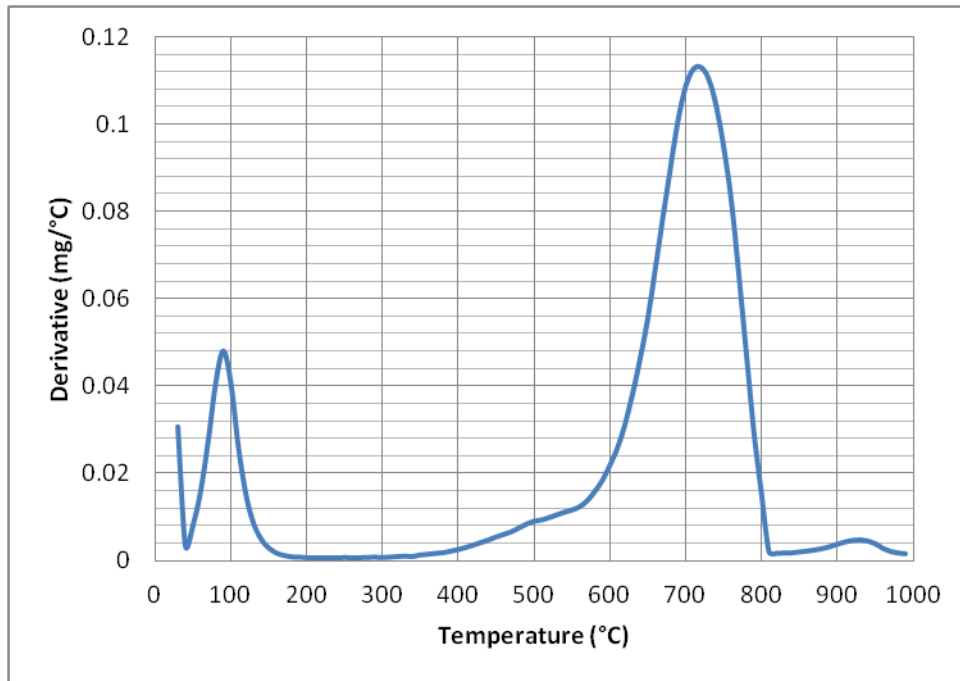


Figure 2.11: Derivative analysis of 0.600-1.000 mm mesh size

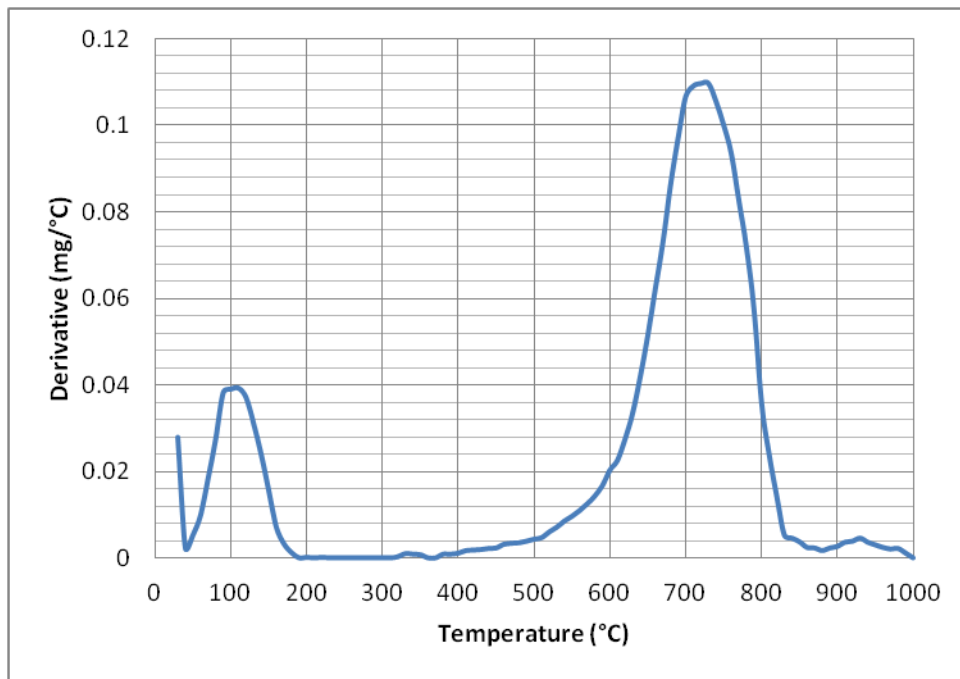


Figure 2.12: Derivative analysis of 1.000-1.180 mm mesh size

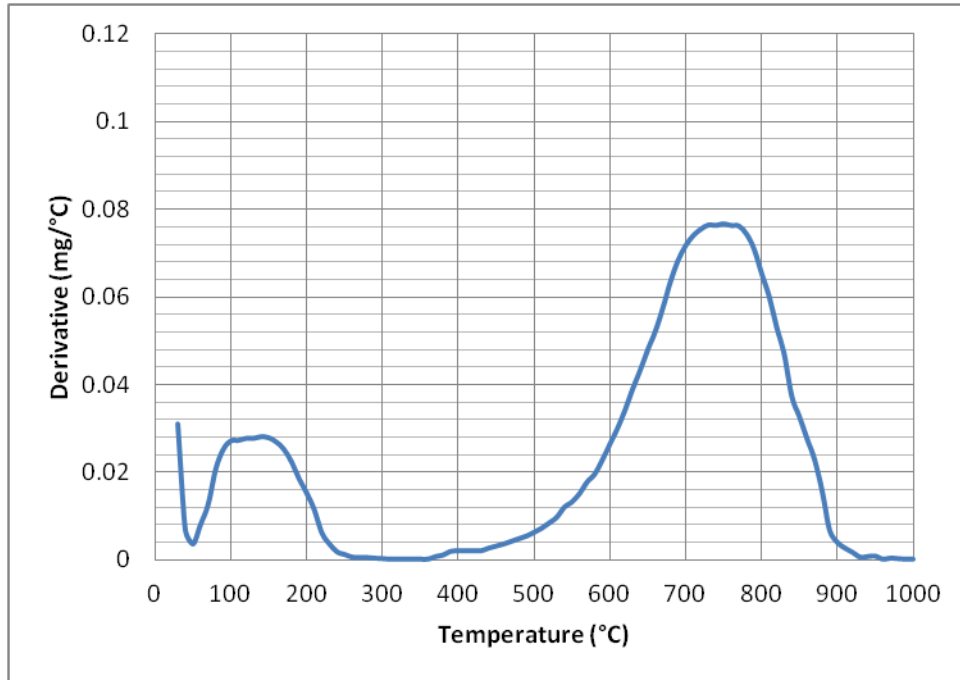


Figure 2.13: Derivative analysis of 1.180-1.144 mm mesh size

2.4.3 Comparison of TGA Results to XRD Mineralogy

This thesis focuses on analyzing the results from three key unconventional resource plays: the Bakken, Eagle Ford, and Utica. However, TGA was performed on seven separate resource plays, and the results are shown in Appendix 3. The Bakken, Eagle Ford, and Utica are notably different in mineralogy and organic content, thus providing an excellent opportunity to analyze and compare the TGA results to those of different analytical techniques, in this case, X-ray diffraction. Table 2.2 shows the mineralogy of the three samples.

	Bakken	Eagle Ford	Utica
Quartz	23%	8%	26.5%
Calcite	8.6%	50.1%	10.7%
Dolomite	20%	0%	5.2%
Smectite	1%	5.7%	8.1%
Illite	8.7%	7.3%	6.1%
Kaolinite	7.1%	5.7%	7.2%
Other	19.6%	23.2%	36.2%

Table 2.2: Mineralogy in wt% of Bakken, Eagle Ford, and Utica samples as determined by XRD by CoreLab in Houston, TX

Some things to point out about this data is that the Bakken sample is rich in dolomite and has very little swelling clays as indicated by the smectite; this would translate to a lower temperature for the carbonate peak, and a very small or completely missing peak for the clay-bound liquids peak in the lower temperatures. The Eagle Ford has a large concentration of calcite with no dolomite present, and has nearly six times the

swelling clay content of the Bakken. The Utica has significantly less carbonates than both the Bakken and Eagle Ford, which should be indicated by a smaller peak in the 700°-800°C range on the TGA. Additionally, the Utica has the largest smectite concentration of the three. Also of note is the concentration in the "other" category. These are largely non-pyrolyzable minerals such as pyrite and are not expected to contribute to TGA results.

Figure 2.14 shows the TGA and derivative peaks for the middle Bakken sample. It shows no sign of an additional peak or inflection point for the clay-bound water, which would be expected to be around 110°C. The free fluid peak does overlap this area, and allows the possibility of at least a small amount of clay-bound fluid. However, due to the small concentration of swelling-clay from XRD, the TGA peak seems to be accurate. The inflection from 400°-600°C is indicative of multiple events, including maturation of organics, and the degradation of illite and kaolinite.

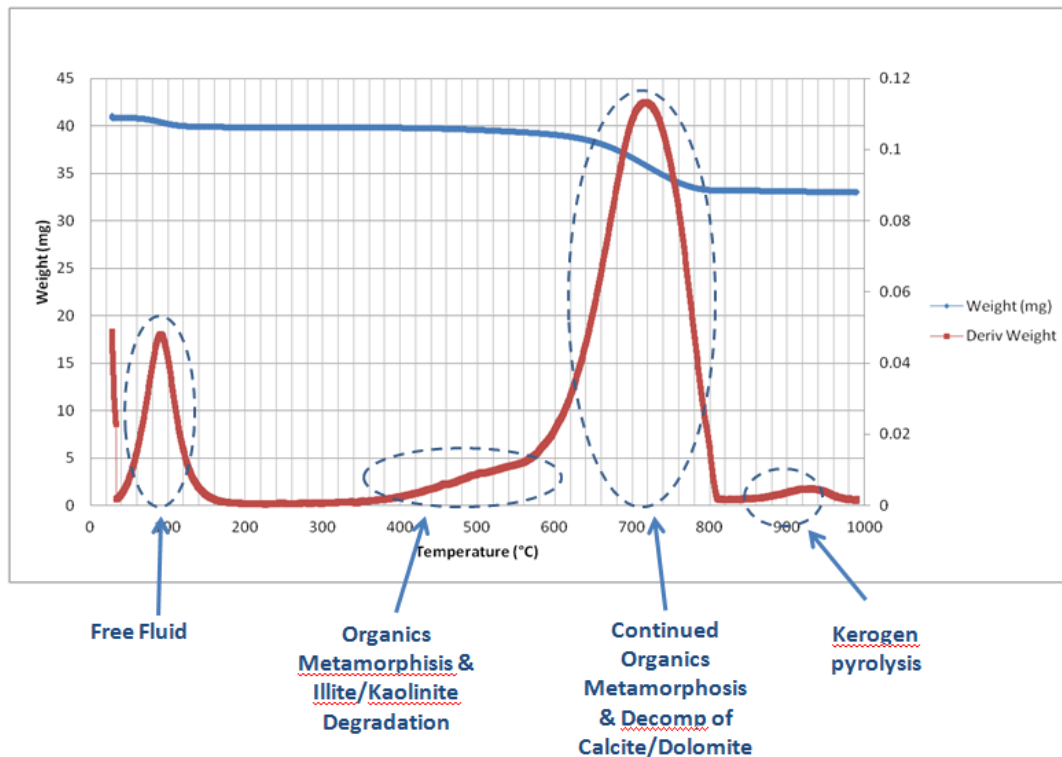


Figure 2.14: TGA and derivative peaks of the Bakken sample with explanations of peaks

The carbonate peak ranges from 600°-840°C and is at its maximum at 720°C. This can be explained by the large dolomite concentration, which alone will have two separate peaks around 650°C and 840°. In fact, a small inflection point around 800°C can be seen in this chart, indicating the decomposition of calcite. The fact that the peak appears as one singular curve is probably indicative of other, longer lasting events taking place. It is expected that this is due to the continued maturation of hydrocarbons. It should be pointed out that while the middle Bakken is not a source rock and kerogen is not expected, very thick, long-chained hydrocarbons can most certainly be present. They can further mature and “thermally crack,” exhibiting similar thermal events as kerogen and bitumen. Lastly, the small peak at 940°C is likely the decomposition of quartz.

However, as mentioned before, at these extreme temperatures a number of reactions can take place, and thus their peaks are difficult to analyze.

The Eagle Ford, however, is a true source rock as it contains the original organic matter from which oil and gas is produced. The TGA results are shown in Figure 2.15, and show a much smaller free fluid peak at the lowest temperatures. This is expected to contain much of the oil and water that would be producible in a hydraulically fractured reservoir. Additionally, the Eagle Ford exhibits a separate peak at about 140°C which is representative of both the clay-bound fluid as well as the remaining producible hydrocarbons, which probably had too high of a boiling point for the first peak, thus the peak at 140°C rather than 110°C. Also shown is a small peak at 540°C, probably the decomposition of siderite mixed with the beginnings of kaolinite and illite decomposition as well as organics maturation. The inflection point leading up to the carbonate peak is most likely the continued clay decomposition as well as organics metamorphosis. Also of note is the singular, sharp carbonate peak right at 830°C. This is confirmation of the existence of very little to no dolomite, with a very large amount of calcite (from XRD, the sample is 50% calcite).

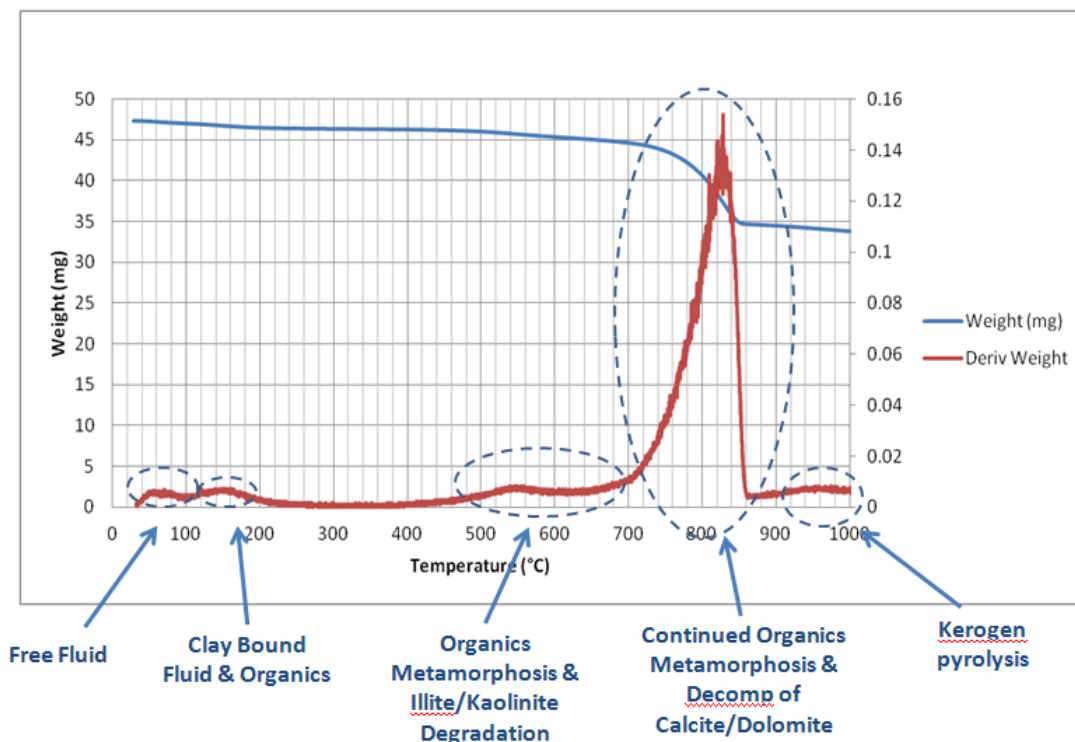


Figure 2.15: TGA and derivative peaks of the Eagle Ford sample with explanations of peaks

Lastly, the Utica sample is shown in Figure 2.16. Its results are similar to the Eagle Ford in that there are two peaks at the lower temperatures, indicating the existence of clay-bound fluid, and possibly thicker but still producible hydrocarbons. It is interesting to note, however, that although the Utica showed a higher amount of swelling clay in the sample, the clay-bound fluid peak is relatively lower than with the Eagle Ford. Explanations for this include the possibility of less medium-chain length hydrocarbons than the Eagle Ford sample (which is quite likely, as this Utica comes from a section of the gas window), and that some of the clay-bound water could have vaporized at lower temperatures, as has been reported in previous TGA papers (Santos et al., 1997). The sample shows a ramp up in derivative peak from 450°C to 540°C, probably the maturation of organics combined with the decomposition of siderite. It is followed by a

much more gradual ramp from 550°C to 700°C, which can probably be explained by degradation of kaolinite and illite, kerogen maturation, and then the beginning stages of dolomite composition. The carbonate peak is at 765°C, indicative of the presence of both dolomite and calcite, and just like Bakken, a small inflection point at 810°C is indicative of the final stages of calcite decomposition.

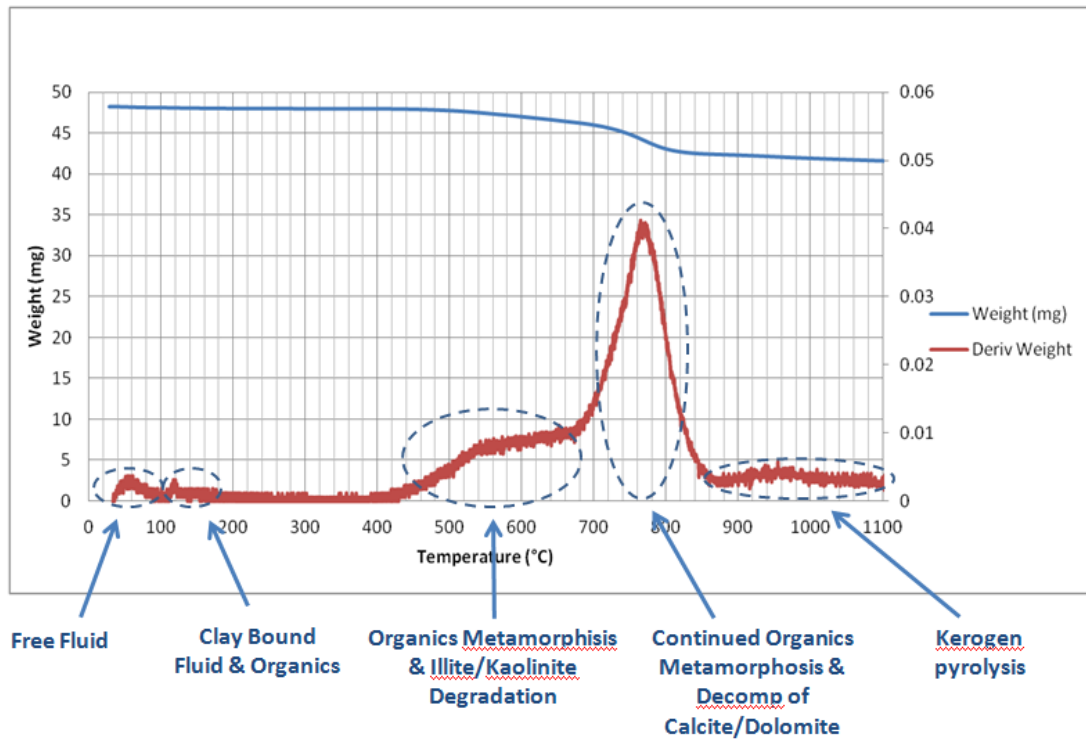


Figure 2.16: TGA and derivative peaks of the Utica sample with explanations of peaks

Of particular note for the three TGA results are the scales at which the derivative peaks lie. The scales were sized differently in order to more accurately show the peaks for explanatory purposes. The Bakken and Eagle Ford are scaled relatively close, with maximum values of 0.12 and 0.16 mg/°C, respectively. However, the Utica has been significantly “zoomed-in” with a maximum value of 0.06 mg/°C. This explains quite well

the reduced amount of carbonate shown by the mineralogy for the Utica compared to the other two. This will be compared quantitatively in Section 2.3.4.

Also of note for both of the Eagle Ford and Utica compared to the Bakken is the raised derivative values after the carbonate peak. The source rocks show elevated derivative values throughout the very high temperatures, whereas the Bakken shows only a peak at 940°C with the values returning to 0 on both sides. This may be due to further kerogen pyrolysis of extremely complex, solid hydrocarbons exhibited only in kerogen. As mentioned previously, however, this section of the data is quite difficult to analyze.

Problems with TGA Analysis

TGA has great potential for use in analyzing source rocks, but does have severe associated problems. Most importantly is the lack of direct identification of mineralogy and hydrocarbons when peaks cannot be isolated, which is largely the case for much of the higher temperatures. Therefore, TGA in this capacity may be best served as a method for confirming or modifying the results of other mineralogy studies.

2.5 Quantitative Analysis using TGA

There is much valuable information that can be gained by analyzing TGA data with various methods, these are mainly:

1. An estimate of the total free liquid vs. clay-bound liquid porosity
2. An estimate of overall carbonate content
3. An estimate of free fluid concentration and a percentage of TOC that is producible hydrocarbon from subtracting isolated TGA signals of known components

It should be noted that all of these methods require assumptions. However, the third method is the most empirical and probably holds the most merit when using TGA alone. When molecule identification is possible, the techniques become more accurate and thus more powerful. This is discussed further, utilizing Py-GC-MS, in Chapter 3.

2.5.1 Estimation of Carbonate Content

The overall carbonate content of the sample can be estimated using the total peak area (which is the same as the total weight loss of the sample over the temperature range of the peak), and the temperature at which the maximum of the peak occurs. The assumption must be made that all other thermal events taking place in this temperature range are negligible. An estimate of calcite-dolomite breakdown is done via the temperature at the peak maximum. This is based on dolomite decomposing first at 625°C and then again at 800°C, giving an average peak at 725°C for carbonate that is purely dolomite. Thus, a linear interpolation between 725°C and 800°C can be utilized to roughly estimate the % of carbonate molecules that are calcite and dolomite, and is given by Equations 2.7 and 2.8, respectively.

$$X_{CaCO_3} = \frac{T_{peak} - 725^{\circ}C}{800^{\circ}C - 725^{\circ}C} \quad (2.7)$$

$$X_{MgCa(CO_3)_2} = 1 - \frac{T_{peak} - 725^{\circ}C}{800^{\circ}C - 725^{\circ}C} \quad (2.8)$$

Where X_i is the molar fraction of calcite or dolomite of the total carbonate content of the sample, T_{peak} is the temperature at which the carbonate peak of the TGA is at its

max. The breakdown can be converted into weight fraction of each carbonate, given by Equations 2.9 and 2.10.

$$m_{CaCO_3} = \frac{X_{CaCO_3} * 100.086 \frac{g}{mol}}{X_{CaCO_3} * 100.086 \frac{g}{mol} + X_{MgCa(CO_3)_2} * 184.399 \frac{g}{mol}} \quad (2.9)$$

$$m_{MgCa(CO_3)_2} = \frac{mol \% dolomite * 184.399 \frac{g}{mol}}{X_{CaCO_3} * 100.086 \frac{g}{mol} + X_{MgCa(CO_3)_2} * 184.399 \frac{g}{mol}} \quad (2.10)$$

Where m_i is the mass fraction of calcite or dolomite relative to the total carbonate mass of the sample. Table 2.3 shows these calculations carried out on the Bakken, Eagle Ford, and Utica TGA's shown in Section 2.3. While not a perfect match, they do give a good indication as to the carbonate breakdown. Additionally, while care was taken to homogenize samples to have the same mineral content sent out for XRD as performed on TGA, this is not always the case.

Formation	Peak Temperature (°C)	Calculated Dolomite Fraction of Carbonate	Dolomite Fraction of Carbonate from XRD
Bakken	727	98.5 %	70.1 %
Eagle Ford	836	0.0 %	0.0 %
Utica	765	47.9 %	32.7 %

Table 2.3: Peak temperature and calculated dolomite concentration compared to XRD results

Next, the weight percent of the dolomite and calcite can be estimated for the entire sample through the use of the weight loss over the range of the carbonate peak. This can be determined with Equations 2.11 and 2.12, respectively.

$$M_{CaCO_3} = \frac{W_{carbonate} * \left(m_{CaCO_3} * \frac{100.086}{60} \right)}{W_{initial}} \quad (2.11)$$

$$M_{MgCa(CO_3)_2} = \frac{W_{carbonate} * \left(m_{MgCa(CO_3)_2} * \frac{184.399}{120} \right)}{W_{initial}} \quad (2.12)$$

Where M_i is the mass fraction of calcite or dolomite relative to the total sample. These calculations conducted on the three samples are shown in Table 2.4 and 2.5 below.

Formation	Carbonate Peak Low Temp (°C)	Carbonate Peak High Temp (°C)	Initial Sample weight (mg)	Carbonate Peak Weight Loss (mg)
Bakken	580	810	40.88	5.58
Eagle Ford	715	855	47.30	9.94
Utica	650	850	48.21	4.21

Table 2.4: Carbonate start and end points for use in total carbonate content calculation

Formation	Calculated Dolomite Concentration (wt %)	Calculated Calcite Concentration (wt %)	XRD Dolomite Concentration (wt %)	XRD Calcite Concentration (wt %)	Overall % Carbonate Accounted For
Bakken	20.65	0.34	20.01	8.60	73.36
Eagle Ford	0.00	35.01	0.00	50.00	70.01
Utica	6.42	7.58	5.20	10.70	88.05

Table 2.5: Calculated dolomite and calcite concentrations compared to XRD results

As shown in the table, the overall dolomite concentrations for the Bakken, Eagle Ford, and Utica seem to be relatively reasonable. However, the calcite concentration does not seem to accurately reflect the XRD results for both the Bakken and Eagle Ford. This stems from two reasons. Firstly, the calculated amount of dolomite compared to calcite may be incorrect from the initial calculations. More importantly, however, the overall amount of carbonate measured via the TGA and calculations is significantly less than what is shown in XRD; this is the main factor causing error for the Eagle Ford. All three show this to varying degrees. The expected result was for the TGA estimates to be higher than XRD, as other thermal events are taking place over this temperature range which are not being subtracted out.

Overall, this method seems to work well primarily for lower carbonate concentration rocks, as displayed by the Utica where the total amount of carbonate accounted for was 88%. However, further testing is required.

2.5.2 Estimation of Free Fluid Content

The second method allows for the estimation of the producible fluid in the sample. This is representative of the free fluid that is not bound by clay or inorganic pores. The

calculation technique requires two assumptions which simplify the processes going on in the thermal events. First, it must be assumed that all vaporized fluid in the low temperature range (usually 25-175°C) is free and producible. This is a reasonable assumption with shales that have a low clay content, and all of the samples shown in this thesis exhibit these characteristics. Additionally, only fluid from swelling clays would contribute in this temperature range, and thus clay contribution is further reduced.

Secondly, a density for the produced fluid must be assumed to convert the mass recorded by the TGA to volume. Through the use of Py-GC-MS to identify the chemical constituents of the vaporized fluid, a density of the fluid has been generated for each of the samples, but all are near 0.8 g/mL. This is because nearly all of these samples exhibit very small amounts of water, and mainly oil. This is discussed in greater detail in Chapter 3.

Lastly, an overall density for the sample must be known as well. This is measured directly via very accurate Archimedes weight and submersion methods. The equation for this method is given by:

$$\varphi_{Free} = \frac{(M_{low} - M_{high}) / \rho_{fluid}}{M_{sample} / \rho_{sample}} \quad (2.13)$$

Where φ_{free} is the volume fraction of free fluid in the sample, M_{low} is the TGA mass at the low temperature defined as the free fluid range, M_{high} is the TGA mass at the

high temperature of the free fluid range, M_{sample} is the starting mass of the sample in the TGA, ρ_{fluid} is the density of the fluid, and ρ_{sample} is the density of the sample.

The results of using this method for the Bakken, Eagle Ford, and Utica samples are shown in Table 2.6 below, and are compared to the NMR porosity measured via transverse relaxation time (T_2). While not a perfect measurement of free fluid porosity for shales, it does represent a number that should be relatively close, as much of the very tightly bound fluid is expected to have T_2 relaxation times too short to measure. This is discussed further in Chapter 4.

Formation	Free Fluid Volume Fraction (%)	NMR Porosity
Bakken	9.8	9.45
Eagle Ford	3.2	5.21
Utica	2.3	4.34

Table 2.6: Free fluid volume fraction compared to NMR porosity of Bakken, Eagle Ford, and Utica samples

As shown, the calculation trends quite well with the porosity measured via NMR. The NMR porosity is generally higher than the free fluid volume fraction. This can be readily explained by the fact that the TGA samples were crushed, whereas the NMR samples were 1” or 1.5” plugs, and some of the free fluid has escaped in the crushing process. The exception to this is the Bakken, which shows a lower NMR porosity than the calculation.

This method is primarily useful as a confirmation tool to use in conjunction with other measurements. Alone, this method does not give a good indication of the amount of oil present in the rock that may be producible, as it is possible for the entirety of the fluid in this temperature range to be water.

2.5.3 Estimation of Overall Free Fluid Content by Subtracting Clays

As mentioned previously, one of the errors contributing to estimating fluid volume fraction is the amount of swelling clay present. This error can be minimized by subtracting out these effects from the shale TGA signal. The method used to perform this requires the generation of clay standards, which are then used in proportion with XRD data for each corresponding clay. The resulting signal should then reflect the thermal events for the shale without clay. Since the only thermal events observed in the low temperature range are from free and clay-bound fluid, the subtracted signal is effectively that of the free fluid alone.

This method has the same drawback as the previous method, in that it cannot differentiate between water and oil. However, as will be discussed later, the overall free fluid content is still a valuable number as it can later be dissected when exact fluid composition can be identified.

The creation of clay standards involved the three major clay types: smectite, kaolinite, and illite. They were run individually to establish a TGA signal for each one. Additionally, varying combinations of the clays were run to ensure the TGA signal was linear based on weight percent of the clay. It has been mentioned in previous papers (Santos et al., 1997) that these different combinations are not linear. However, this was not observed in these experiments. The most likely explanation for this difference is that the combinations created for this research were simply crushed together and mixed at the macro scale, whereas those measured in the previous papers are combined at a much smaller scale. At this smaller scale, the direct interactions between the clays are more capable of causing a change in temperature where a given thermal event will take place. The clays mixed at the macro scale will not exhibit this behavior, as they cannot be

mechanically made to be close enough to have these interactions in great significance, and thus linear results are observed. For the purpose of this thesis, we assume that the clays in shales exhibit linear combinations.

Figures 2.17, 2.18, and 2.19 show the TGA signals for the three clays. The one of the most significance is smectite, as it exhibits the greatest impact in the low temperature range. The combined clay signals are shown in Appendix 4. It is important to note that these clay calibration samples were prepared in the same manner as the shale samples discussed in Section 2.4. Most importantly, they were allowed to equilibrate with the correct water activity under controlled humidity.

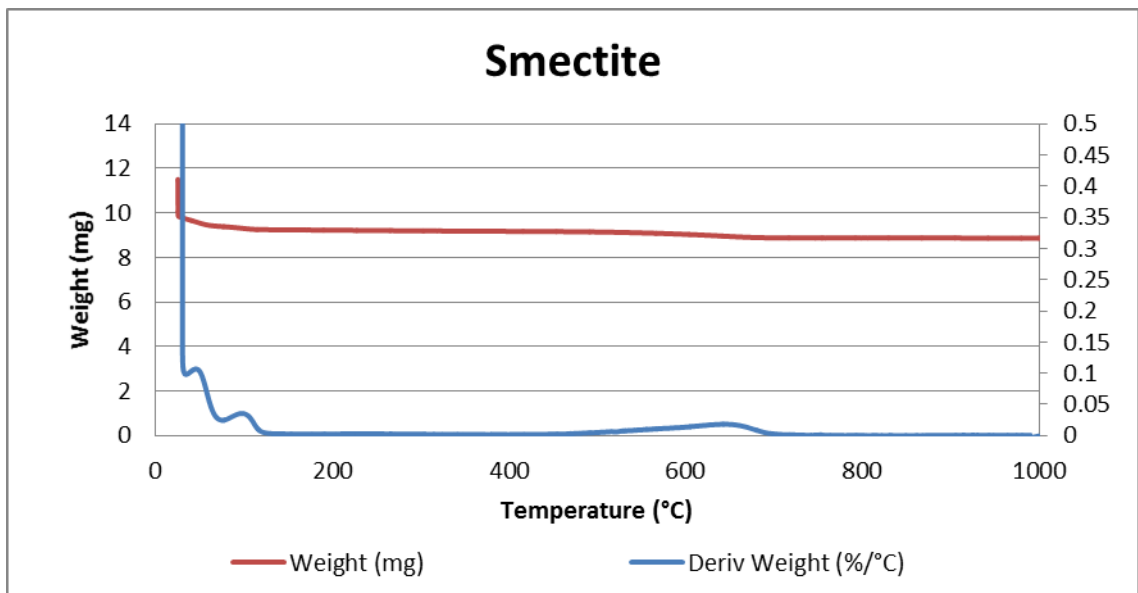


Figure 2.17: TGA signal and derivative weight of smectite

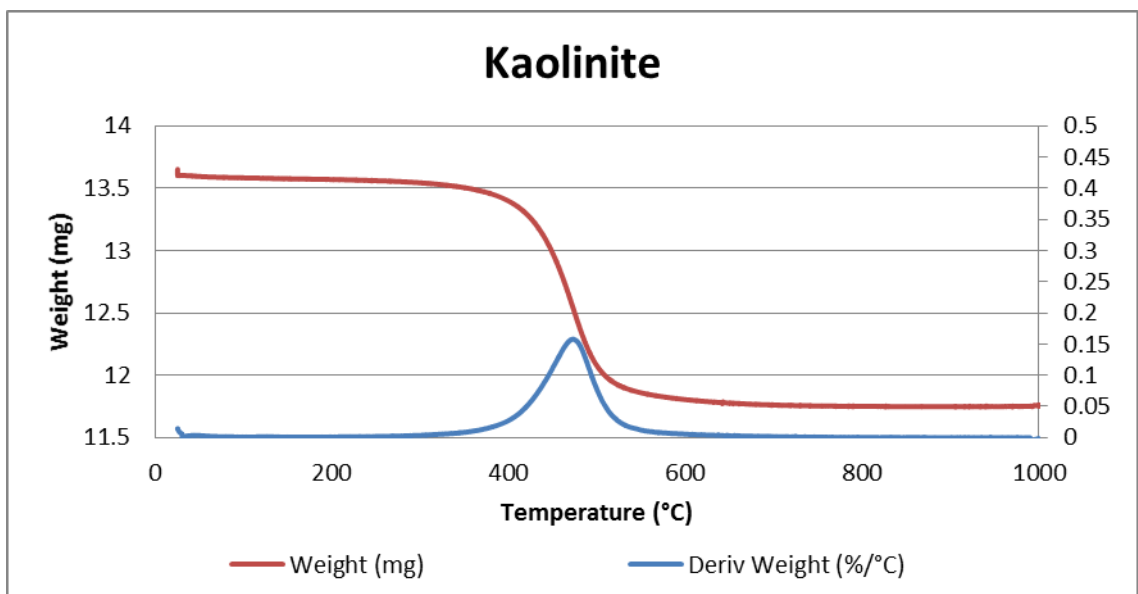


Figure 2.18: TGA signal and derivative weight of kaolinite

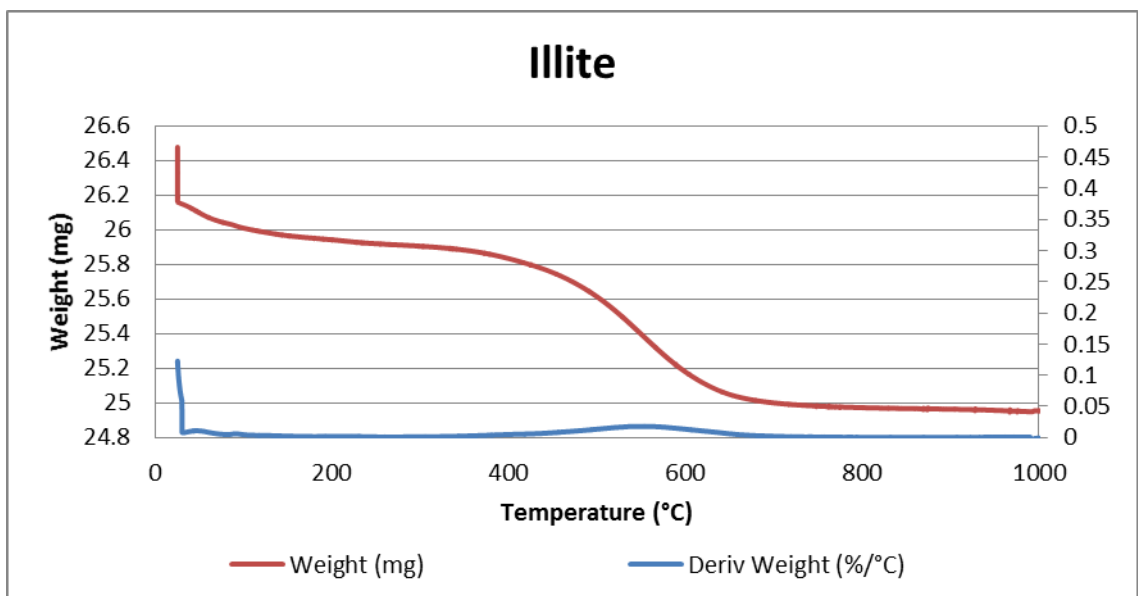


Figure 2.19: TGA signal and derivative weight of illite

Results

Figures 2.20 and 2.21 below show the Eagle Ford sample derivative weight raw, then with the subtraction. As expected, the change in the signal is rather small, and the most noticeable change at this scale is in the range of 400-500°C where some of the subtracted signal is negative. Also, the carbonate peak is unaffected.

Zooming in on the low temperature peak reveals some small changes as well. Interestingly, the peak observed at the lowest temperature can be largely accounted for via the clay. It was previously expected that clay bound water would not vaporize at low temperatures, and especially at the lowest point. Overall, the entire low range peak is reduced very little, and is due to the fact that the XRD analysis revealed only 18.4% clay by weight, with much of this not being smectite (only 5.7%).

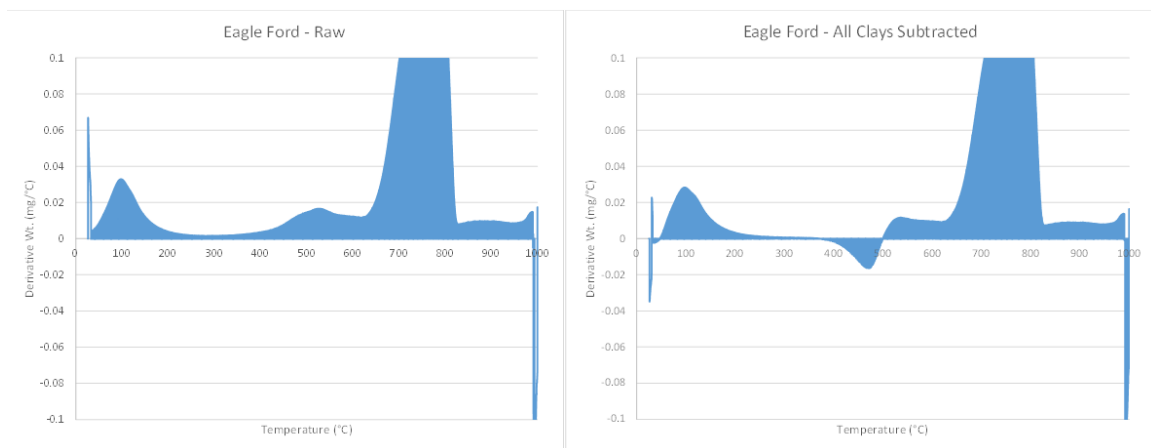


Figure 2.20: Raw and subtracted derivative weight of Eagle Ford sample

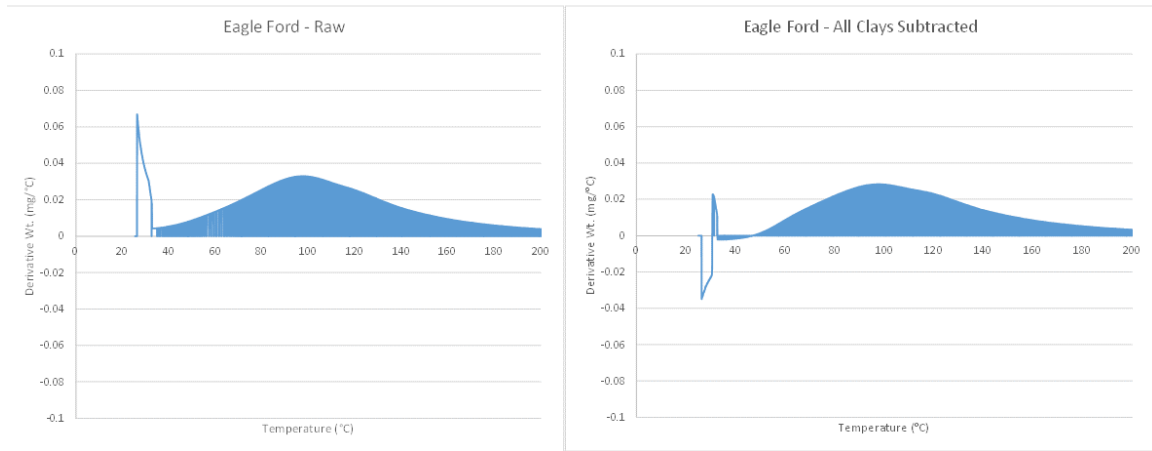


Figure 2.21: Raw and subtracted derivative weight of Eagle Ford sample zoomed in to the low temperature range

This reduction represents a 24% reduction in the estimated free fluid content by weight, and brings the free fluid volume fraction down to 2.5%. Therefore, this is not a sizeable reduction compared to the original estimation of 3.2%, largely because the amount of clay is quite small. This process is repeated for the Bakken and Utica, and the results are shown in Table 2.7 below.

Formation	Free Fluid Volume Fraction - Uncorrected	Free Fluid Volume Fraction – Corrected for Clays
Bakken	9.8	9.1
Eagle Ford	3.2	2.5
Utica	2.3	1.7

Table 2.7: Free fluid volume fractions of the Bakken, Eagle Ford, and Utica samples uncorrected and corrected for clay-bound water

2.6 TGA Conclusions

Overall, TGA can be a valuable method to gain additional data useful for characterizing shales. The method is very simple and easy to perform. With a basic understanding of thermal events and geochemistry, it is possible to estimate the carbonate concentration and free fluid volumes both corrected and uncorrected for clay water content. The method may be best utilized as a confirmation tool for other techniques, especially for early stages of use. Opportunities may involve quick verification of carbonate concentration when using small portable XRD machines. Also the field analysis of cuttings may provide data to help delineate play boundaries or may be correlated to core data for formation evaluation.

In general, however, we believe that TGA can play its most important role in conjunction with Py-GC-MS, where it provides accurate mass data, which can be matched with accurate chemical identification data. This gives a very detailed picture of exactly what type of gas is being volatilized, and therefore, what type of fluid is contained in the rock.

3 Pyrolysis-Gas Chromatography-Mass Spectroscopy (Py-GC-MS)

3.1 Py-GC-MS Basics

Pyrolysis-Gas Chromatography-Mass Spectroscopy is simply the combination of the three methods in linear order performed on a single sample. Specifically, a small crushed sample on the order of 50 mg is placed into a small pyrolysis tube above a heat conducting fiber. Inert gas, usually nitrogen, is purged through the tube to eliminate any oxygen. The tube and the sample are then “flash” heated to the desired temperature in 1 to 2 minutes, and held for 1 minute. Fluids with boiling points at this temperature or below can then vaporize, exit the sample into the purge gas stream, and then enter the gas chromatograph (GC).

The GC typically utilizes a basic boiling point separation capillary tube where the different molecules vaporized have different retention times. The primary factor determining this retention time is the boiling point of the fluid compared to the temperature of the GC, and thus the name. In the case of our experiments, water and CO₂ have a retention time of 1.3 minutes and 2.0 minutes, respectively. CO₂ moves slower through the capillary tube because the GC is held slightly higher than 100°C, and the slight polarity of water allows it to travel slightly faster. Hydrocarbon retention times vary widely from 7 to 14 minutes. This separation is important, as it allows the final step, the Mass Spectrometer (MS), to identify each molecule individually.

It is beyond the scope of this thesis to describe in detail the workings of Mass Spectrometry. In short, the method is based on ionizing the molecules by removing an electron, and then accelerating the molecule to a set kinetic energy. It is then deflected

from its trajectory by a magnetic field, and the magnitude of the deflection allows for the mass of the ion to be identified. Molecules are typically broken into two or more different ions, and thus leave a “signature” of different compounds representing the breakdown of the original molecule. This signature can then be compared to databases of known standards for identification. Additionally, the “abundance” of molecules going through the mass spectrometer at different retention times can be recorded. This allows for a calculation of the weight fraction of each molecule for a particular Py-GC-MS run. It should be noted that the term abundance used in this instance is different than the term “relative abundance” which is used to define the size of peaks of different ions when actually identifying a molecule in the MS. Abundance in this thesis is used as the total electrical signal for each molecule (defined by retention time), and again is used to calculate the weight fraction.

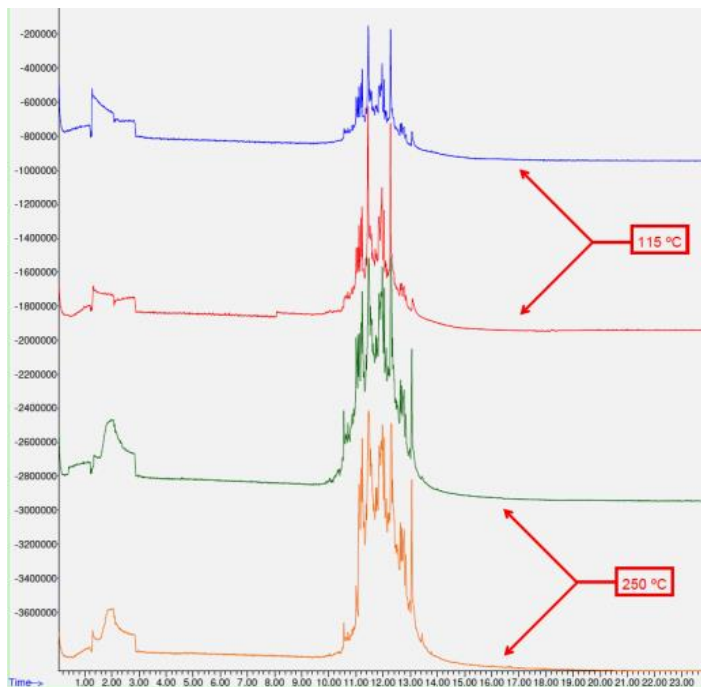


Figure 3.1: Example Abundance vs. Retention time readout from Py-GC-MS.

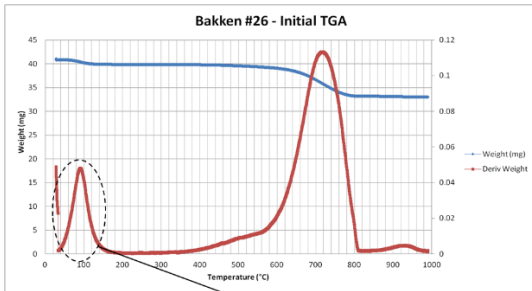
As mentioned in Chapter 2, one of the biggest benefits of TGA is the ability to tie the weight fraction information from Py-GC-MS to the overall sample weight by using identical temperatures and samples in the two techniques such that the vaporized fluid should be identical as well. This then allows for the calculation of the weight fraction of a molecule relative to the entire sample, which can be used to calculate saturation.

3.1.1 Procedure for Linking Py-GC-MS with TGA to Get Vaporized Fluid Concentration Relative to the Overall Sample Size

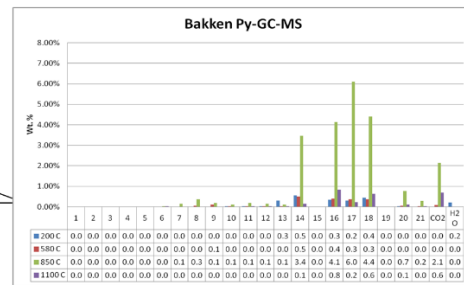
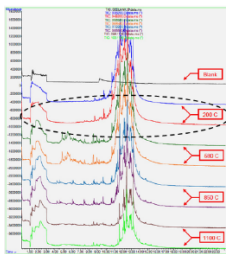
Simply put, the method for determining the vaporized fluid concentration relative to the sample is to multiply the mass data from the TGA with the concentration data from Py-GC-MS. Procedurally, this is performed by first running a TGA, and determining a good “end point” for a given set of thermal events. This temperature is then used as the flash heating point for a Py-GC-MS experiment. The fluid composition that results is then assigned to the given mass loss of the TGA over this temperature span. This can be repeated at higher temperatures to allow the composition to be analyzed for each set of thermal events. The result of this combination is the concentration of each molecule relative to the original sample weight for a given temperature range. An illustration of this combination is shown by Figure 3.2 using the Bakken as an example.

More specifically, the output of the Py-GC-MS gives the exact molecules present. An example of this data is shown in Figure 3.3 for the same data shown in Figure 3.2. This bulk data is then placed into different bins based on the number of carbon atoms (with the exception of H₂O and CO₂, which are kept separate) to allow for analysis. The final output is a chart showing the wt. % relative to the sample of different chain lengths at each temperature. The interpretations of these diagrams will be explained in greater

detail in later sections. An example of this output is shown in the lower right corner of Figure 3.2.



Mass information for a given temperature step
+
chemical identification information =



Concentration of the vaporized fluid for each chemical step

Figure 3.2: Illustration of Combination of TGA and Py-GC-MS for molecular concentrations for a given temperature step.

200C			
Retention Time (min)	NIST Best Match Compounds	Match Factor	Abundance (10 ⁷)
1.334	Water	720	21.9
7.504	Cyclotetrasiloxane, octamethyl-	763	0.1
7.768	Nonane, 2,6-dimethyl-	791	0.1
8.269	Decane, 2-methyl-	777	0.2
8.360	Decane, 3-methyl-	628	0.1
8.691	Undecane	838	0.8
9.074	Benzene, 1,2,4,5-tetramethyl-	704	0.5
9.228	Cyclopentasiloxane, decamethyl-	841	0.1
9.288	1-Decanol, 2-methyl-	629	0.5
9.373	1-Octanol, 2-butyl-	695	0.4
9.658	Naphthalene, decahydro-2,3-dimethyl-	641	0.5
9.752	Dodecane	919	1.1
9.885	Undecane, 2,5-dimethyl-	739	1.1
10.198	1,1,6,6-Tetramethylspiro[4.4]nonane	667	1.4
10.454	9-Undecenol, 2,10-dimethyl-	663	3.0
10.534	2-Undecanone, 6,10-dimethyl-	628	1.0
10.726	Tridecane	769	5.3
10.811	1,11-Tridecadiene	715	1.6
10.888	1,11-Tridecadiene	682	3.8
11.207	1-Dodecanol, 2-methyl-	657	14.9
11.327	Tridecane, 2-methyl-	743	7.9
11.446	Tetradecane	698	13.9
11.707	Tetradecane	757	35.2
11.949	2-Dodecen-1-yl(-)succinic anhydride	724	2.4
11.987	2,5-Furandione, 3-dodecyl-	724	4.2
12.118	Tridecane, 5-propyl-	687	11.8
12.213	Undecane, 5-ethyl-5-propyl-	656	10.4
12.277	Pentadecane, 4-methyl-	625	6.1
12.356	Hexadecane, 2-methyl-	675	11.6
12.555	Heptadecane	646	18.6
12.629	Acetic acid, chloro-, hexadecyl ester	694	3.5
12.714	Heptadecane, 3-methyl-	614	9.1
12.844	Heptadecane, 8-methyl-	701	6.2
12.908	Heptadecane, 2-methyl-	669	6.0
12.972	Heptadecane, 2-methyl-	697	4.3
13.034	Heptadecane, 3-methyl-	645	4.5
13.160	Oxirane, hexadecyl-	684	4.3
13.249	Octadecane	750	7.1
13.572	Ethanol, 2-(octadecyloxy)-	664	0.1

Figure 3.3: Py-GC-MS output for the Bakken at 200°C showing the GC retention time, molecular match, the match factor, and its abundance.

3.2 Py-GC-MS Results for Multiple Temperature Steps

Py-GC-MS was run on the Bakken, Eagle Ford, and Utica samples following the procedure detailed in Section 3.2.1 at multiple temperature steps in order to develop a greater understanding of the molecular distribution at varying thermal events. The most interesting and useful is the low temperature step, which can give information about the producible fluid in the sample. More details are discussed in Chapter 5.

Temperature steps were designated for each of the samples via TGA and are shown in Table 3.1. The TGA signals used to determine the steps can be found in Appendix 1.

Sample	Step 1	Step 2	Step 3	Step 4
Bakken	200° C	580° C	850° C	1100° C
Eagle Ford	320° C	600° C	860° C	1100° C
Utica	275° C	625° C	850° C	1100° C

Table 3.1: Temperature step end points for the Bakken, Eagle Ford, and Utica

It should be noted that these samples are different than those used described in Chapter 5, but are the same samples discussed in the NMR subtraction section in Chapter 4. The results of these tests are shown in Figure 3.4, 3.5, and 3.6.

3.2.1 Results and Discussion

There are several key results to point out. First, the amount of CO₂ that is shown in the 850°C temperature step for all three samples is significantly lower than what would be expected based on the mineralogy. At this temperature, calcite and dolomite decomposition should be the largest thermal event and should result in a large release in CO₂ indicated by the Py-GC-MS. The trend of CO₂ as temperature increases is expected,

in that there is very little or no CO₂ at lower temperatures, but it does increase with higher temperatures. However, at the time of writing, no solid explanation for the lack of CO₂ in the 850° C peaks can be explained. The second point of note is the increase in composition of the shorter chain molecules (<C₁₁) in both the Eagle Ford and Utica samples but is missing from the Bakken. This can be readily explained by the fact that both the Eagle Ford and Utica are source rocks with kerogen and bitumen present. This emergence of shorter chain molecules can thus be interpreted as the continued maturation of long chain hydrocarbons. This is different from the Bakken, as this represents the breaking off of small chains from extremely long chains, whereas in the Bakken only medium chain length (<C₂₁) hydrocarbons exist and instead vaporize prior to maturing. Lastly, the amount of water shown in the samples seems to be concurrent with expectations. There is a little water at the lower temperatures, and then very little or none at the higher temperatures.

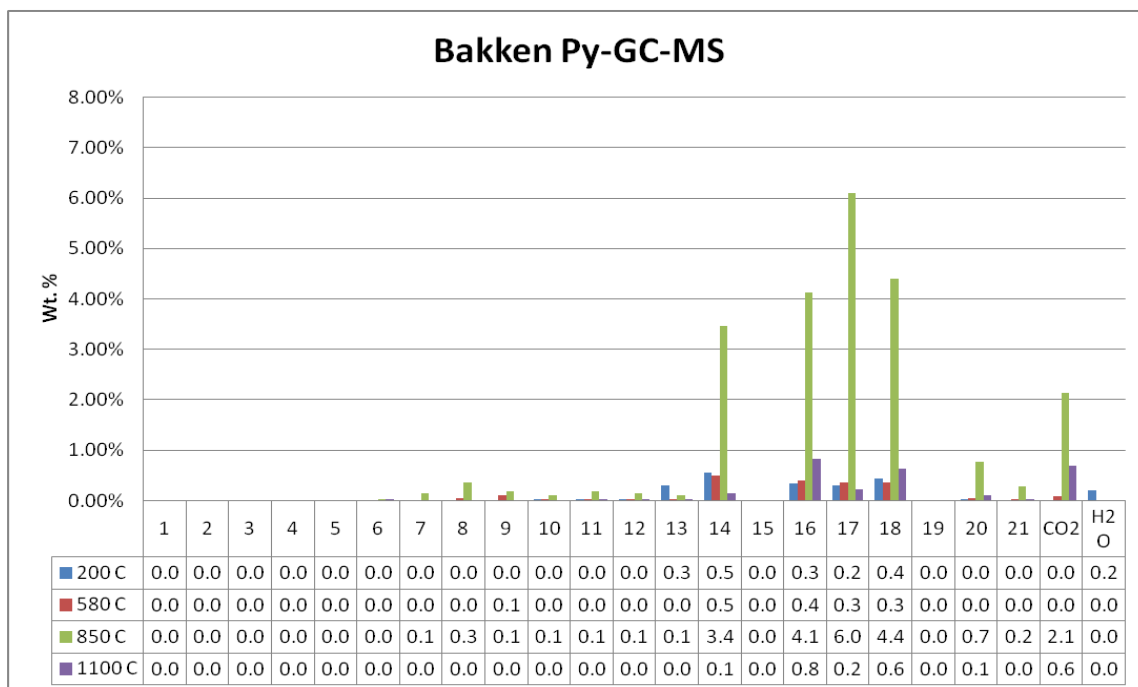


Figure 3.4: Wt. % of vaporized fluid at various temperature steps categorized by # of carbon atoms of the Bakken sample

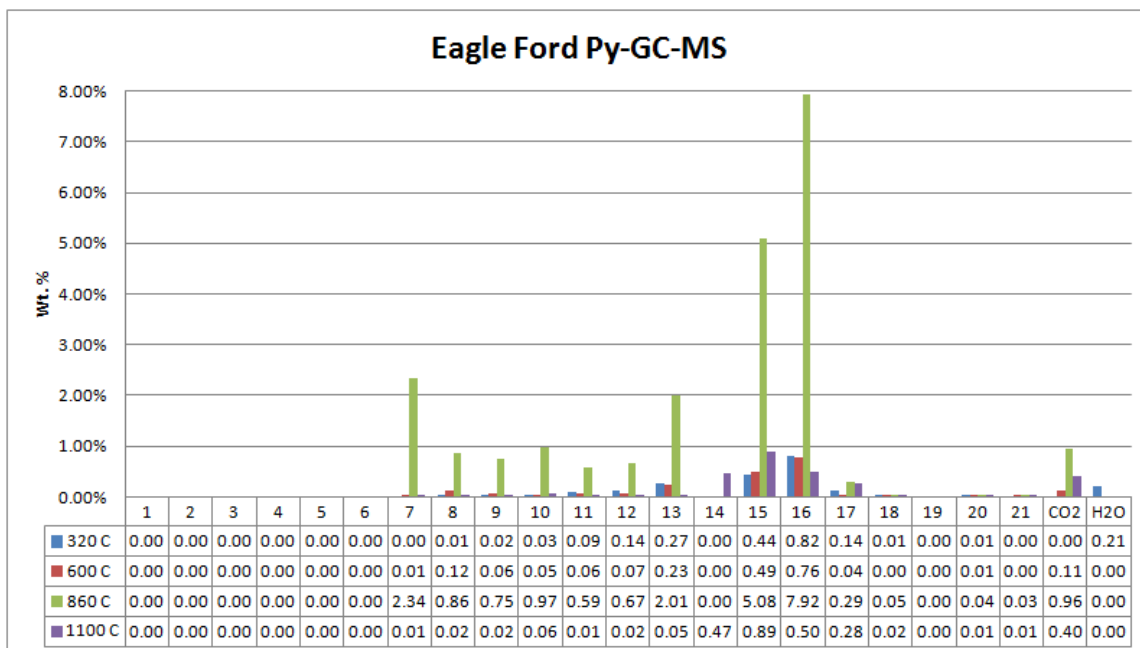


Figure 3.5: Wt. % of vaporized fluid at various temperature steps categorized by # of carbon atoms of the Eagle Ford sample

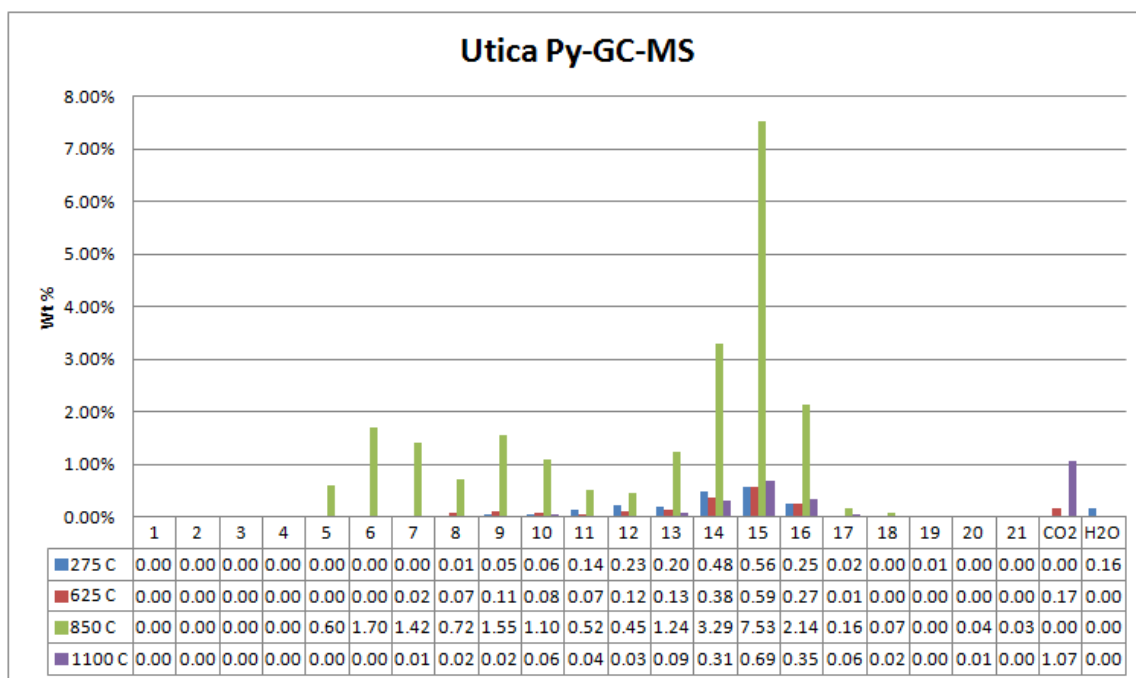


Figure 3.6: Wt. % of vaporized fluid at various temperature steps categorized by # of carbon atoms of the Utica sample

3.3 Conclusions

Py-GC-MS is a promising technique that has the capability of more accurately identifying and characterizing fluid both free and bound. It is most powerful when combined with TGA in order to obtain the mass of each compound relative to the weight of the sample. Identifying temperatures for various thermal events is an important part of the analysis when using Py-GC-MS in order to have a clear understanding of the composition of the fluid is being analyzed at a given temperature. The results of the initial study are consistent with expectations in terms of hydrocarbon chain lengths at various temperatures and trends of water and CO₂, although the actual quantity of CO₂ does not. In general, Py-GC-MS provides useful data not currently available by any other means, and therefore, is a valuable tool for shale characterization.

We see it has having large potential use in detailed laboratory studies, especially for the determination of saturations which cannot be determined by conventional means. However, due to cost and the required maintenance of equipment, it is probably not applicable to studies involving a large number of samples or field applications.

4 Nuclear Magnetic Resonance (NMR)

4.1 Introduction

NMR has been used for several decades as a tool in the laboratory and field, and is utilized for analyzing porosity of formations and diffusion of fluids in a non-destructive manner. While the techniques for NMR study have been well researched for use in conventional (large pores and little clay or source organic material) formations, NMR work on shale formations is quite limited with the exception of a few key pieces of work that will be discussed below.

4.1.1 Governing Physics

NMR utilizes the naturally occurring phenomena of the relaxation of spin states of nuclei when held in a magnetic field. While NMR is possible on any atom with an odd atomic number, Hydrogen is almost always the atom utilized as it has a large magnetic moment due to its single proton and no neutrons.

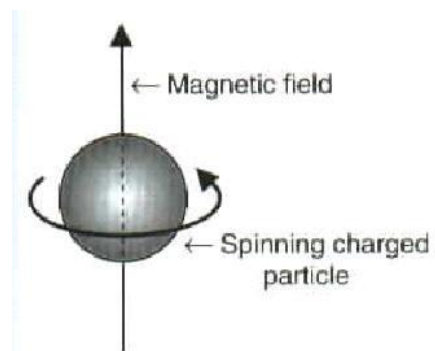


Figure 4.1: Spin states of protons (www.process-nmr.com)

Also, since it has only one proton, understanding its magnetic spin is relatively easy. Since the proton has a set angular momentum and a positive charge, it generates a positive and negative pole, much like a bar magnet. The direction of north vs. south is based on the direction of rotation of the proton via the Right-Hand Rule. All NMR measurements are based on the manipulation of these magnetic spin states.

Outside of any static magnetic field, the direction of the hydrogen magnetic poles of different atoms are randomly oriented. However, after a static magnetic field is applied, commonly referred to as B_0 , the hydrogen atom's spin axis will line up with the static external magnetic field. It is from this starting point that further measurements of magnetism can be taken. The spin states can align with the external field in two ways: most atoms will align their magnetic fields in the same direction as the external static magnetic field; this is called the “low energy state.” Some atoms, however, will point 180° (or exactly opposite) to the external magnetic field in a “high energy state.” The resultant (or net) magnetism from these two orientations is an equilibrium that is measured by the device (Coates, 1999). This situation is analogous to holding two bar magnets with two alike poles directly facing each other.

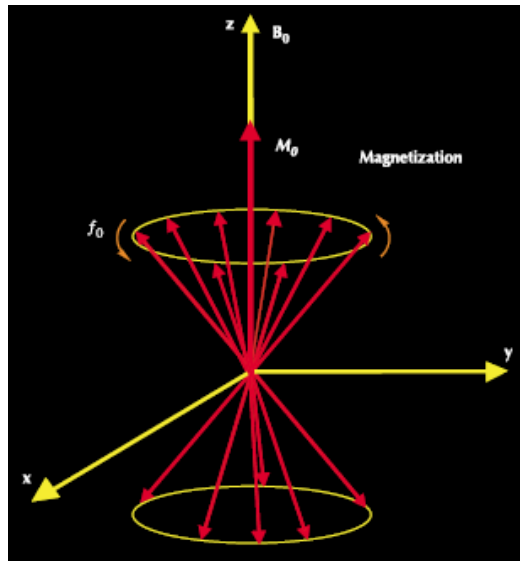


Figure 4.2: Polarization of nuclear spins (After Coates, 1999)

This process of going from random orientation of the spin axis to the equilibrium shown in Figure 4.2 is called polarization. The amount of time for the net magnetization, M_0 , to go from 0 to 63% of its final value is considered the longitudinal relaxation time (Coates, 1997).

If an oscillating magnetic field with a frequency equal to the Larmor frequency is applied perpendicular to the static magnetic field (shown in the x direction in Figure 4.2), the spin states will begin to precess about the axis in an overlapping manner. The frequency of this precession is defined as the Larmor frequency, and is based on the strength of the external magnetic field and the gyromagnetic ratio of the nucleus.

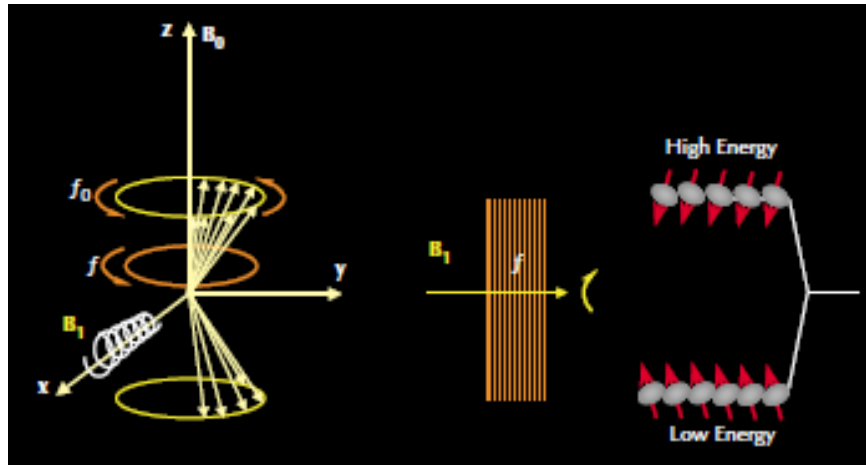


Figure 4.3: Oscillating magnetic force and resultant magnetic force in x-axis (Coates et al., 1997)

This means that they will be in phase with one another, and will have a resultant magnetism in the direction of the new magnetic field. Additionally, some of the nuclei will be able to absorb the energy from the new magnetic field and swap energy states from low to high. The result is a net magnetism in the direction of B_0 (z-axis) of 0, and a net magnetism in the direction of B_1 as positive. This precession with the oscillating magnetic field is Nuclear Magnetic Resonance (Coates, 1999). When the oscillating magnetic field is turned off, the net magnetism on the x-axis will begin to degrade back to a 0 net magnetism. This slow degradation is called dephasing, and is referred to as a “Free Induction Decay” or FID. The amount of time for the net magnetism to go from its highest point when the oscillating magnetic field is on to 0 is called T_2^* , and is rarely used as it is largely due to magnetic inhomogeneities (Coates, 1999). This process is best illustrated in Figure 4.4.

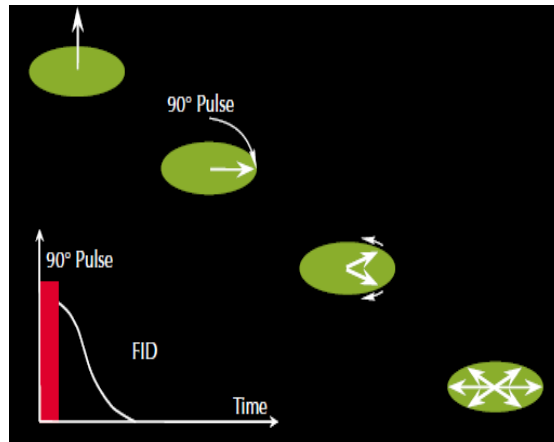


Figure 4.4: FID decay of T_2 measurement (Coates et al., 1999)

More usefully, the nuclear spins can be influenced to move back again in the direction of the net magnetization along the x-axis with another 180° pulse (the opposite direction of the original static magnetic field, B_0); however, the resultant magnetism will not be as high as from the original 90° pulse. If done repeatedly, it creates a continually forming and decaying net magnetic force in the x-axis, until the signal eventually degrades completely. These continuing peaks are called echoes, and the time between peaks of the net magnetic force is referred to as the transverse relaxation time (T_2). T_2 is the most common NMR measurement in petrophysics and is the basis of study for most conventional reservoirs when utilizing NMR (not necessarily for unconventional, as will be illustrated below) (Cao Minh, 2006).

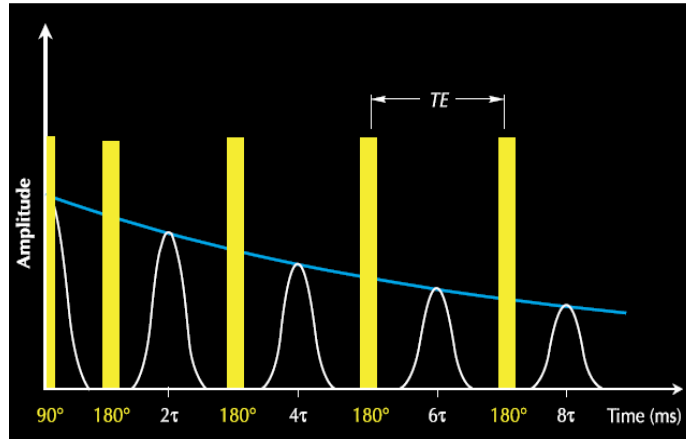


Figure 4.5: T_2 echo train decay (After Coates et al, 1999)

Factors Affecting T_1 & T_2

The reason NMR is so effective at measuring rock properties such as porosity is due to the relaxation mechanisms that affect the longitudinal (T_1) and transverse (T_2) relaxation times. There are two major theories underpinning descriptions of the mechanisms associated with these relaxation times. The first is associated with interactions of the fluid and unpaired electrons in the outer orbital shells of paramagnetic ions on the surface of the rock matrix, which ultimately cause a faster loss in net magnetism spin. The second is caused by dipolar coupling, or the "transmission" of magnetic energy from two molecules with like dipole moments. This is often the case with organic hydrogen or hydroxyl groups (Foley, 1996).

The mechanism for T_1 involves the transfer of energy from the precessing nuclei to their environment whenever they switch energy states and go to their natural equilibrium. The two main factors affecting this time is the bulk T_1 , which is the longitudinal relaxation time if the fluid was in a large container where there were minimal effects from the container, and surface T_1 , the longitudinal relaxation time if there were only a

single layer of atoms of fluid on the surface, thus maximizing the effects of paramagnetism. These two effects work in parallel to arrive at a T_1 time somewhere in the middle, and can be quantified by Equation 4.1:

$$\frac{1}{T_1} = \frac{1}{T_{1,bulk}} + \frac{1}{T_{1,surface}} \quad (4.1)$$

The mechanism for T_2 is slightly more complicated. It also involves the parallel times of bulk relaxation as well as surface relaxation. Also, while it does involve some transfer of energy between the precessing nuclei and the environment from the natural re-orientation to equilibrium along the z-axis, this component is much smaller than the relaxation from the net magnetism along the x-axis back to a zero value. Therefore, T_2 relaxation times are generally faster than T_1 times. Additionally, another factor involved in T_2 is the diffusion of particles out of the zone affected by the 90° oscillating magnetic field along the x-axis. Since T_2 times are collected via a train of echoes, the atoms have time to diffuse from the measurement area and thus decrease the following echo signals by a greater amount than if they had not moved. This factor also occurs in parallel, and the resulting equation for T_2 can be written as follows:

$$\frac{1}{T_2} = \frac{1}{T_{2,bulk}} + \frac{1}{T_{2,surface}} + \frac{1}{T_{2,diffusion}} \quad (4.2)$$

In general, paramagnetic ions in the rock tend to make the fluid nuclei relax much faster than if they had been measured in bulk (Foley, 1996). Due to this, the majority of

the relaxation is done on the matrix surface area via the diffusion of protons to and from it. From this, we can establish two regimes characterized by the rate-limiting step of the process of either the diffusion to and from the surface), or the relaxation on the surface when the fluid molecules get there. In the first case, the relaxation rates are not directly related to the pore size, but by the diffusion rates of the molecule. In this case, a correlation to pore size is not linear. In the second regime, the surface area to volume ratio is the most important factor, as the greater number of sites means a faster relaxation rate. In this regime, the surface effects are dominant, and the surface to volume ratio (and effectively pore size) can be calculated from the transverse relaxation time assuming a given surface relaxivity, as they scale linearly (Brownstein, 1979). Diffusion plays a role in the overall transverse relaxation time via the mechanism described above, but typically is not the dominant factor as it is fast enough when compared to the overall pore size. Therefore, in the realm of petrophysics, we are typically in the surface relaxation rate limiting regime.

Porosity Measurement:

The raw data from a T_2 echo train is a squiggly looking negative exponential curve, and from this data complex calculations called echo-fit mapping can be performed. They're based on fitting the curve with previously decided discrete T_2 values, and then performing an inverse Laplace transformation to get a product series of exponential decays, each with a characteristic T_2 relaxation value. Based on the intensity of each product series a T_2 distribution diagram can be generated and then related to porosity. An example performed here at UT-Austin is shown in Figure 4.6.

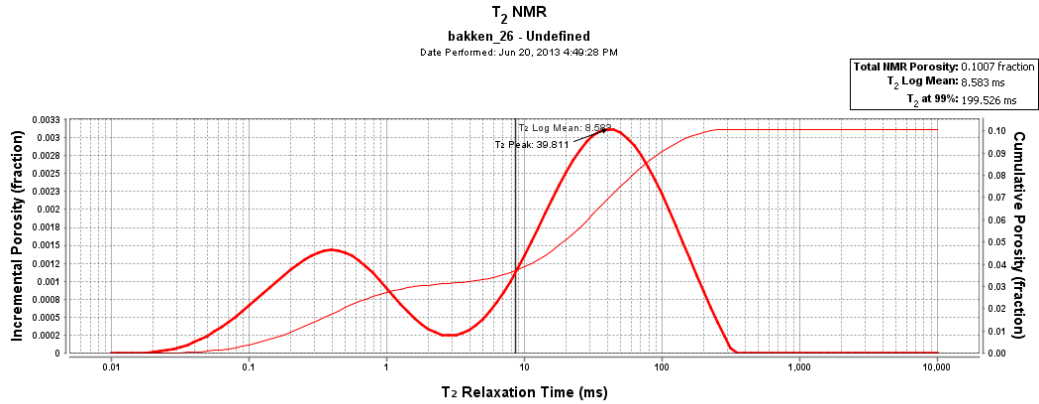


Figure 4.6: Example T₂ distribution diagram using Bakken core

This area under the curve directly represents the porous space of the sample analyzed, as each discrete T₂ value is assigned a given porosity. Given the bulk volume of the sample, the overall porosity can be calculated and has been proven to be quite accurate and robust (Matteson, 2006).

4.1.2 Use of NMR in Unconventionals

The use of NMR in unconventionals as a petrophysical measurement technique are still relatively new. Many of the methods involve the use of data similar to that obtained from the NMR logging tool, and additional data such as the diffusion distribution and T_1 relaxation times which are not normally measured with traditional downhole equipment. Most of these techniques involve the use of bench scale NMR machines for use in core analysis, where time spent on a single scan is less of a factor and signal-to-noise ratio (SNR) can be maximized. Due to this, techniques utilizing two measurements simultaneously can be performed. These typically require an exponential increase in the amount of time it takes to run a single scan.

2D-Mapping

As mentioned above, the use of 2D-mapping for shales is still in its infancy. It served little purpose (and for the large part didn't exist outside of very specialized fundamental NMR research) for conventional formations where fluids could be identified by their T_2 relaxation times alone. The little it was used was namely for identification of very light hydrocarbons where the relaxation times of hydrocarbon and water are very close.

The simplest type of 2D map is Diffusion vs. T_2 . Since diffusion is a parameter that can be measured independent of NMR, it makes this type of map a very strong first step to characterize fluids. Cao Minh et al. in 2012 generated an advanced model for diffusion of different molecules, and overlaid values of diffusion onto the map in order to aid in their identification. An example is shown in Figure 4.7 below.

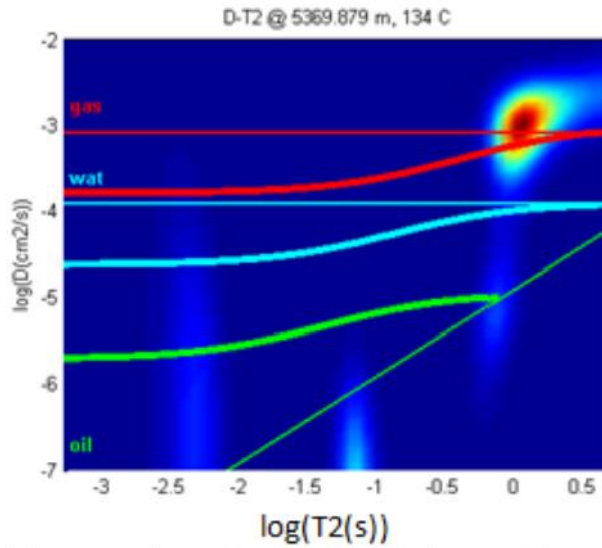


Figure 4.7: Diffusion vs. T₂ Log (Cao Minh, 2012)

Along with an advanced diffusion model, Cao Minh et al. were able to provide insight on the effects of wettability as well. With such small pore volumes, wettability plays a very large role in the type of fluid bound to the surface of the grains. Thus, it will also have a large role in the surface component of the total T₂ measurement.

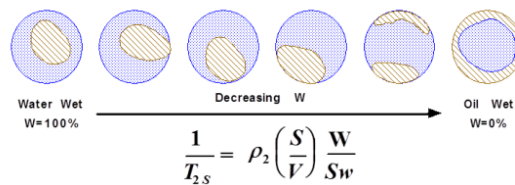


Figure 4.8: Trend of wettability effects (Cao Minh et al., 2012)

Cao Minh et al. in 2012 showed that wettability is a variable that must be taken into consideration when interpreting a given T₂ value. He included a “wettability factor” to the T₂ surface calculation, and the scale of this factor is directly related to the viscosity

of the saturating oil. For light oils this factor is much less pronounced, as lighter oils tend to relax slower. However, for heavy oils, this wettability factor can dominate the T_2 surface term (Cao Minh et al., 2012).

Furthermore, a T_1 vs. T_2 cross-plot can be generated to reveal additional information useful to characterization of formation fluids, especially by taking the ratio of T_1/T_2 . This ratio can be used to identify particular fluids if used in conjunction with T_2 measurements taken. Rylander et al. in 2013 have shown the correlation between this T_1/T_2 and fluid properties in the Eagle Ford shale. In their results, oil in larger pores is shown to have a ratio of roughly one, and will have relatively longer T_1 and T_2 relaxation times due to the smaller effect of the surface relaxation mechanism. Organics such as kerogen and bitumen in nanopores, however, will have a very high T_1/T_2 ratio, but have a relatively low T_2 relaxation time due to the larger influence of the paramagnetic ions on the surface of the pores. This rough correlation is shown in Figure 4.9.

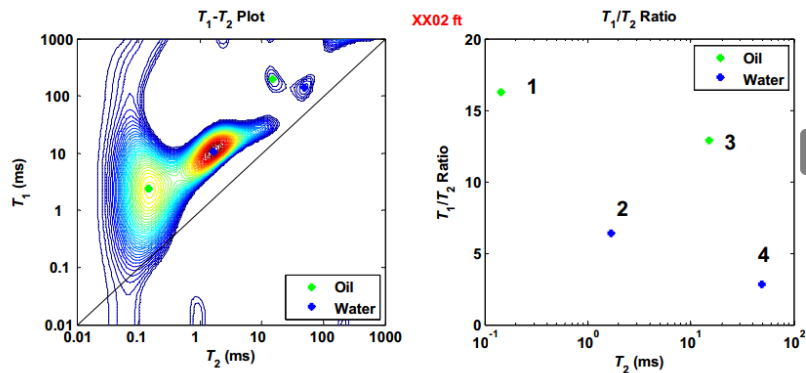


Figure 4.9: Left Plot - T_1 vs. T_2 plot. Right Plot - T_1/T_2 ratio vs. T_2 . (Rylander, 2013)

Solid-Echoes and Visual Emergence of Kerogen via NMR

A very recent emergence is the use of exotic echo-trains in order to better detect the relaxation of the nuclear spins in very short relaxation situations. One such technique is solid-echoes (Washburn, 2013), which has shown some promise in that it is able to refocus the transverse polarization on the y-plane (see Figure 4.2 above for reference). This reduces the loss in signal from the homo-nuclear dipolar coupling (the effect that causes nuclei very close to surface paramagnetic ions to quickly relax) that results from the relatively long T_1 signal and relatively short T_2 signal. The result of this technique is the ability to see with greater intensities lower field relaxations and higher resolution in 2D maps. The work of Washburn et al. in 2013 also includes the use of their solid-echo train technique to analyze the pyrolysis of organics to the maturation of kerogen. In their experiment, they slowly heated a shale sample saturated with decane. As temperature increased, and pyrolysis took place, T_1 vs. T_2 mapping quite evidently showed the emergence of hydrogen bound by kerogen. This is shown in Figure 4.9 (Washburn et al., 2013).

4.1.3 “Single-Scan” vs. “Multi-scan” NMR Techniques

The methods used for NMR core analysis discussed in this thesis fall into two categories:

- 1) Those that attempt to analyze and characterize shale with only a single scan.
- 2) Those that analyze and characterize shale before and after making some type of change to it.

The first category is useful in that it can provide data analogous to what is possible in downhole logging. Therefore, characterizing shale with this method would be useful for formation evaluation. The second category is useful in several ways. First, NMR can be

used to measure the change in the character of the sample as a process is performed on it (e.g. measuring changes as enhanced oil recovery (EOR) techniques are applied). Secondly, if the changes are known on a sample, greater understanding of the measurement using NMR can be achieved. It should be noted that with all measurement techniques, research in the second category must precede usefulness in the first. In general, understanding of NMR measurement in shales is relatively low, therefore the entirety of this thesis is dedicated to research of the second category.

4.2 Characterizing Fluids in Shales with NMR and Py-GC-MS

The method presented below attempts to "cancel out" the effects of the rock by subtracting the NMR responses of T_1 and T_2 2D maps using the same sample but at different sample states, in this case after being heated to different temperatures. These measurements are then compared to results of Pyrolysis-Gas Chromatograph-Mass Spectrometry (Py-GC-MS), in which it is possible to accurately determine the exact composition of the escaping fluid.

Both longitudinal and transverse relaxation times (T_1 and T_2 respectively) are a function of the correlation factor, τ_c , describing the length of time an interaction between two forces exists. For the case of intermolecular dipolar coupling in a fluid, this factor is best described via Debye theory and is given by Equation 4.3 (Bloembergen et al., 1948):

$$\tau_c = \frac{4\pi\mu\alpha^3}{3kT} \quad (4.3)$$

Where μ is the viscosity of the fluid, a is the radius of the molecule, k is Boltzmann's constant, and T is the absolute temperature. This provides a basis that both T_1 and T_2 relaxation times are a function of molecule size and viscosity. Further, in cases of higher τ_c , the dependence of T_1 and T_2 are opposite. T_1 increases with τ_c with a slope approximately equal to 1, and T_2 is reduced with τ_c with a slope approximately equal to negative one as shown in Figure 4.10 (Bloembergen et al., 1948).

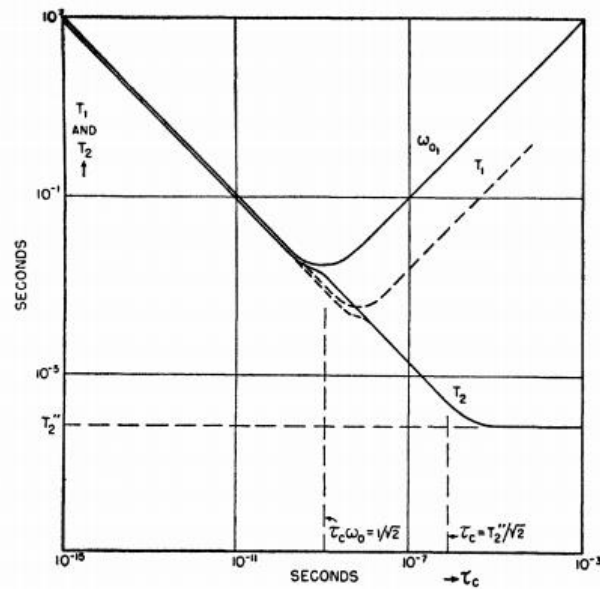


Figure 4.10: Relation of T_1 and T_2 relaxation times to correlation time, τ_c (Bloembergen et al., 1948)

Thus, all else being equal, the ratio of T_1 to T_2 will also increase with correlation time with a slope greater than one as T_1 and T_2 continue to diverge and is shown in Figure 4.11. This is true until the transverse relaxation time reaches its maximum value, at which point T_1/T_2 will only be influenced by T_1 .

Applying this to use in the lab, the T_1/T_2 value should increase with an increase in correlation time, which will remain a value of one for smaller, low-viscosity fluids,

increase rapidly for medium, mid-viscosity fluids, and then increase with a slope of one for larger molecules (Bloembergen et al., 1948). Simply put, for liquid hydrocarbons, we should see an increase in T_1/T_2 with viscosity and molecular size.

4.2.1 Experimental Method

Sample Prep

Only preserved shale samples were used in these experiments to maintain the concentrations of fluids within the cores to as close to in-situ conditions as possible. Each sample was first crushed and then separated with multiple sieve trays. Only sizes between 0.25 and 1 mm (60 mesh and 20 mesh, respectively) were used for the experiment. The pieces of selected size were homogenized, and then set in a desiccator at the appropriate water activity for each sample (Zhou et al., 2013) to recover any water that may have been lost during the crushing process.

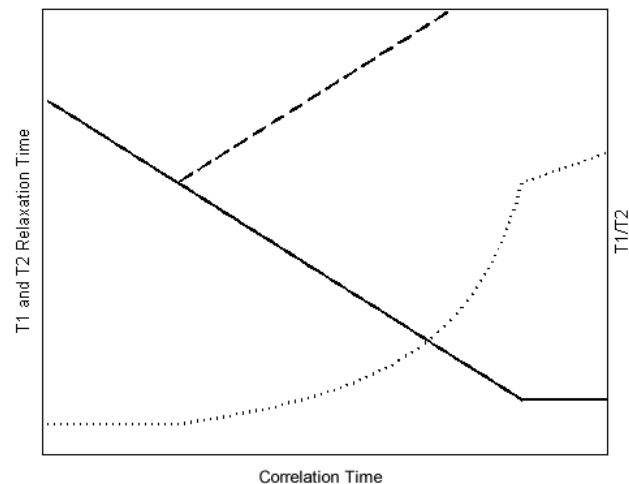


Figure 4.11 Relationship of T_1/T_2 with increasing correlation time

TGA and Py-GC-MS

Afterwards, part of each sample (~40 mg) was analyzed via TGA to ascertain thermal event end points and thus provide set points for Py-GC-MS tests and oven temperatures for each step prior to NMR analysis. TGA was performed using the method detailed in Chapter 2. Analysis was further performed to ascertain the derivative peaks and temperature set points. These are the same temperatures shown in Table 3.1, and are shown again for convenience.

Sample	Step 1	Step 2	Step 3	Step 4
Bakken	200° C	580° C	850° C	1100° C
Eagle Ford	320° C	600° C	860° C	1100° C
Utica	275° C	625° C	850° C	1100° C

Table 4.1 Temperature step end points for the Bakken, Eagle Ford, and Utica

Using another part of the crushed sample (~50 mg), Py-GC-MS was performed using the same sample at each temperature step identified from the TGA procedure as discussed in Chapter 3.

Heating and NMR

After TGA and Py-GC-MS were complete, the remaining portion of the sample (~60 g) was then utilized for NMR measurement after heated to the same temperature steps described above. Each sample was measured via NMR scans before any heating occurred (the entire core was actually measured before crushing as well to confirm continuity). NMR measurements were made using an Oxford GeoSpec2 with a 2.2 Mhz frequency utilizing Green Imaging Technologies (GIT) software for inversion. For all heating steps, the following measurements were taken with parameters listed below:

- T_2 – CPMG measurement, 0.044 ms TE, 1000 ms maximum relaxation time, 32 scans
- T_1 - Inversion recovery measurement, 1000 ms maximum relaxation time, 32 scans
- T_1 & T_2 2D map – Coupled CPMG-inversion recovery measurement, 0.044 ms TE, 1000 ms maximum relaxation time, 32 scans

The heating at each temperature step was performed using the following procedure: 1) Measure sample container weight (crucible). 2) Add sample to container and weigh again. 3) Place sample in oven and heat to set temperature for 8 hours. 4) Turn off oven and cool to 100°C. 5) Remove sample and reweigh. 6) Transfer sample to sealed NMR container and cool to room temperature. 7) Measure sample with NMR and repeat steps 1-7 for each temperature step.

It should be noted that Py-GC-MS is performed under anaerobic conditions (by definition), while the oven heating is performed at atmospheric conditions. This was deemed necessary due to the extreme temperatures used in this particular experiment, and thus the extreme material requirements for constructing an adequate container.

The subtractions between sample states of the NMR T_1 and T_2 2D maps were performed by taking the lower temperature state, and from it, subtracting the NMR porosity from the higher temperature state at each T_1 , T_2 data point. Importantly, all values where the subtraction resulted in a negative value were set to zero. We make the assumption that the majority of this “negative” porosity is the result of the maturation of kerogen from a state with relaxation times too short to be measured with our benchtop NMR. Effectively, this causes the subtracted data to miss hydrocarbons that had transitioned from kerogen all the way to escaping short chain molecules in a single step.

We believe that these "missing hydrocarbons" are not necessary to show a relationship between hydrocarbon characteristics of the volatilized fluid and T_1/T_2 values.

4.2.2 Experimental Results and Discussion

TGA and Py-GC-MS-Analysis

The difference between anaerobic vs. an oxygen rich environment during the two heating processes seems to have little impact upon mass measurements. The left chart in Figure 4.11 below shows a comparison between the Bakken weight measurements taken with both the TGA and the oven. They exhibit similar curve shapes and relatively similar values of normalized weight throughout the heating process. The Eagle Ford and Utica show similar curves with slight differences due to the fact that they contain organic matter. Since the maturation of kerogen is a time-dependent process, the 8 hour heating in the oven vs. the few seconds of heating in the Py-GC-MS does make a small difference.

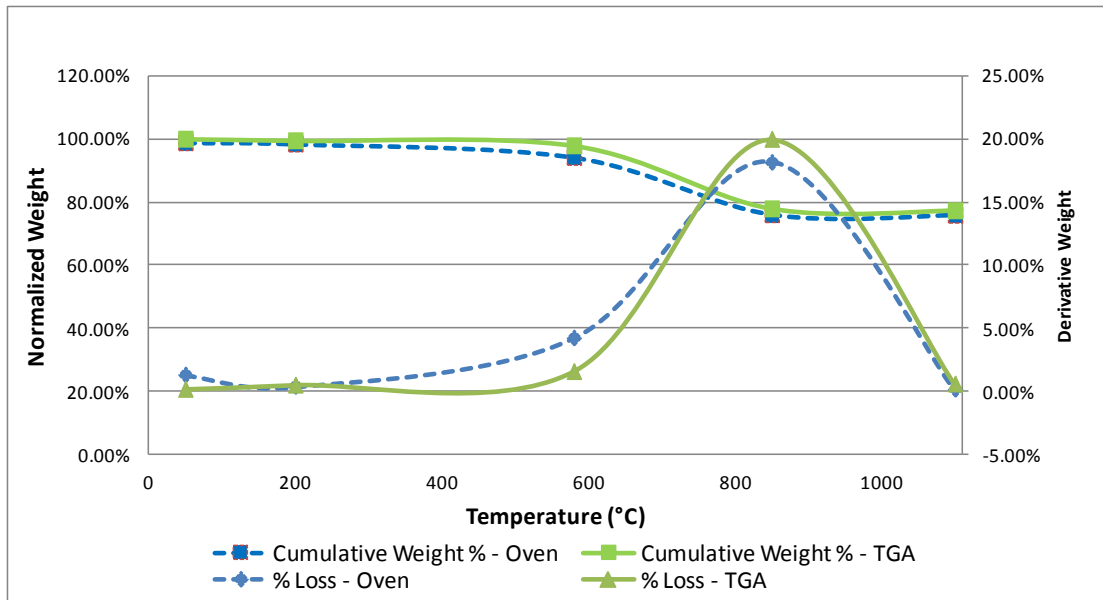


Figure 4.11: Comparison of TGA weight loss to oven weight loss normalized to original weight of the Bakken

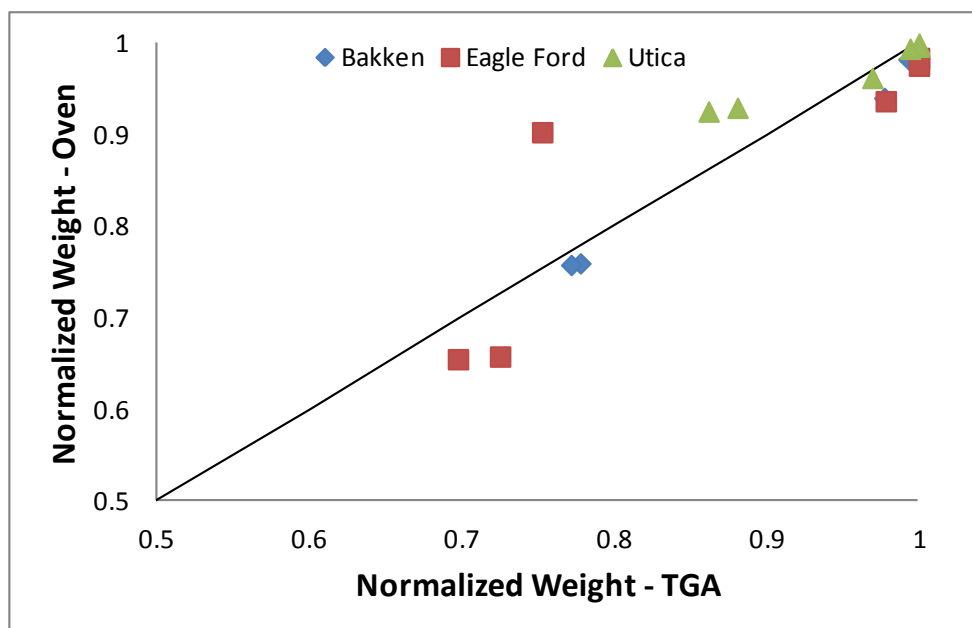


Figure 4.12: Normalized TGA and oven weights for all samples at each temperature step

Figure 4.12 shows the average carbon chain length for each sample at each temperature step. The Bakken exhibits a much greater slope and number of carbon atoms per chain than the other two samples. We explain this with the fact that our Bakken core is from the Middle Bakken, a non-organic rich section, whereas both the Eagle Ford and Utica cores were taken from organic-rich source areas of their respective formations. Therefore, the Bakken, having presumably a less complex pore structure and little to no organic matter to mature, shows a simple increase of chain length due to the lowered boiling point (of course modified by the interacting forces between the pore walls and the hydrocarbon molecules) as temperature is increased. The other two are more complex. As temperature increases, the maturation of kerogen to simpler hydrocarbons allows a later release of shorter molecules. This is especially notable in the $\sim 850^{\circ}\text{C}$ point, where both the Eagle Ford and Utica exhibit a sharp decrease in chain length, whereas the Bakken does not.

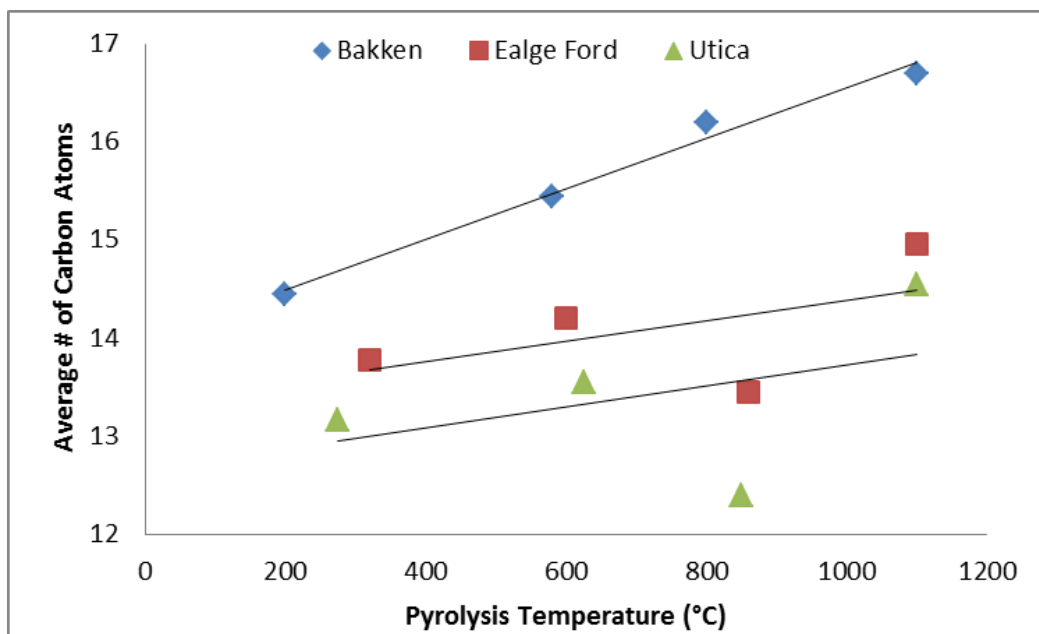


Figure 4.13 Average # of carbon atoms for each temperature step

NMR Results

In general, we saw results consistent with expectations using the subtracted T_1 and T_2 2D maps. High NMR fluid volumes were observed for the initial temperature step as most of the free fluid was lost, and then very small changes in measured NMR fluid volume were observed throughout the higher temperature steps. This is inconsistent with the weights measured from the thermal processes, where the largest jump was observed around 600°C - 800°C. This can be explained by two processes 1) Kerogen maturing and the subsequent vaporization of hydrocarbons in a single step, and 2) The decomposition of carbonates, which is the predominant factor for mass loss in the higher temperature range. Both of these effects would not appear in the T_1 and T_2 subtraction measurements, but would still be reflected as an overall loss of mass.

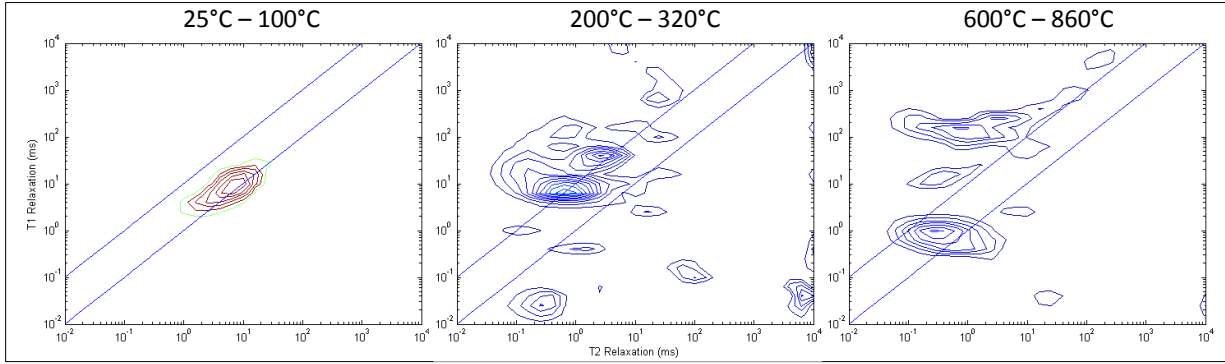


Figure 4.14: T_1 and T_2 map subtractions at progressing temperature steps – Eagle Ford

Figure 4.14 shows an example of this progression with the Eagle Ford shale. The lost fluid for the first temperature step (25°C – 100°C) has an average T_1/T_2 ratio of just greater than one, and a T_2 value of 6-7 ms. This is consistent with observations of these values for free fluid (Coates et al., 1999), which is expected to be the primary component at this temperature step. The second step (100°C – 200°C) shows a reduction in the T_2 value and an increase in T_1/T_2 value for its peak, with an emergence of some higher T_1/T_2 material. This again is consistent with expectations, as T_2 would decrease as fluid loss would be from clay-bound fluid and tighter pores, and we would begin to see the beginning of kerogen maturation (Washburn et al., 2013 (2)). Lastly, the third temperature step (600°C - 860°C) shows a separation between two major components of the effluent fluids, a large peak with a T_1/T_2 of about 6, and another similarly sized peak with a T_1/T_2 close to 100. This is interpreted to be due to extreme cracking of the already matured hydrocarbons, indicated by the low T_1/T_2 peak. The high T_1/T_2 peak is interpreted to be very viscous, organic solids that have matured only just enough to become measurable with NMR.

This trend is present for all three of the samples, with an increase in the geometric mean T_1/T_2 ratio of the subtracted T_1 and T_2 data. However, at higher temperatures, the Bakken sample exhibits a much greater increase in the T_1/T_2 ratio compared to the Eagle Ford and Utica. This is best shown visually at the $\sim 600^\circ\text{C}$ point, shown in Figure 4.15 below.

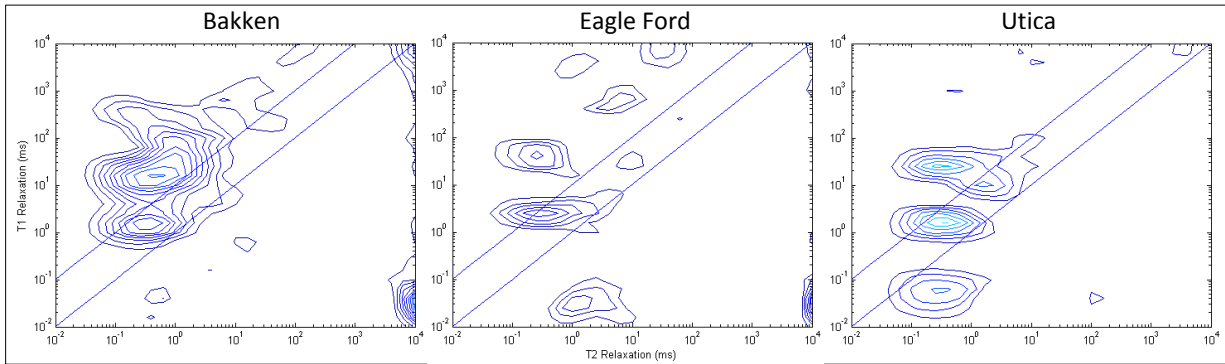


Figure 4.15: Comparison of Bakken, Eagle Ford, and Utica T_1 and T_2 map subtractions at $\sim 600^\circ\text{C}$ end point temperature

A large majority of the signal from the Bakken is at a T_1/T_2 ratio greater than 10, while the Eagle Ford and Utica samples still have a significant amount below ten. When the geometric means of the T_1/T_2 ratios are calculated and plotted to the maximum temperature of each step, a trend appears that is similar to that shown above with number of carbon atoms. These results are shown in Figure 4.16 below.

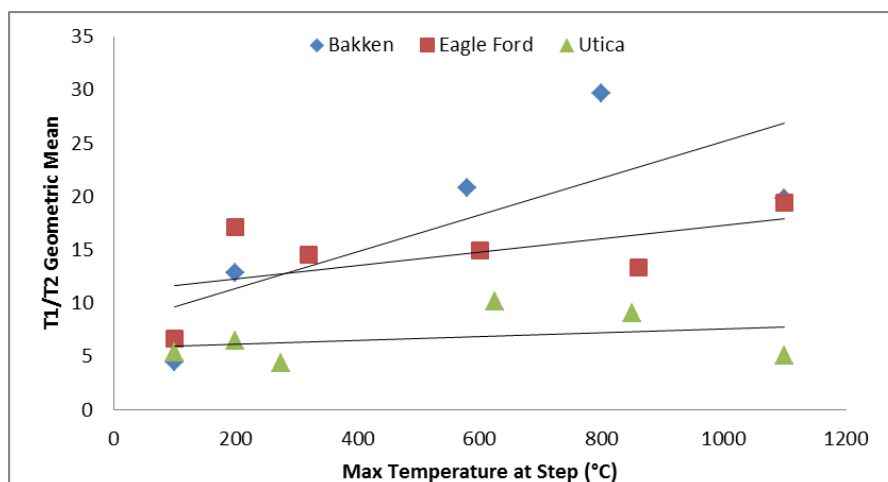


Figure 4.16: Trend of T_1/T_2 geometric mean for each temperature step

Interesting to note is the relative position of the trends compared to those from Figure 4.13 (# of carbon atoms). They are quite similar in position and slope for each formation, with the Bakken having both the highest values and slope, and the Eagle Ford in the middle with a relatively similar slope to the Utica which is on the bottom. The notable exception to this trend is that the Bakken and Eagle Ford trends cross at lower temperatures while this is not the case in the Py-GC-MS/TGA data.

Additionally, T_1/T_2 values plotted against the corresponding average chain length for each temperature step can be compared. This is illustrated in Figure 4.17. A rough correlation does emerge when looking at all of the data points, although it must be noted that while the Bakken and Eagle Ford hold this trend individually, the Utica does not. Based on the general shape of the trend, it appears that a slight curvature is present, similar to that observed in the relationship between T_1/T_2 and τ_c .

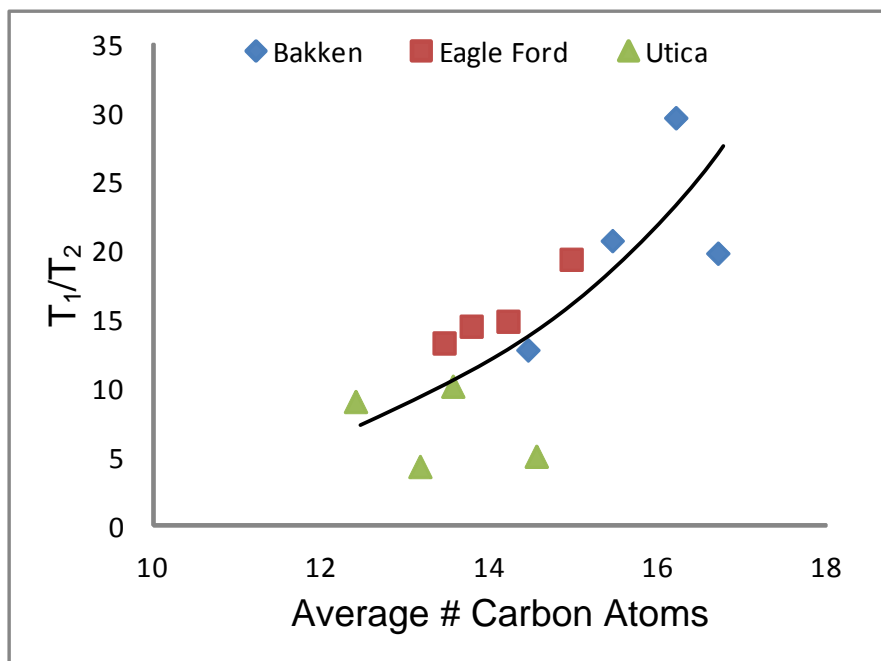


Figure 4.17: T_1/T_2 geometric means plotted against the average # of carbon atoms at each temperature step

Based on the Debye theory presented above, likely causes for this overall increase in T_1/T_2 are the increased molecular length and increased viscosity of the fluids. However, it is beyond the scope of this thesis to speculate on the relative importance of each.

Overall, the data imply a correlation between the differential T_1 and T_2 2D maps and the measurements performed via Py-GC-MS. Thus, it appears that the process of subtracting T_1 and T_2 2D maps has the potential to reveal valuable information on the properties of the fluid itself, in a sense, cancelling out the effects caused by the rock. The next steps in this work will be focused on applying this technique to a smaller range of temperatures in the 25°C - 200°C range. This will further mitigate the effects of maturing kerogen and provide an environment less conducive to further cracking of hydrocarbons,

as well as having the added benefit of focusing on hydrocarbons more likely to be produced. Additionally, work to perform the subtraction prior to the inversion of the NMR signal is desirable.

4.2.3 Conclusions

A new method called the differential T_1 , T_2 method is proposed to investigate the fluid content of shales. In this method the relaxation times T_1 and T_2 are measured with a NMR for shale samples that have been heated to different temperatures. The difference between these measurements reflects the changes in the fluid content of the sample as it is heated. From the theoretical basis of T_1/T_2 and its relationship with correlation time, we present a method to characterize the hydrocarbon fluid within shales based on its molecular size and viscosity by taking these subtracted T_1 and T_2 2D maps to represent the fluid leaving the sample over a given temperature step. Through laboratory analysis, we have correlated the increasing chain length of hydrocarbon molecules analyzed via Py-GC-MS and TGA to increasing T_1/T_2 values. These results lead to a conclusion that T_1/T_2 values for subtracted data can be a simple but valuable indicator of hydrocarbon characteristics. Future work will involve application of this method to lower temperatures within a smaller range to more accurately identify shorter chain hydrocarbons and further mitigate the effects of maturing kerogen in the subtraction.

5 Using Multiple Techniques for Petrophysical Calculations in Shales

While TGA, Py-GC-MS, and NMR are quite useful in their own regard, perhaps the best information can be obtained by combining the results of two or three of them. Several methods for making petrophysical measurements in shales are presented below, including first the calculation of fluid saturations through the use of Py-GC-MS and TGA, and second the characterization of fluid change using NMR and confirmed with Py-GC-MS.

5.1 Py-GC-MS to Determine Producible Fluid Saturations

The most powerful method utilizing Py-GC-MS is possibly the ability to determine oil and water saturations. Combined with the ability of TGA to determine the difference between free and clay bound fluids, it becomes possible to estimate the amount of free oil in the sample. Using the Eagle Ford as an example, this method will be explained in detail.

5.1.1 TGA and Low Temperature Range Selection

As mentioned in Section 3.2.1, the first step is to analyze the sample via TGA, and select the appropriate temperature range representative of free fluid. It should be noted that this is a different Eagle Ford sample than was used as an example in Chapter 2. This is due to the two experiments being performed at two different times. The sample used for the TGA and Py-GC-MS in this chapter are plugs taken adjacent to each other from a preserved whole core. Based on the peak from the TGA, a good cut-off point for the low temperature range appears to be around 160°C, an example of this selection is shown in Figure 5.1.

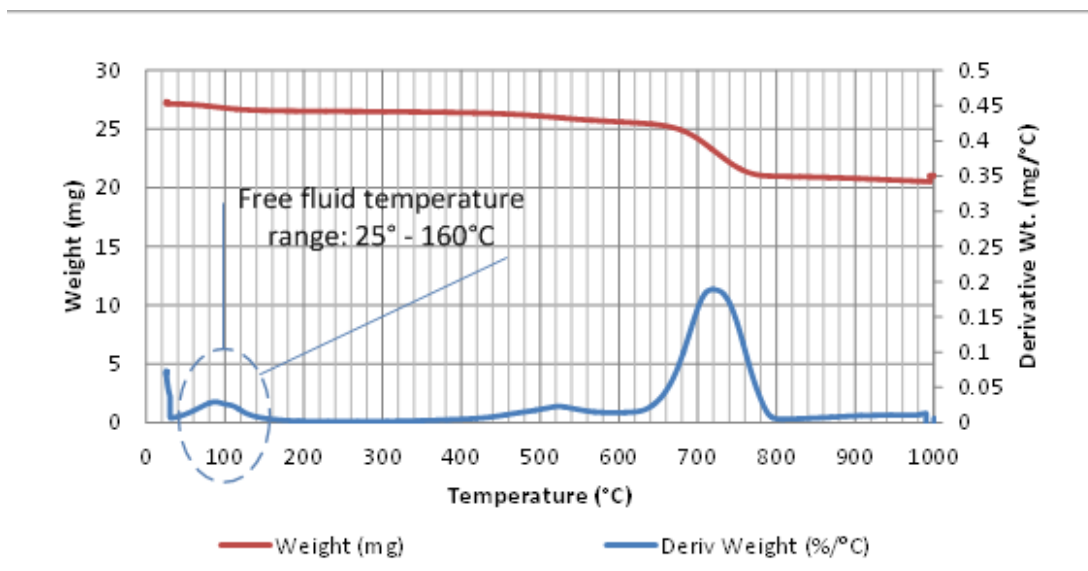


Figure 5.1: TGA of Eagle Ford sample showing selection criteria for low temperature range

5.1.2 Py-GC-MS and Conversion to wt. %

Next, Py-GC-MS is performed at the temperature identified by TGA, in this case 160°C. The chemical identification data is generated by the NIST database, and then correlated with the abundance to give a wt. % relative to the fluid released for each molecule. A sample of this data is shown in Figure 5.1. After this, an in-house written program identifies the molecular name and assigns it a number of carbon atoms and density. The now categorized data can then be shown graphically. This is shown for the Eagle Ford sample in Figure 5.2.

Eagle Ford - 160°C			
Retention Time (min)	NIST Best Match Compounds	Match Factor ¹	Abundance (10 ⁶)
1.033	Carbon monoxide	663	8.43
1.217	Water	838	67.47
2.834	Oxygen	510	15.66
10.552	Tridecane	866	4.95
10.619	2-Hexyl-1-octanol	794	1.40
10.650	Oxirane, dodecyl-	760	1.29
10.705	Tridecane, 6-methyl-	769	2.70
10.740	5-Tetradecene	761	3.03
10.803	4-Tetradecene	767	3.38
10.856	2-Ethyl-1-dodecanol	679	5.57
10.919	1,9-Tetradecadiene	761	4.23
11.009	Tetradecane	738	11.35
11.061	2,3-Dimethyldodecane	784	5.19
11.114	Tridecane, 2-methyl-	873	11.55
11.182	Tridecane, 3-methyl-	823	6.58
11.225	Tetradecane	830	13.66
11.287	Tetradecane	752	6.56
11.373	2-Hexyl-1-octanol	810	8.18
11.446	Tetradecane	862	27.86
11.520	Pentadecane	796	7.77
11.567	Hexadecane	757	6.11
11.609	1-Decanol, 2-hexyl-	698	7.44
11.715	Pentadecane, 4-methyl-	712	4.28
11.759	Oxirane, tetradecyl-	736	10.34
11.845	Tridecane, 5-propyl-	704	14.69
11.922	Tridecane, 5-propyl-	768	8.54
11.959	Hexadecane	862	11.27
12.030	Pentadecane, 2-methyl-	837	10.87
12.090	E-2-Hexadecacen-1-ol	723	8.92
12.158	Decahydro-4,4,8,9,10-pentamethylnaphthalene	723	2.95
12.274	Heptadecane	799	21.86
12.329	Heptadecane	841	6.07
12.636	Tetradecane, 2,6,10-trimethyl-	814	4.91
12.683	Tetradecane, 2,6,10-trimethyl-	811	2.43
12.757	Cyclohexane, 1,1'-(1,5-pentanediy)bis-	758	3.71
12.832	Hexadecane, 4-methyl-	829	4.60
12.985	Tetradecane, 2,6,10-trimethyl-	780	1.71
13.058	Octadecane	887	4.22

Table 5.1: Py-GC-MS output data showing retention time in the GC, the molecular identification via the NIST database, the match factor, and the abundance

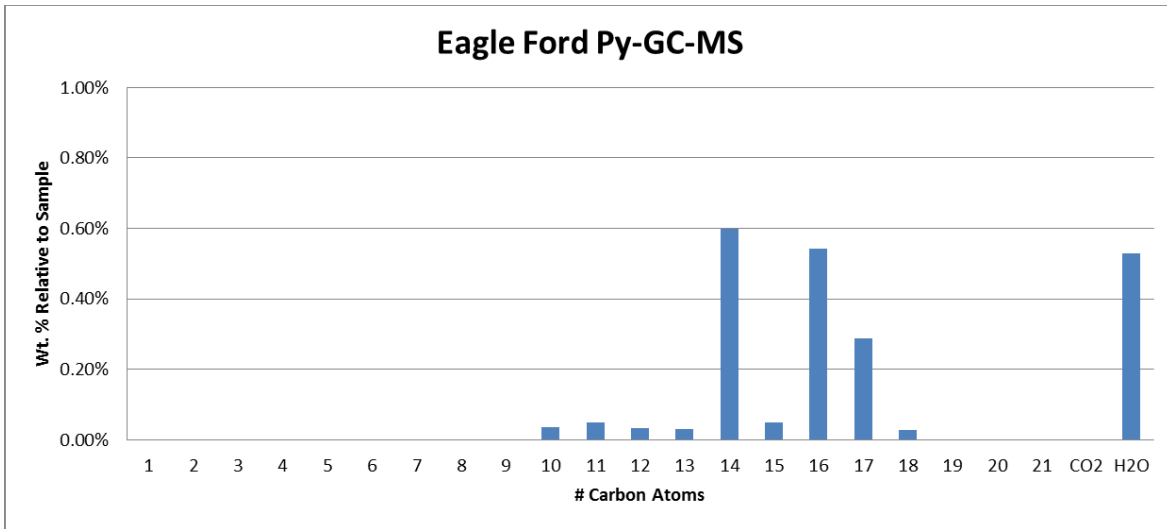


Figure 5.2: Molecular distribution by weight relative to the sample

Next, the wt. % hydrocarbon vs. water and CO₂ can be calculated, and an overall oil and water saturation can be calculated for the temperature step. This is shown in Table 5.2 with the associated volume % assuming a water density of 1 g/mL and 0.8 mg/L for oil. Lastly, the water concentration needs to be corrected based on the amount of clay present in the sample. This clay-bound water will still show up at the 160°C point, but can be subtracted out by knowing the clay concentration and using a calibrated clay standard as discussed in Chapter 2.

Component	Weight % relative to fluid	Volume %	Weight % relative to sample, ω_{total}
Oil	76.4	81.1	1.852%
Water	23.6	18.9	0.573%

Table 5.2: Weight and volume distribution of oil and water for the Eagle Ford uncorrected for clay-bound water

Calculating the amount of clay-bound water to be corrected from a given sample calculation is given by Equation 5.1.

$$\omega_{clay-bound} = \sum_n \frac{(M_{n,initial} - M_{n,160^\circ C})\omega_n}{M_{n,initial}} \quad (5.1)$$

Where $M_{n, initial}$ is the initial weight of the swelling clay n in the TGA, $M_{n, 160^\circ C}$ is the weight of the swelling clay n in the TGA at $160^\circ C$, ω_n is the weight fraction of clay n in the shale sample, and $\omega_{clay-bound}$ is the weight fraction of clay-bound water in the sample. Thus, the calculation of the weight fraction of water corrected for the clay is given simply by Equation 5.2.

$$\omega_{free\ water} = \omega_{total\ water} - \omega_{clay-bound} \quad (5.2)$$

The results of this calculation for the Eagle Ford are shown in Table 5.3 below using 5.7% by weight smectite, and 7.3% illite.

Component	ω_{total}	$\omega_{clay-bound}$	ω_{free}	Saturation in Free Fluid
Oil	1.852%	0%	1.852%	100%
Water	0.573%	0.612%	-0.039%	0%

Table 5.3: Weight fractions relative to the total sample of the total, clay-bound, free fluids, and the resulting saturations

The results show that the entirety of the water in the vaporized fluid at $160^\circ C$ can be attributed to clay-bound water. This is a very reasonable result for several reasons. First, the shale is known as a source rock, and very little water would be expected in free

form, and second, much of the free water existing in larger pores may have been lost in the crushing process.

The results of this calculation for the other two shales is shown in Table 5.4 below.

Sample	S_o	S_w
Bakken	88%	12%
Eagle Ford	100%	0%
Utica	97%	3%

Table 5.4: Free fluid oil and water saturations for the Bakken Eagle Ford and Utica samples

6 Conclusions

Due to the severely different characteristics of shales compared to conventional reservoir rocks, it is necessary to utilize previously unused methods for petrophysical measurements. This work presented applicable methods involving Thermal Gravimetric Analysis (TGA), Pyrolysis Gas Chromatography Mass Spectrometry (Py-GC-MS), and Nuclear Magnetic Resonance (NMR). Individually, each has merit and can provide useful information. TGA can provide confirmation of mineralogy to XRD techniques and analyze water saturations related to the free fluids in the sample. Py-GC-MS gives accurate identification of components of vaporized fluid, and NMR can provide a wide array of useful information relating to viscosity and chain length.

However, much greater understanding can be achieved by utilizing multiple techniques combined. Examples of this include the use of TGA and Py-GC-MS together to analyze the weight percent of each component in a fluid relative to the total sample weight and the use of NMR and Py-GC-MS to show the relationship between hydrocarbon chain length and T_1/T_2 ratio.

Overall, the conclusions of this work are best understood when judged against the original objectives which are shown again below:

1. Determine the amount of producible oil in a given core sample of shale or tight rock.
2. Determine the oil and water saturations of the free fluid (producible fluid).
3. Estimate the porosity (free and bound) of the rock sample.
4. Characterize the producible fluid.

Number 1 can be calculated using TGA, and corrected using Py-GC-MS. In shale samples, nearly all of the non-clay bound fluid can be assumed to be hydrocarbon to make this approximation. However, we feel that the most accurate representation of this number can be achieved using the most recent models of Pyrolysis Rock Evaluation as mentioned in Chapter 1. This method has had considerably more research, and newer models can now adequately handle the high carbonate concentrations. Number 2, determining the saturations of the producible fluid, can be calculated using the method presented in Chapter 5. In this instance it is necessary to use both TGA and Py-GC-MS along with calibrated clay samples to correct for the fluid in clay. Determining the free and bound porosity of the rock is not well covered in this Thesis, but other research for this exists especially in the realm of NMR (Daigle, 2014). Lastly, characterization of the producible fluid is performed by both ascertaining the saturations (Chapter 5), and analyzing hydrocarbon chain length via NMR (Chapter 4).

The next logical step for this research is the application of the fundamental understanding of these measurements into useful experiments. An obvious example of this is the use of NMR T_1/T_2 ratio to measure the progress of enhanced oil recovery techniques. The change in T_1/T_2 ratio would signal the effective release of shorter hydrocarbon molecules. This would be useful as most measurement techniques for this are invasive and would ruin the experiment. Another possible use, as mentioned in Chapter 2, is the utilization of TGA to analyze drill cuttings. Due to its low cost and ease of use, the technique could feasibly be used to further optimize the depth at which to drill the lateral. This would be most applicable to plays where a large drilling program is expected. Probably the most useful application and implication of this work, however, is

the saturation of the free fluid within a given sample. Many petrophysical calculations utilize fluid saturation to determine recoverable reserves, which is a major component in the overall valuation of an oil and gas play.

Appendices

A1: Hydrocarbon Boiling Points

Chemical name	Carbon Atoms	BP (°C)
Cyclopentene	5	45
1-Hexanol	6	157
2-Pyrrolidinone, 1-ethenyl-	6	92
Benzene	6	80
(5-Methylcyclopent-1-enyl)methanol	7	176
1-Heptene	7	93
2-Hexene, 5-methyl-, (E)-	7	88
3-Heptene, (E)-	7	95
3-Methyl-4-propenyl-oxetan-2-one	7	181
3-Methylenecyclohexene	7	114
cis-3-Methylcyclohexanol	7	170
Cyclohexane, methyl-	7	101
Heptane	7	98
Toluene	7	111
1,5-Dimethyl-1,4-cyclohexadiene	8	133
1-Heptanol, 6-methyl-	8	179
1-Octene	8	122
2-Octene	8	125
3,4-Dimethyl-2-hexene (c,t)	8	114
3-Heptene, 3-methyl-	8	119
3-Octene, (E)-	8	121
cis-1-Butyl-2-methylcyclopropane	8	120
Cyclohexanone, 3-ethyl-	8	185
Ethylbenzene	8	136
Heptane, 2-methyl-	8	117
Hexane, 3-ethyl-	8	117
Octane, 2-chloro-	8	173
o-Xylene	8	144.4
p-Xylene	8	138.35
trans-1-Butyl-2-methylcyclopropane	8	119
1-Nonene	9	#N/A
2,3-Dimethyl-3-heptene, (Z)-	9	139
2-Indanol	9	120
2-Nonene, (E)-	9	150
4-Nonene	9	145

5-Methyl-5-octen-1-ol	9	211
Benzene, (1-methylethyl)-	9	151
Benzene, 1,2,3-trimethyl-	9	175
Benzene, 1,2,4-trimethyl-	9	169
Benzene, 1,3,5-trimethyl-	9	164.7
Benzene, 1-ethenyl-2-methyl-	9	170
Benzene, 1-ethyl-3-methyl-	9	158
cis-2-Nonene	9	150
Cyclohexane, 1,2,3-trimethyl-	9	143
Cyclohexane, propyl-	9	#N/A
Cyclopropane, 1-methyl-2-pentyl-	9	145
Indane	9	175
Nonane	9	151
Nonane, 1-chloro-	9	201
trans-1,3-Diethylcyclopentane	9	149
1-Decene	10	170
1H-Indene, 1-methylene-	10	216
1-Octanol, 3,7-dimethyl-	10	213
2,4-Dimethylstyrene	10	69
2-Cyclohexen-1-ol, 2-methyl-5-(1-methylethenyl)-	10	226
2-Octene, 2,6-dimethyl-	10	163
2-Octene, 3,7-dimethyl-, (Z)-	10	163
4-Decene	10	169
5-Decene, (E)-	10	171
Benzene, 1,2,3,4-tetramethyl-	10	203
Benzene, 1,2,3,5-tetramethyl-	10	199.2
Benzene, 1,2,4,5-tetramethyl-	10	191
Benzene, 1-methyl-2-(1-methylethyl)-	10	178
Benzene, 1-methyl-2-propyl-	10	186
Benzene, 1-methyl-4-(1-methylethyl)-	10	176
Benzene, 4-ethyl-1,2-dimethyl-	10	190
Cyclohexane, 1,1,2,3-tetramethyl-	10	155
Nonane, 3-methyl-	10	167.9
Nonane, 4-methyl-	10	166
Octane, 2,6-dimethyl-	10	160
Octane, 3,6-dimethyl-	10	159
1-Chloroundecane	11	242
1-Decanol, 2-methyl-	11	211
1-Undecanol	11	146
1-Undecene	11	193
2(3H)-Furanone, 5-heptyldihydro-	11	164

2-Decene, 3-methyl-, (Z)-	11	190
5-Undecene	11	191
6,7-Dimethyl-3,5,8,8a-tetrahydro-1H-2-benzopyran	11	254
Benzene, 1-ethyl-2,4,5-trimethyl-	11	213
Benzene, 1-methyl-4-(1-methylpropyl)-	11	196
Benzene, 2,4-diethyl-1-methyl-	11	206
Cyclohexane, pentyl-	11	202
Cyclopropane, 1-pentyl-2-propyl-	11	191
Decane, 2-methyl-	11	189
Decane, 3-methyl-	11	189
Nonane, 2,3-dimethyl-	11	165
Nonane, 2,6-dimethyl-	11	181
Undecane	11	196
1-Dodecene	12	213
1-Octanol, 2-butyl-	12	145
2,3-Dimethyldecane	12	208
2,6-Dimethyldecane	12	201
2-Dodecene	12	216
3-Dodecene, (E)-	12	212
Benzene, (3,3-dimethylbutyl)-	12	192
Cyclododecane	12	239
Decane, 2,5-dimethyl-	12	199
Dodecane	12	216.2
Dodecane, 1-chloro-	12	260
Naphthalene, decahydro-2,3-dimethyl-	12	218
Undecane, 3-methyl-	12	211
Undecane, 5-methyl-	12	170-195
1,1,6,6-Tetramethylspiro[4.4]nonane	13	220
1,11-Tridecadiene	13	231
1-Dodecanol, 2-methyl-	13	261
1-Tridecanol	13	#N/A
1-Tridecene	13	232
2-Undecanone, 6,10-dimethyl-	13	244
2-Undecene, 2,5-dimethyl-	13	226
9-Undecenol, 2,10-dimethyl-	13	284
Dodecane, 2-methyl-	13	227
Nonane, 5-butyl-	13	216
Tridecane	13	235
Undecane, 2,4-dimethyl-	13	220
Undecane, 2,5-dimethyl-	13	219

Undecane, 2,6-dimethyl-	13	219
Undecane, 6-ethyl-	13	222
2-Hexyl-1-octanol	14	275
Cyclotetradecane	14	281
Dodecane, 4,6-dimethyl-	14	236
Tetradecane	14	253
Tridecane, 2-methyl-	14	245
Tridecane, 3-methyl-	14	248
Tridecane, 4-methyl-	14	247
Dodecane, 2,6,10-trimethyl-	15	249
Tetradecane, 2-methyl-	15	262
1-Decanol, 2-hexyl-	16	304
2,5-Furandione, 3-dodecyl-	16	376
2-Dodecen-1-yl(-)succinic anhydride	16	348
Hexadecane	16	287
Pentadecane, 4-methyl-	16	281
Pentadecane, 5-methyl-	16	281
tert-Hexadecanethiol	16	329
Tetradecane, 2,5-dimethyl-	16	274
Tetradecane, 6,9-dimethyl-	16	271
Tridecane, 5-propyl-	16	272
Undecane, 5-ethyl-5-propyl-	16	265
1-Hexadecanol, 2-methyl-	17	318
7-Methyl-Z-tetradecen-1-ol acetate	17	345
Heptadecane	17	302
Hexadecane, 2-methyl-	17	291
Tetradecane, 2,6,10-trimethyl-	17	281
Acetic acid, chloro-, hexadecyl ester	18	356
Heptadecane, 2-methyl-	18	305
Heptadecane, 3-methyl-	18	313
Heptadecane, 8-methyl-	18	306
Octadecane	18	317
Oxirane, hexadecyl-	18	146
Nonadecane	19	330
Eicosane	20	342
Ethanol, 2-(octadecyloxy)-	20	413
Hexadecane, 2,6,10,14-tetramethyl-	20	322
Heneicosane	21	100
Docosane	22	368
Heptadecane, 9-hexyl-	23	397

A2: Structures of Gibbsite and Silica Sheets and The Arrangement for Different Clays

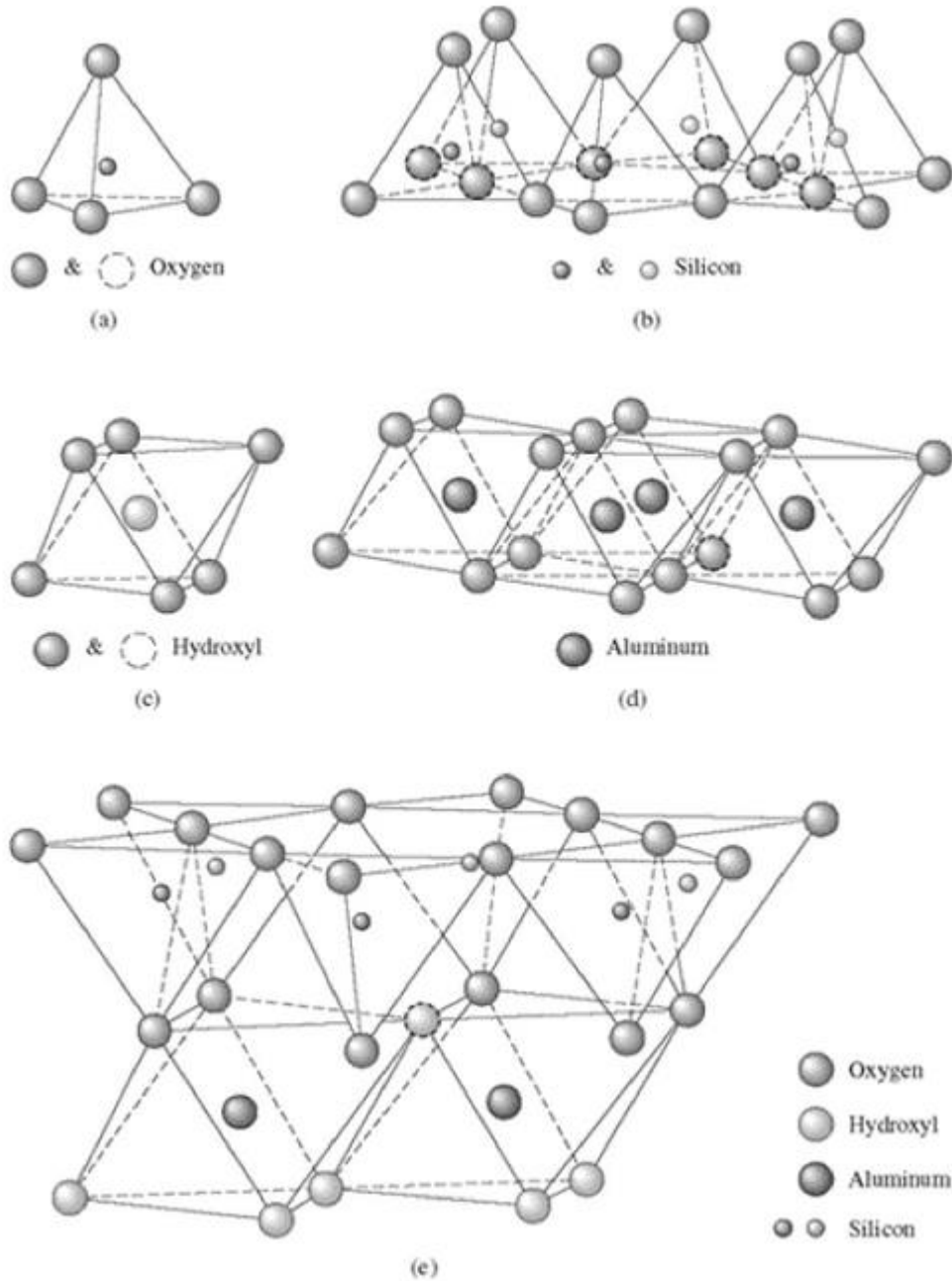


Figure 0.1: A) Single silica tetrahedron B) Silica tetrahedral sheet. C) Al-Octahedron. D) Al-Octahedral sheet. E) Combination of Si-tetrahedral and Al-octahedral sheets (after Das, 2012)

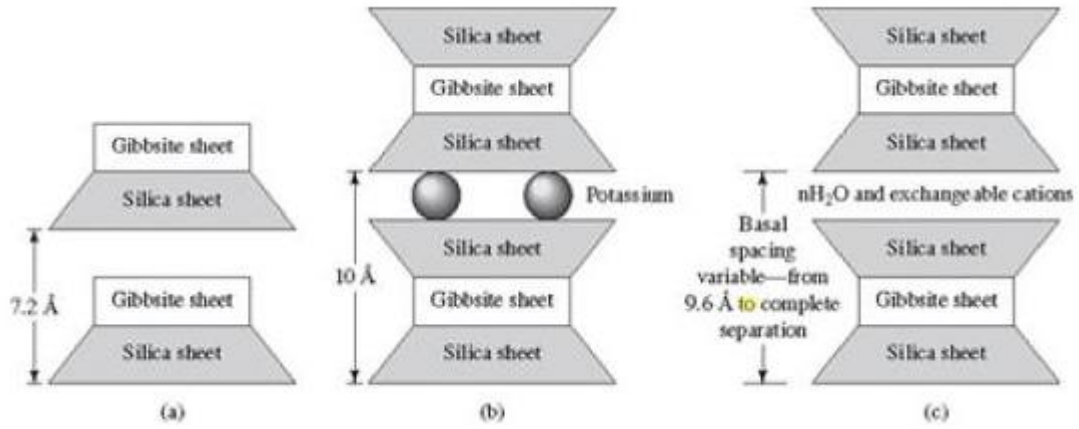
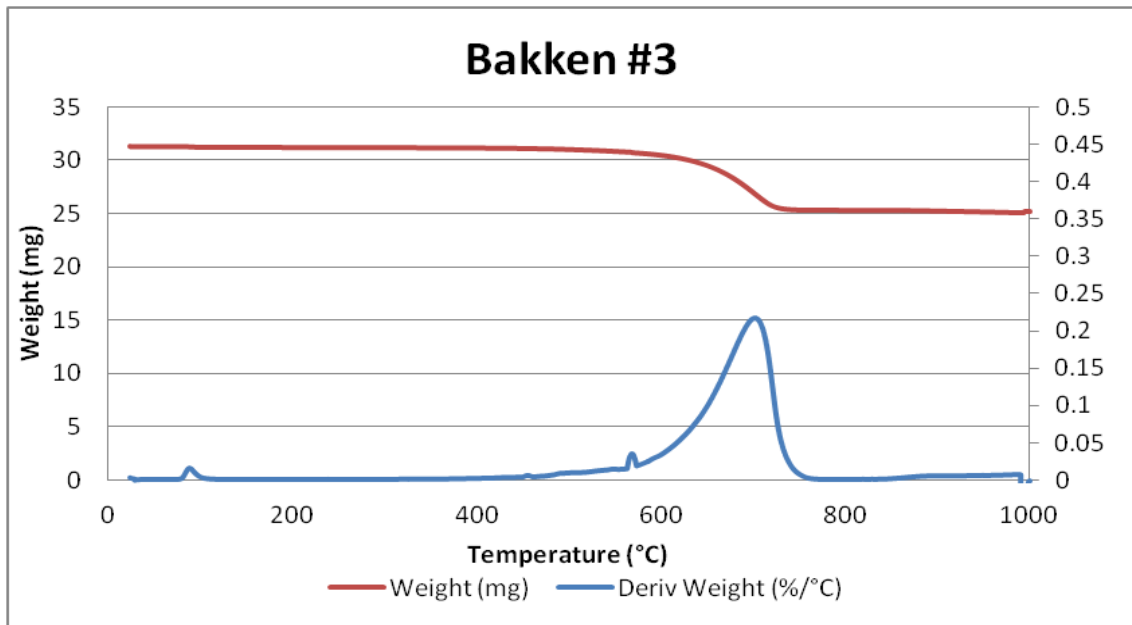
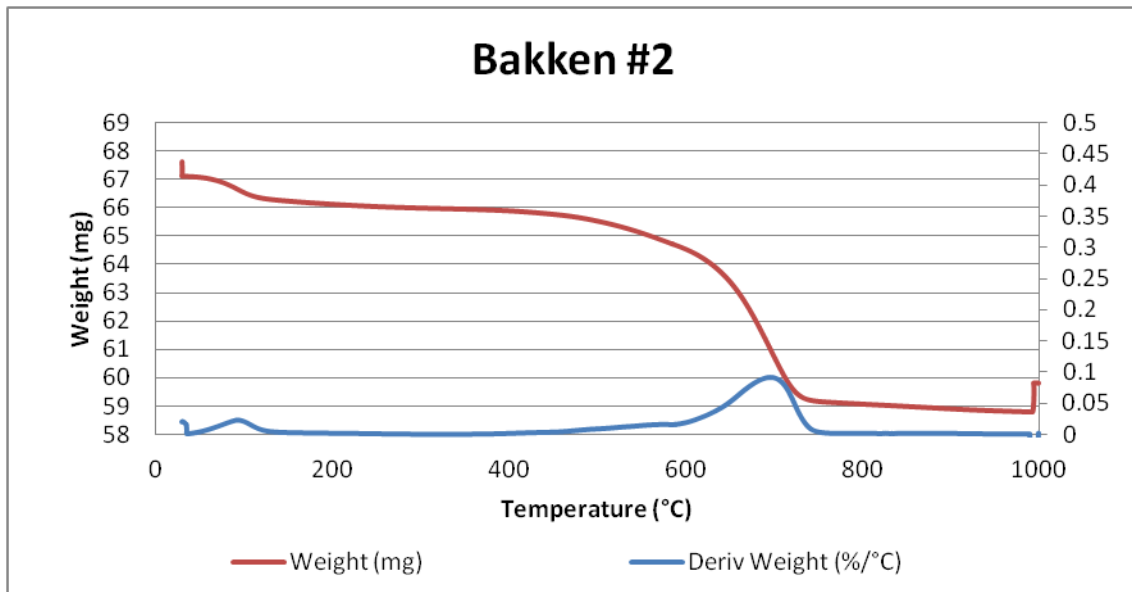
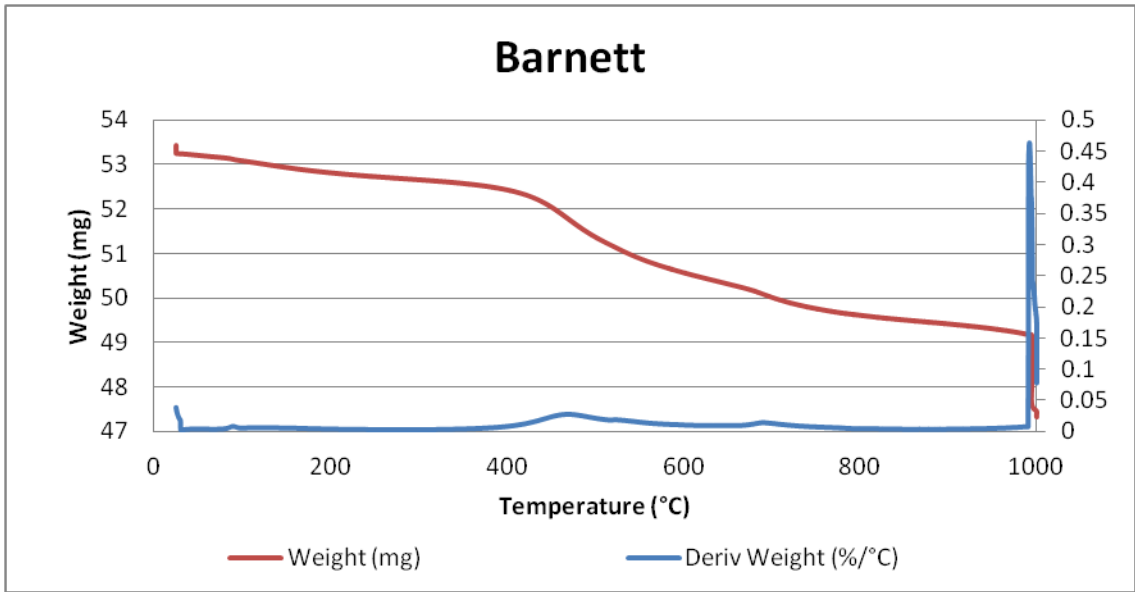
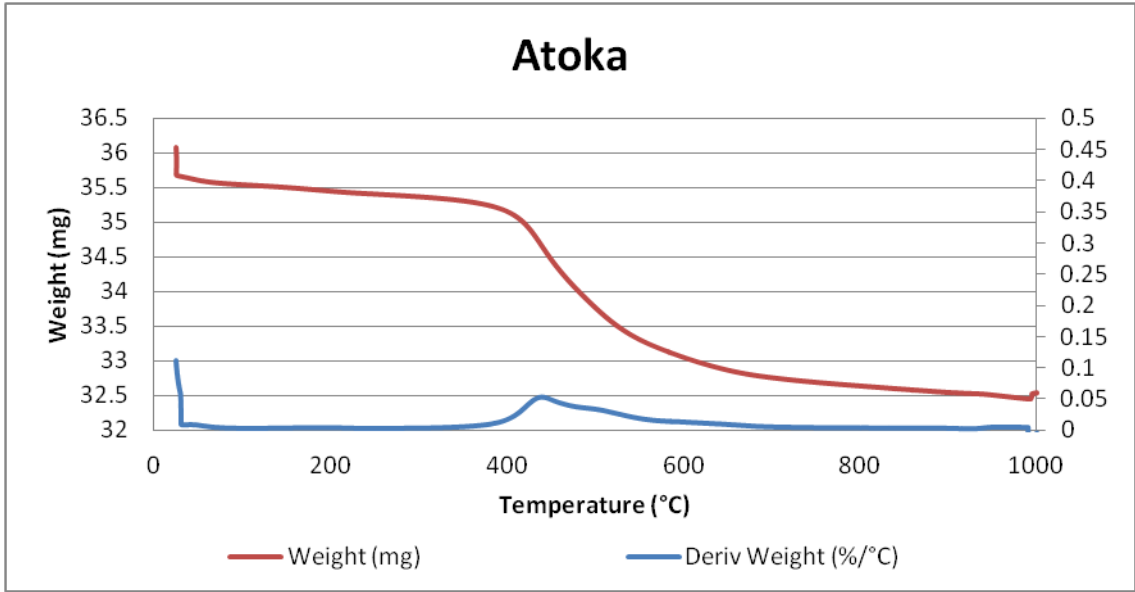
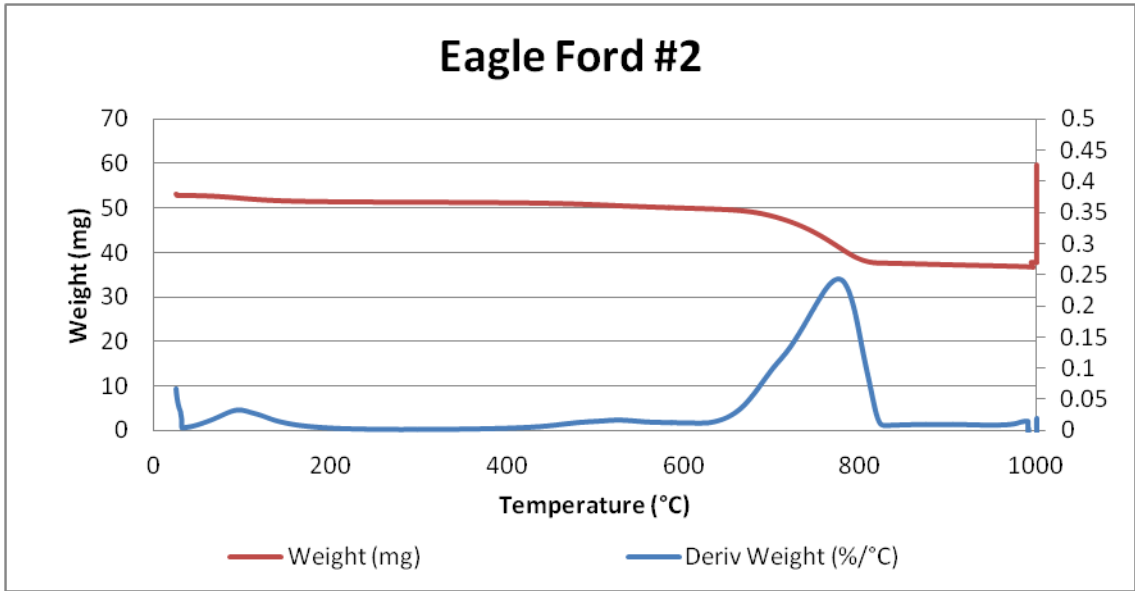
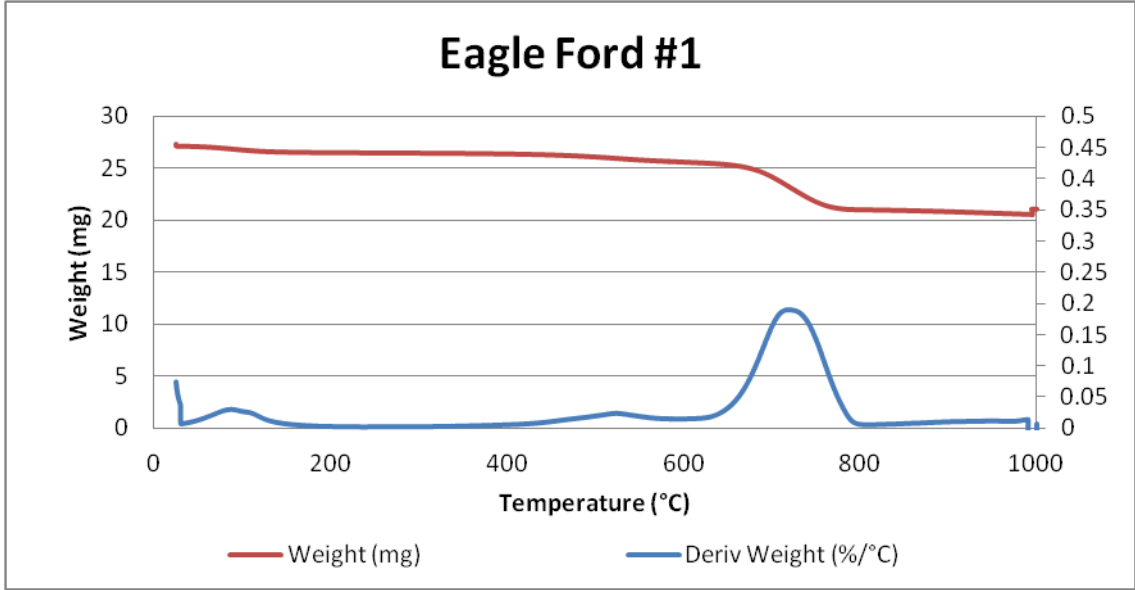


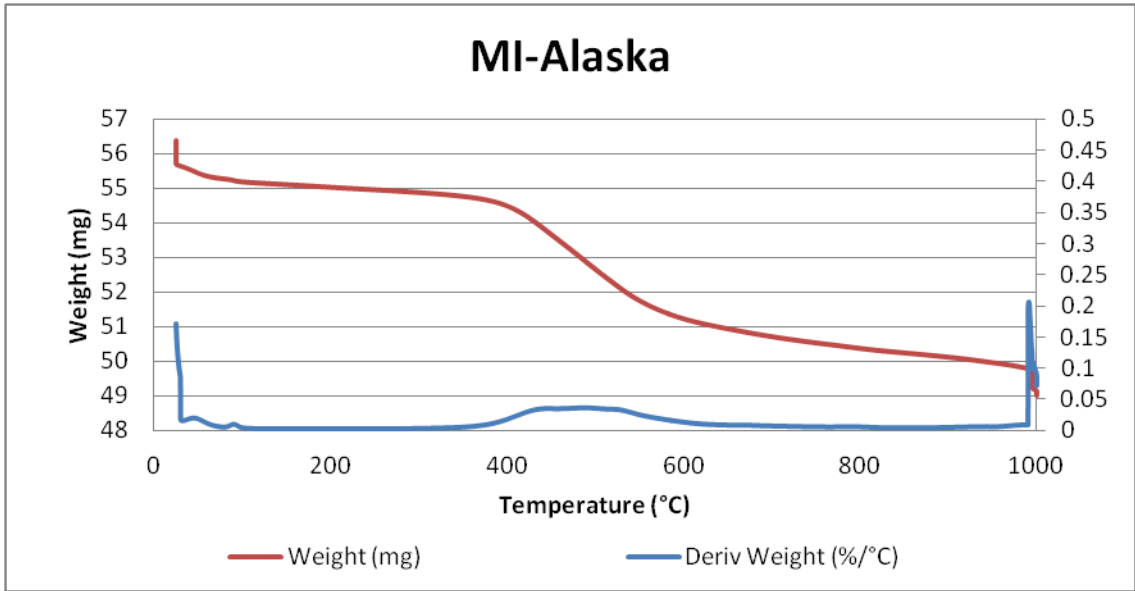
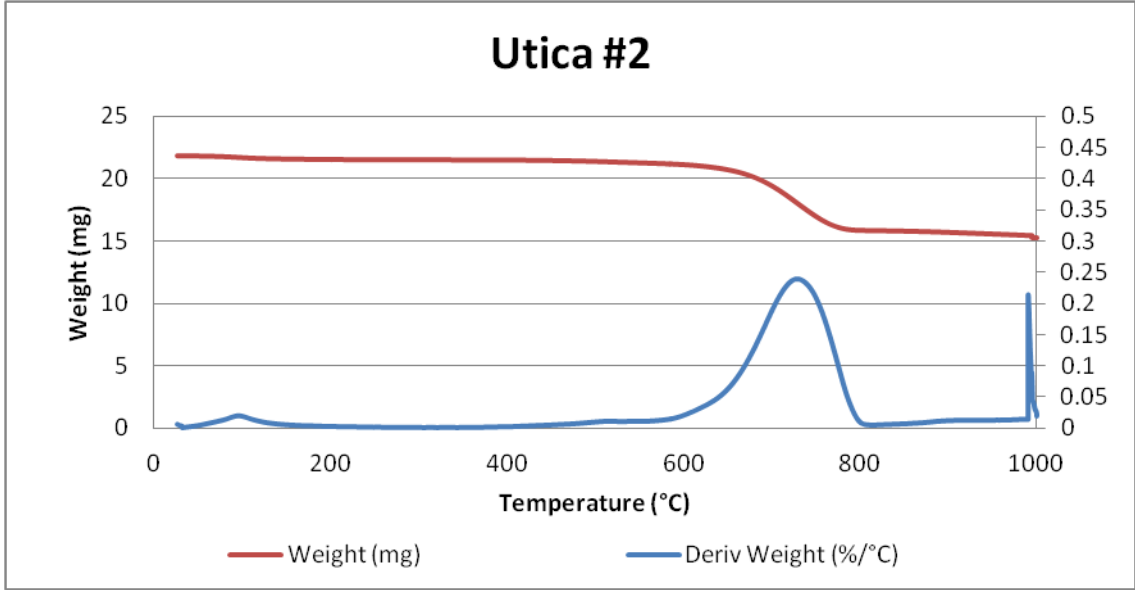
Figure 0.2: A) Kaolinite clay structure. B) Illite clay structure. C) Montmorillonite clay structure (after Das, 2012)

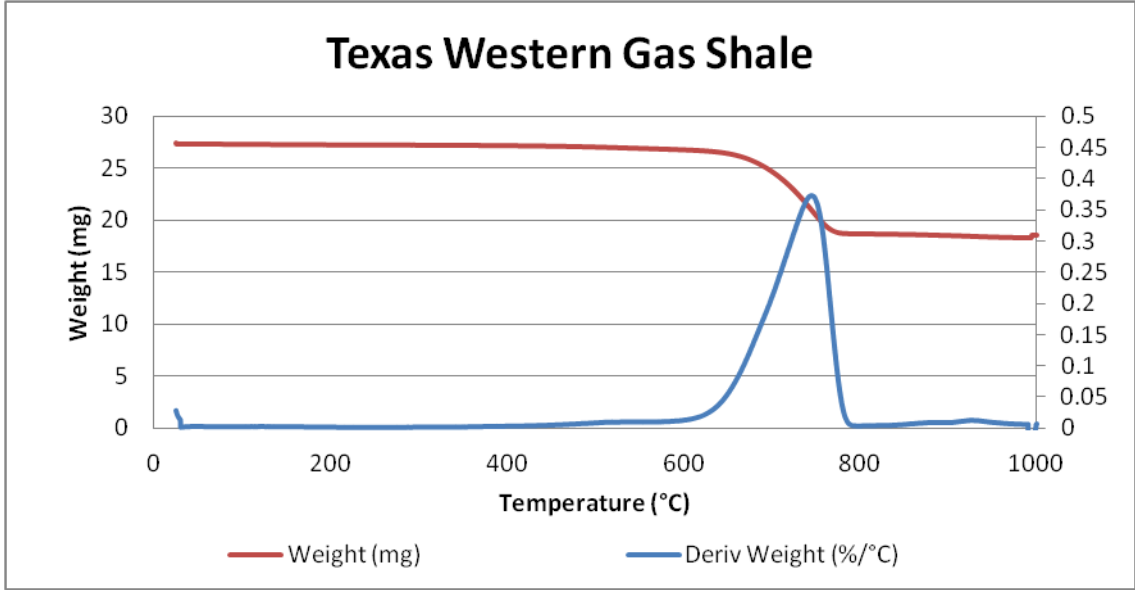
A3: TGA Results for All Shales



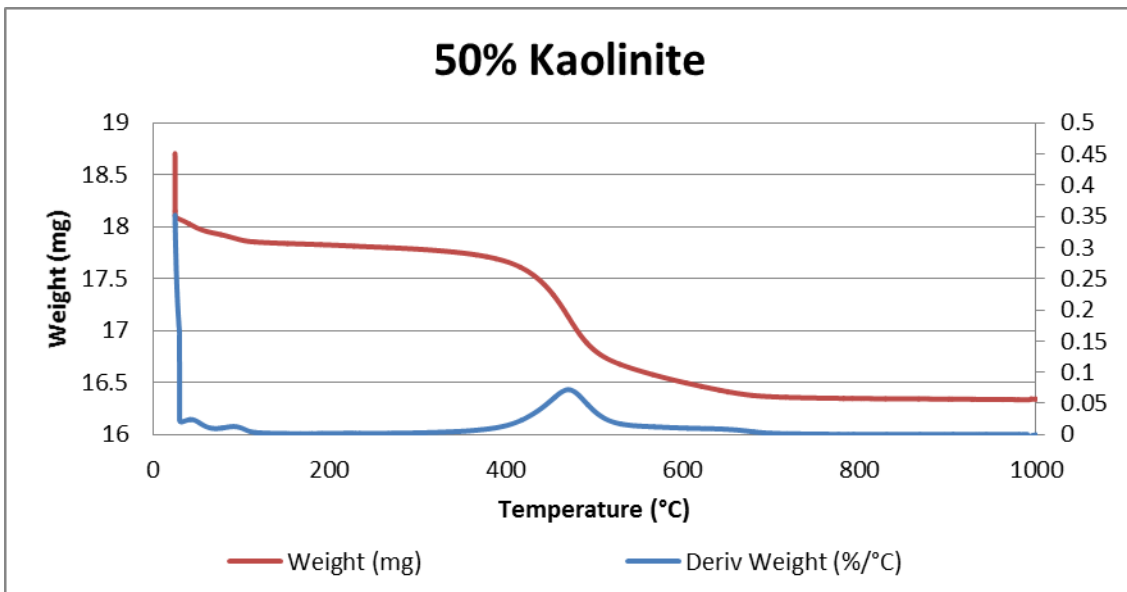
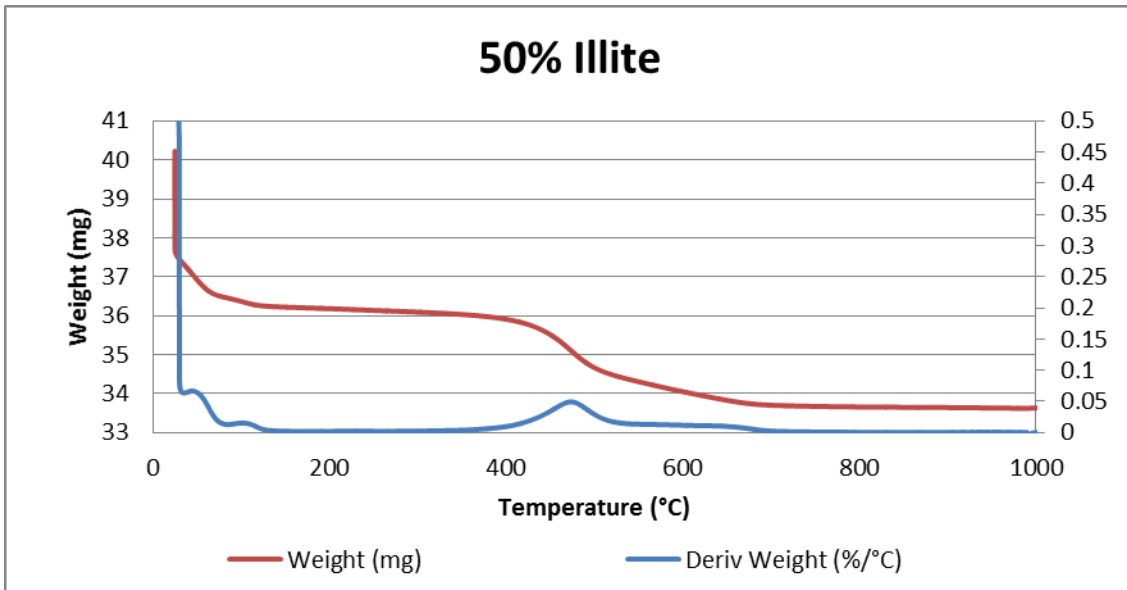


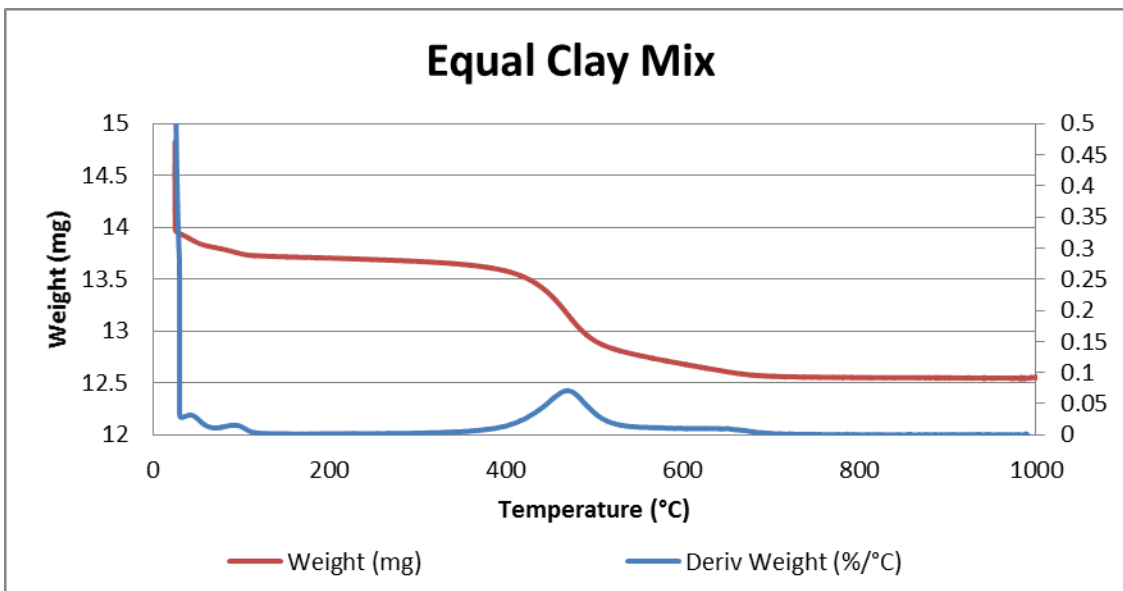
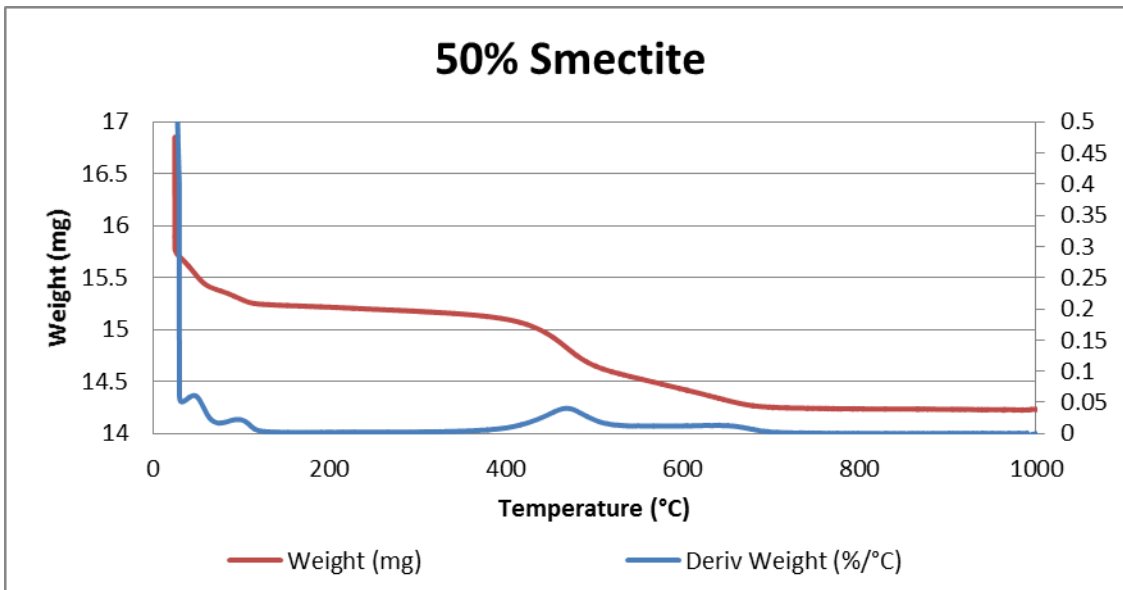






A4: TGA results for clay combinations





A5: NMR – Temperature Step T_1 & T_2 2D-Maps

Bakken

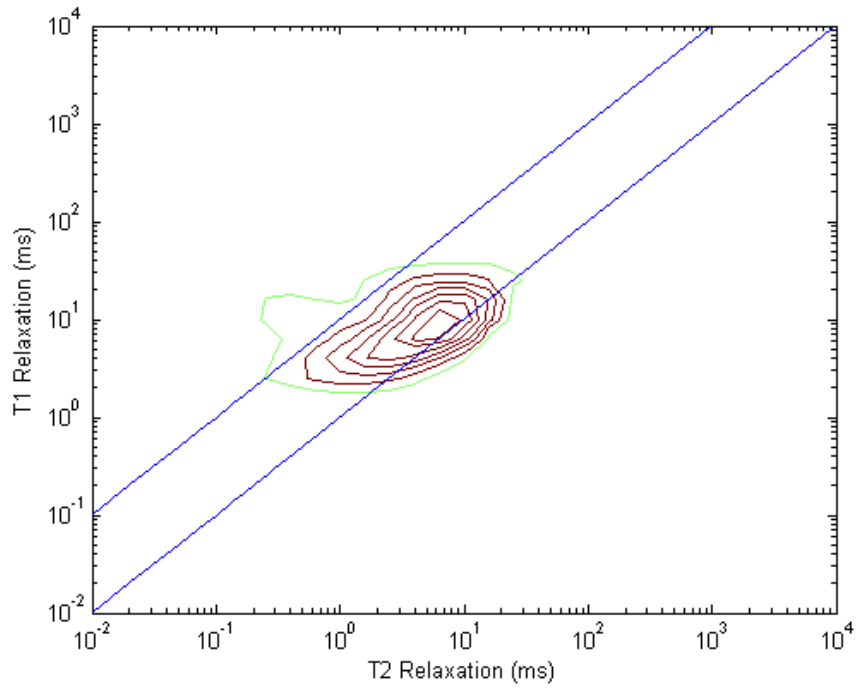


Figure 0.3: Simultaneous T₁ & T₂ 2D map of the Bakken sample after heating to 25°C

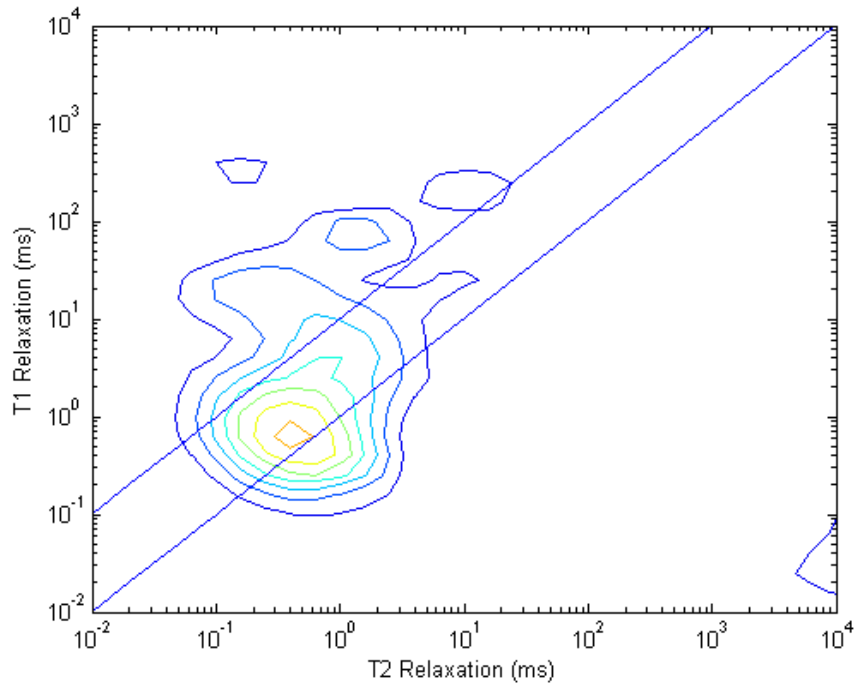


Figure 0.4: Simultaneous T₁ & T₂ 2D map of the Bakken sample after heating to 100°C

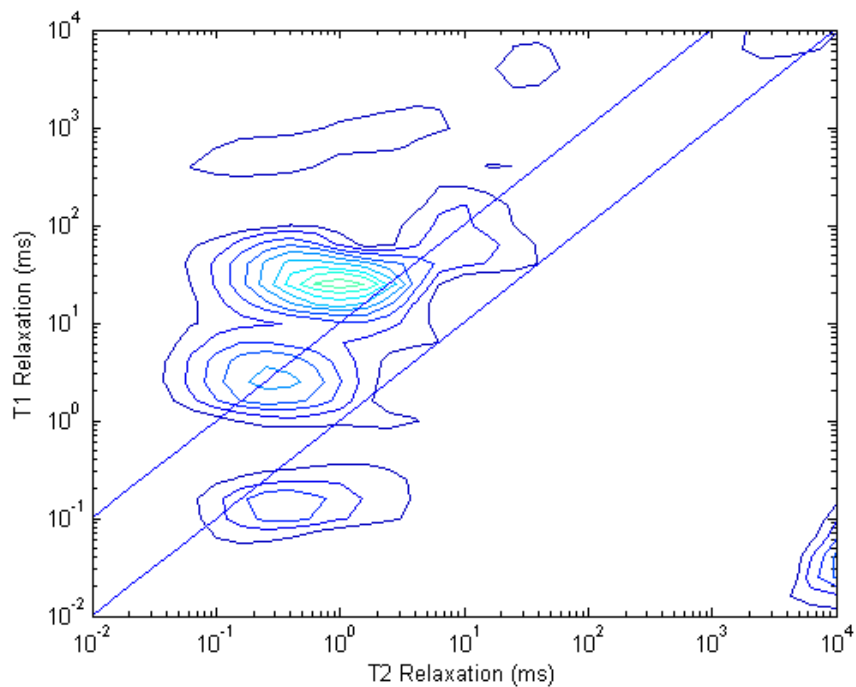


Figure 0.5: Simultaneous T1 & T2 2D map of the Bakken sample after heating to 200°C

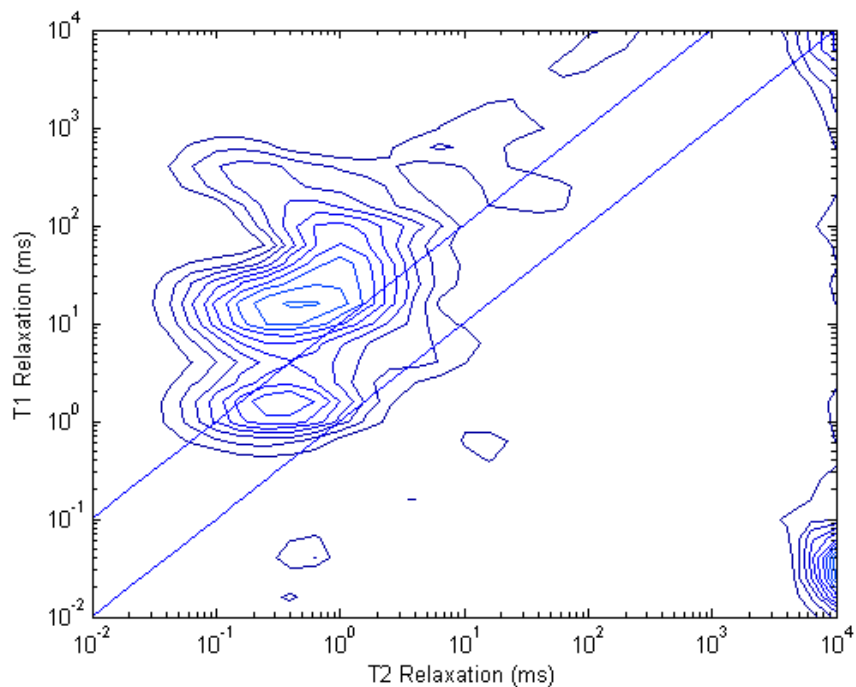


Figure 0.6: Simultaneous T1 & T2 2D map of the Bakken sample after heating to 580°C

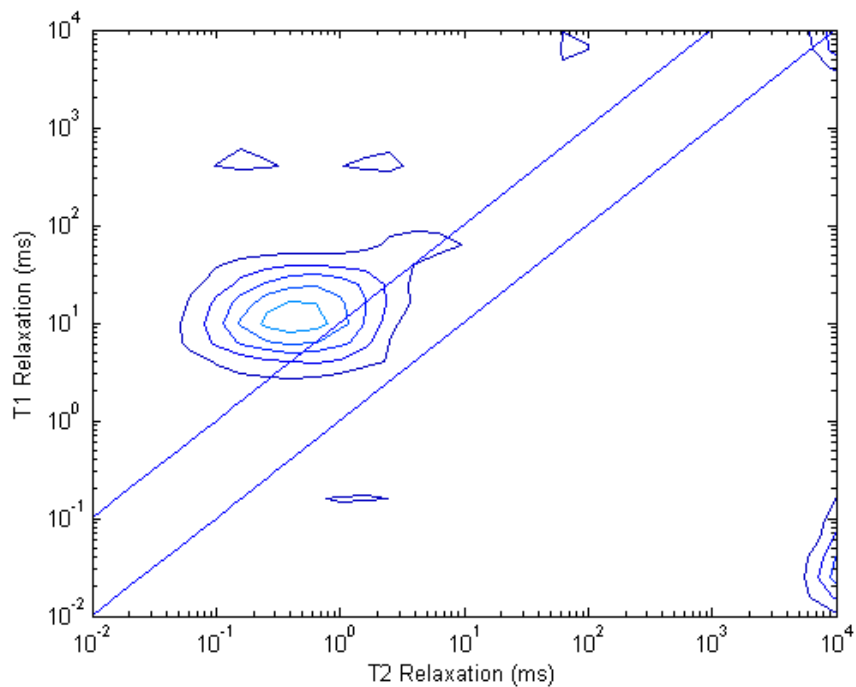


Figure 0.7: Simultaneous T1 & T2 2D map of the Bakken sample after heating to 800°C

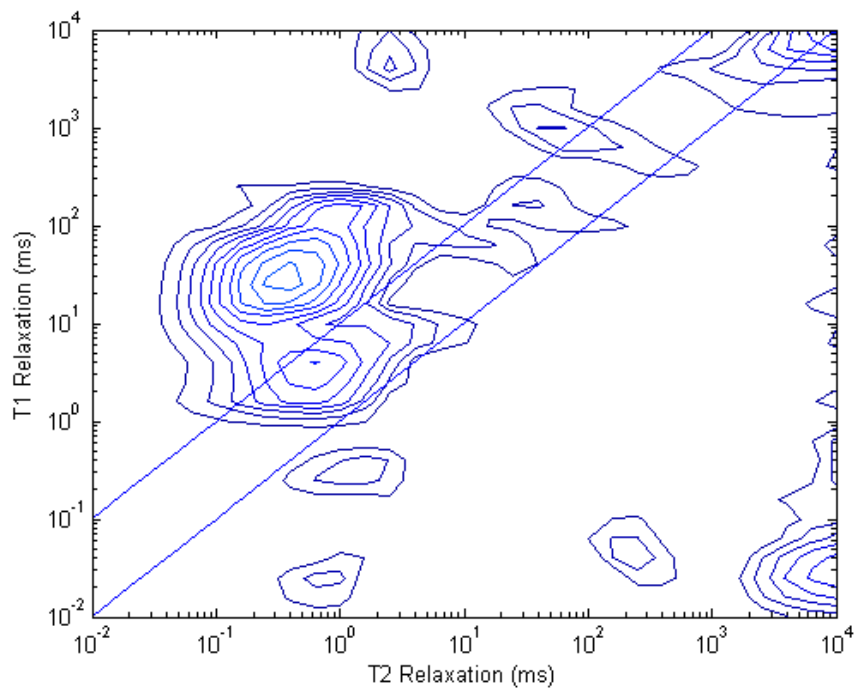


Figure 0.8: Simultaneous T1 & T2 2D map of the Bakken sample after heating to 1100°C

Eagle Ford

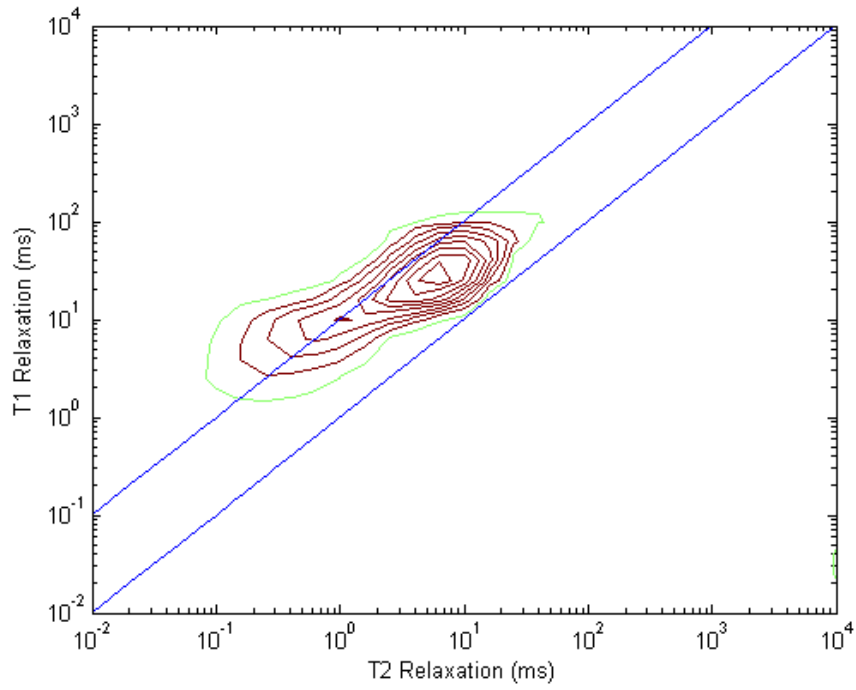


Figure 0.9: Simultaneous T1 & T2 2D map of the Eagle Ford sample after heating to 25°C

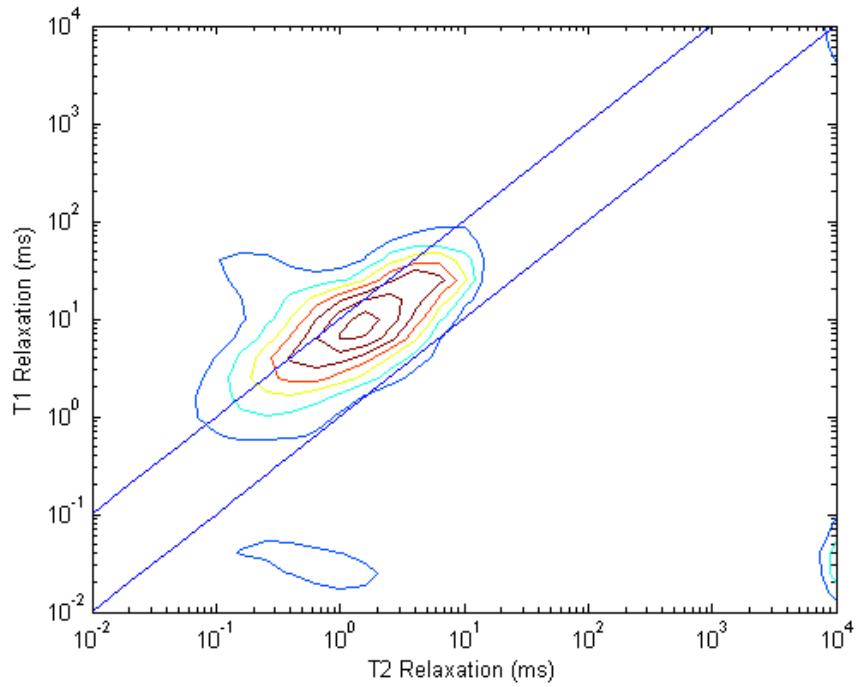


Figure 0.10: Simultaneous T1 & T2 2D map of the Eagle Ford sample after heating to 100°C

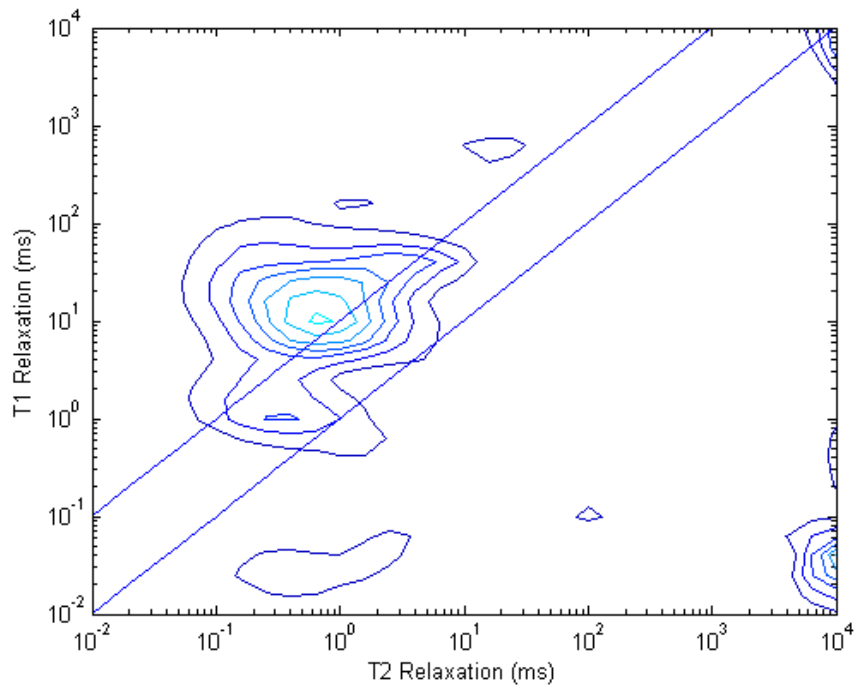


Figure 0.11: Simultaneous T1 & T2 2D map of the Eagle Ford sample after heating to 200°C

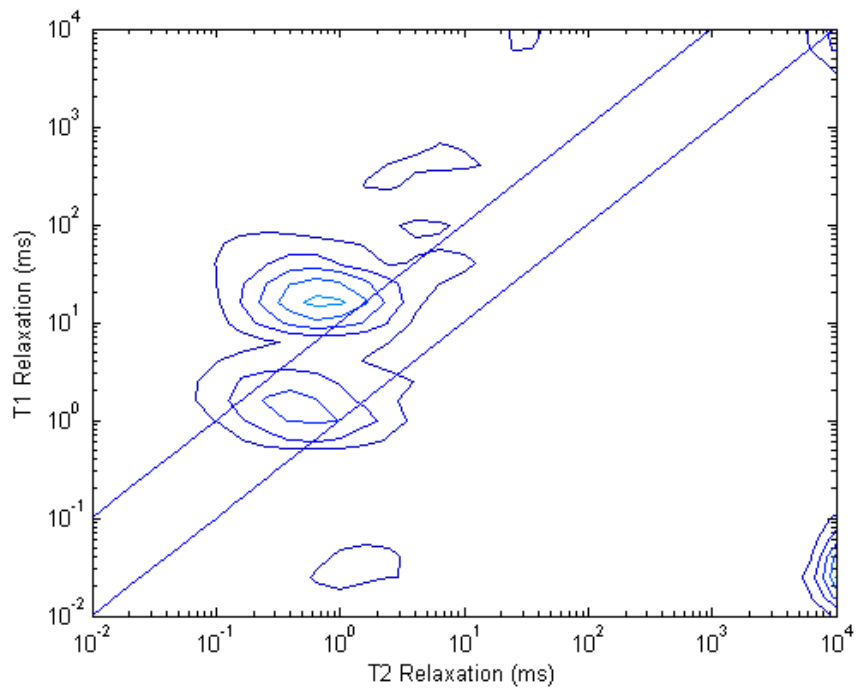


Figure 0.12: Simultaneous T1 & T2 2D map of the Eagle Ford sample after heating to 320°C

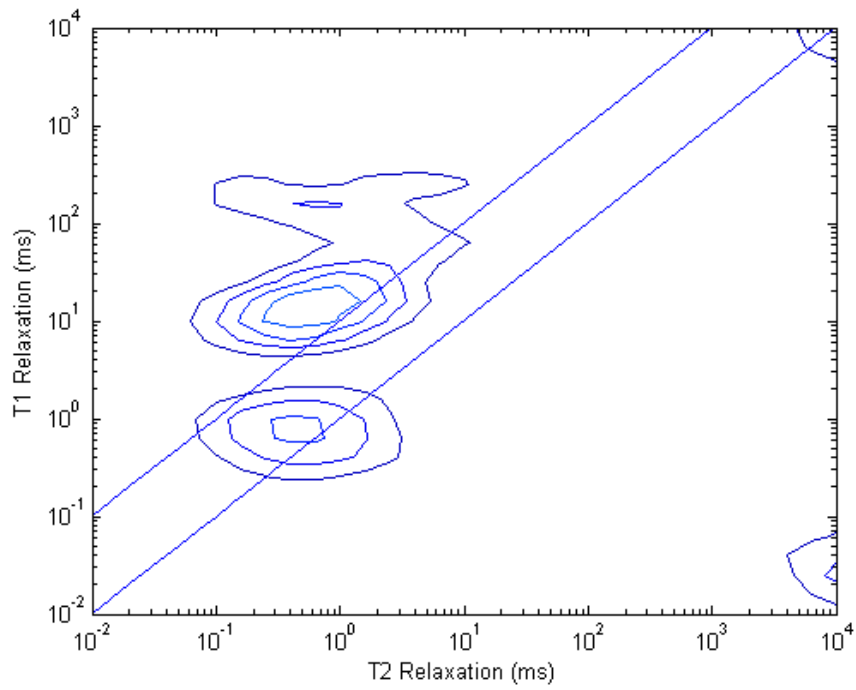


Figure 0.13: Simultaneous T1 & T2 2D map of the Eagle Ford sample after heating to 600°C

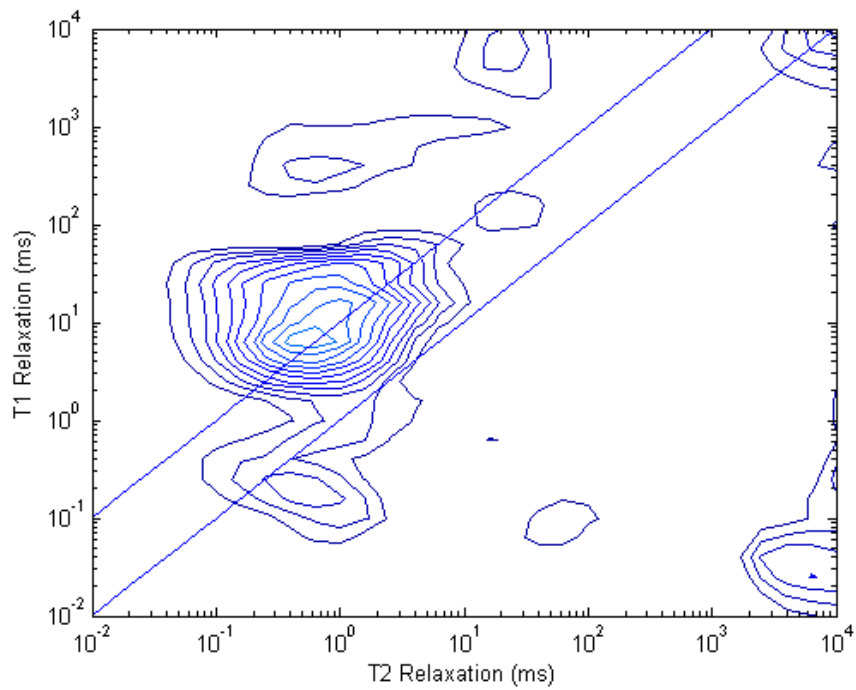


Figure 0.14: Simultaneous T1 & T2 2D map of the Eagle Ford sample after heating to 860°C

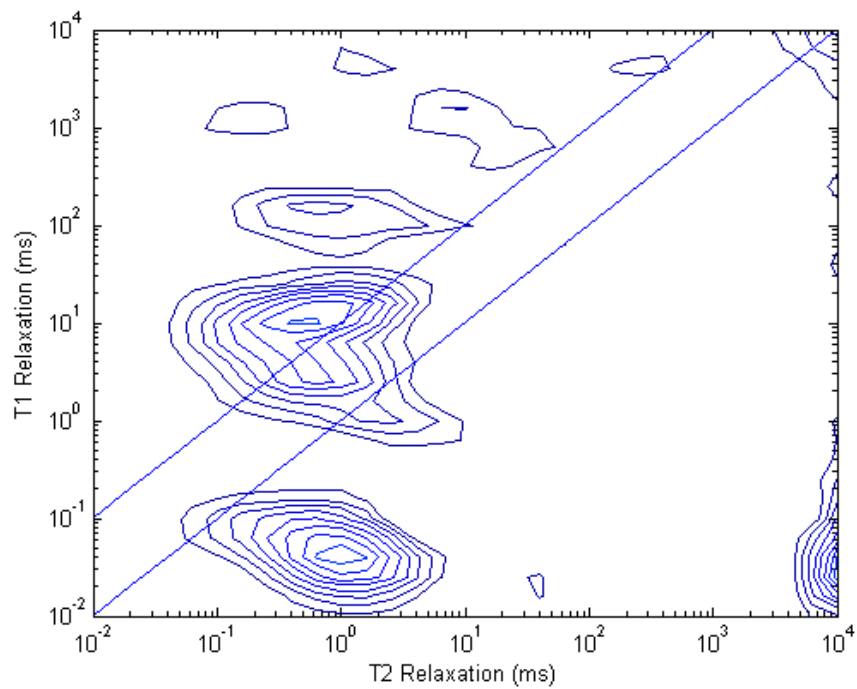


Figure 0.15: Simultaneous T1 & T2 2D map of the Eagle Ford sample after heating to 1100°C

Utica

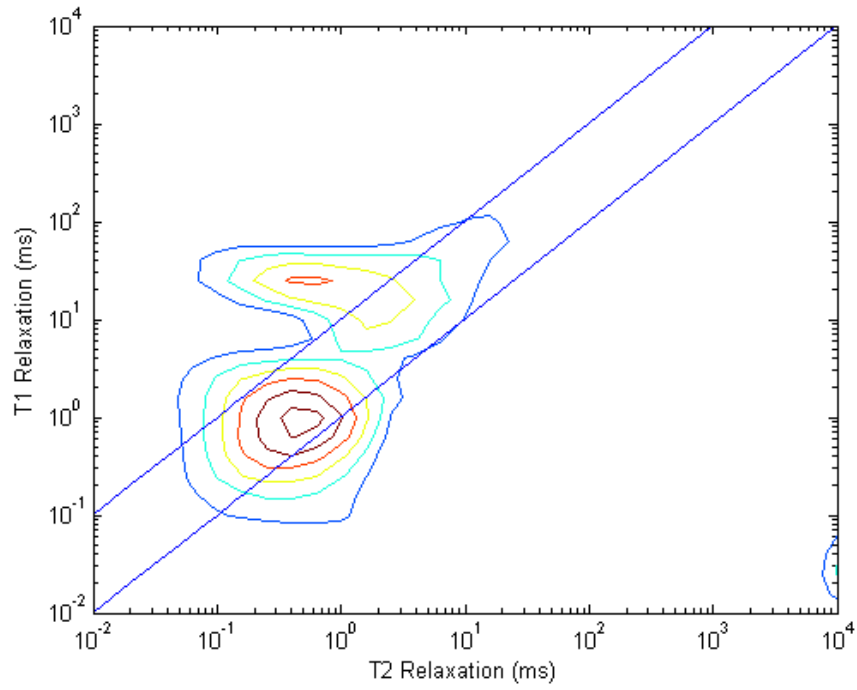


Figure 0.16: Simultaneous T1 & T2 2D map of the Utica sample after heating to 25°C

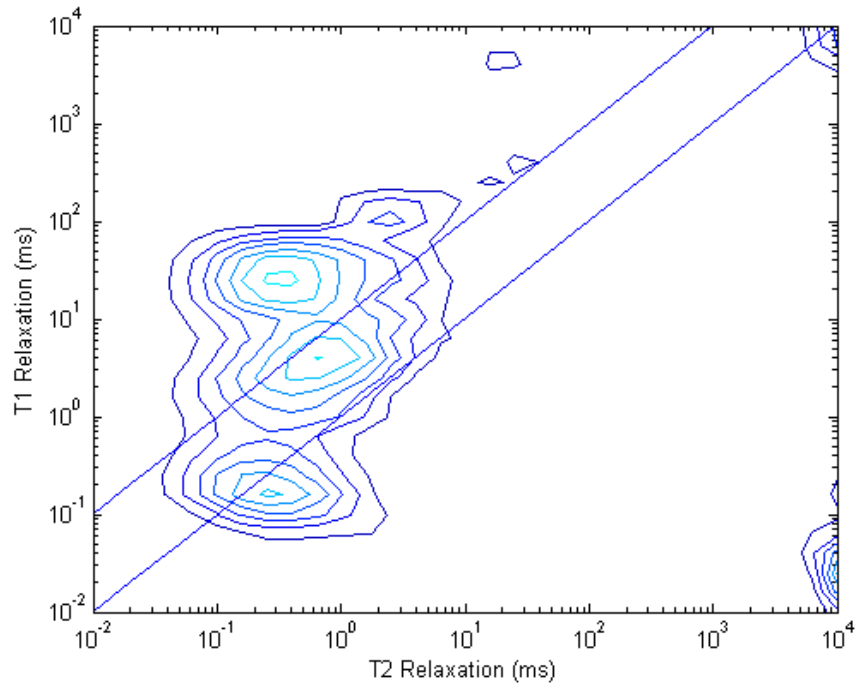


Figure 0.17: Simultaneous T1 & T2 2D map of the Utica sample after heating to 100°C

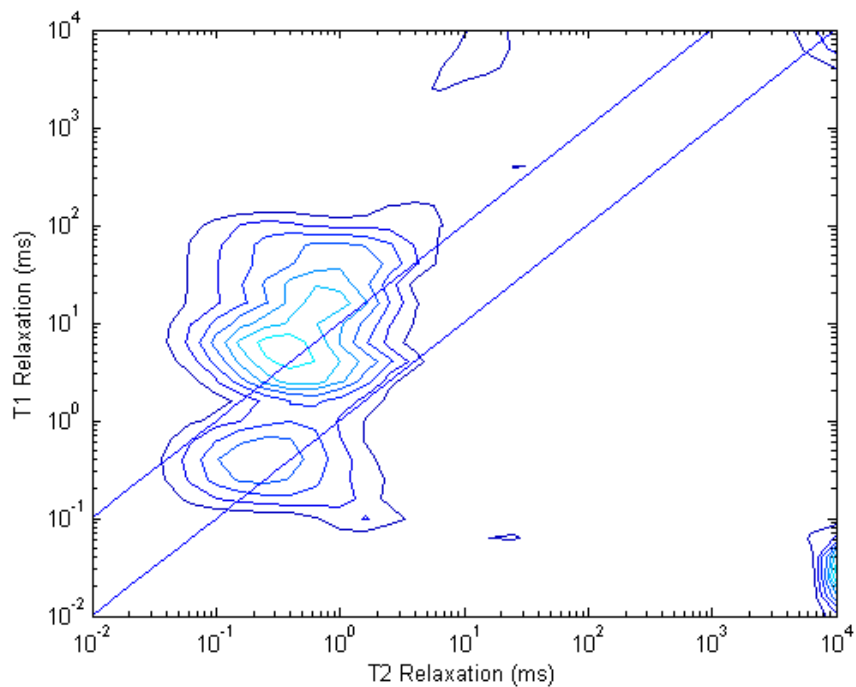


Figure 0.18: Simultaneous T1 & T2 2D map of the Utica sample after heating to 200°C

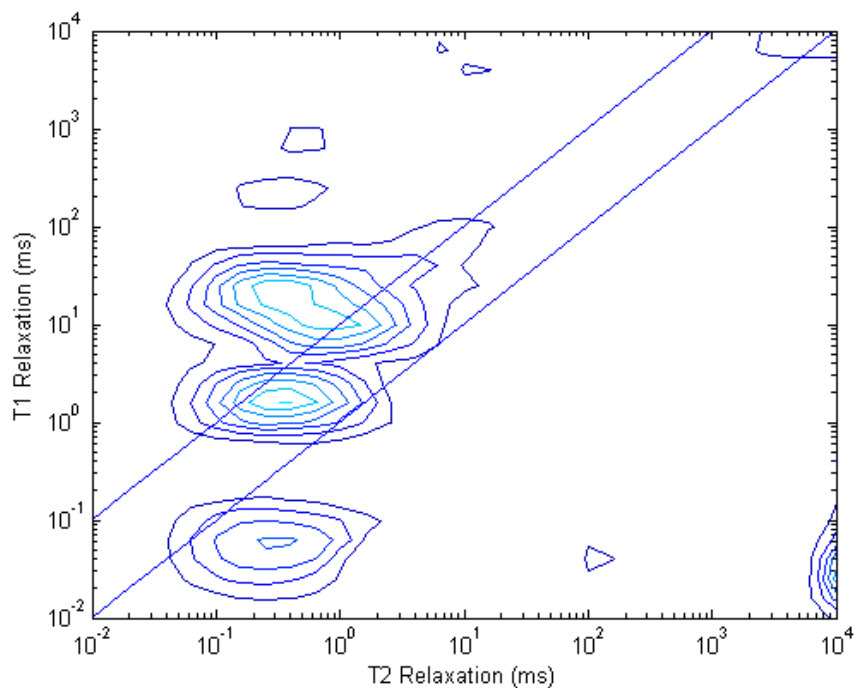


Figure 0.19: Simultaneous T1 & T2 2D map of the Utica sample after heating to 275°C

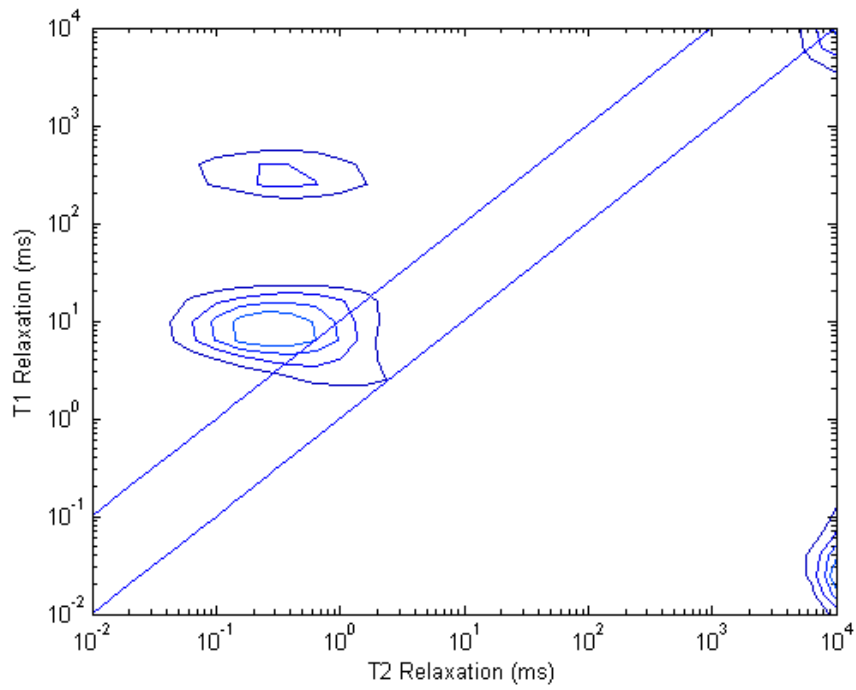


Figure 0.20: Simultaneous T1 & T2 2D map of the Utica sample after heating to 625°C

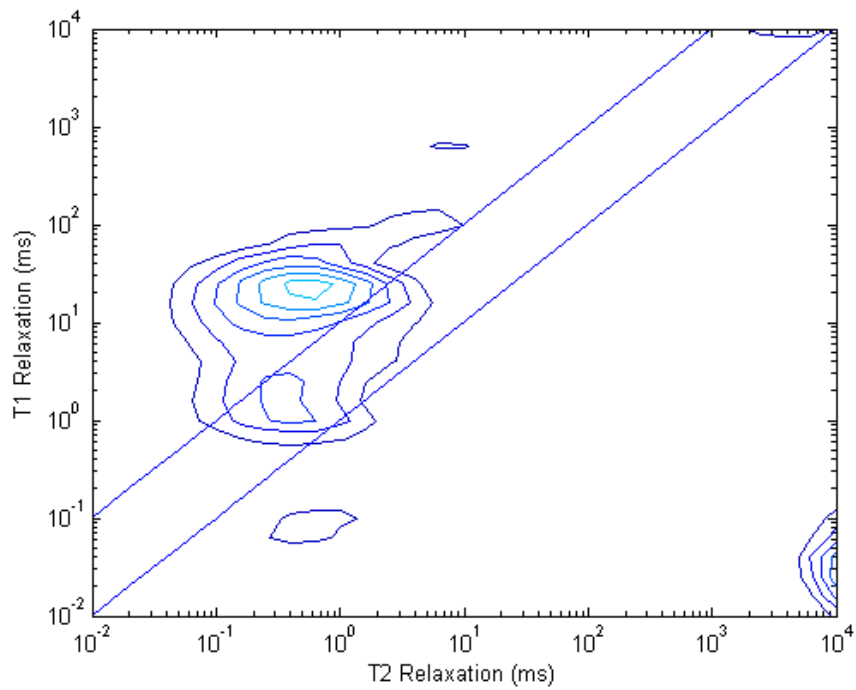


Figure 0.21: Simultaneous T1 & T2 2D map of the Utica sample after heating to 850°C

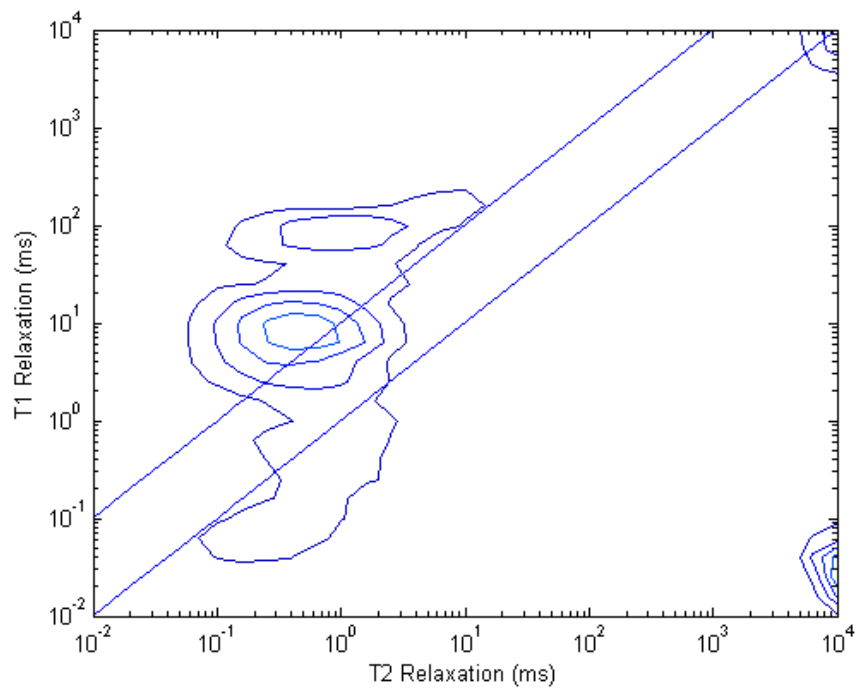


Figure 0.22: Simultaneous T1 & T2 2D map of the Utica sample after heating to 1100°C

References

- Bloembergen, N., Purcell, E.M., Pound, R.V. (1948). Relaxation effects in nuclear magnetic resonance absorption. *Physical Review*, 73(7), 679-712.
- Brownstein, K., Tarr, C. (1979). Importance of classical diffusion in NMR studies of water in biological cells. *Physical Review*, 19 (6), 2444-2456.
- Cao Minh, C., & Sundararaman, P. (2006). NMR Petrophysics in Thin Sand-Shale Laminations. SPE 102435. Presented at the Annual Technical Conference and Exhibition in San Antonio, TX. 24-27 September, 2006.
- Cao Minh, C., Zielinski, L., Liu, C.B., Jones, S., & Jacobsen, S. (2012). 2D-NMR Applications in Unconventional Reservoirs. SPE 161578. Presented at the SPE Canadian Unconventional Resources Conference in Calgary, AB. 30 October - 1 November, 2012.
- Coates, G.R., Xiao, L., & Prammer, M.G. (1999). NMR Logging Principles and Applications. *Halliburton Energy Services, Publication H02308, Ch 2-3*, 33-65.
- Daigle, H. (2013). NMR use for Formation Evaluation (Course Notes). University of Texas at Austin, Department of Petroleum and Geosystems Engineering. Notes taken November, 2013.
- Daigle, H., Johnson, A., Gips, J., Sharma, M. (2014) Porosity Evaluation of Shales Using NMR Secular Relaxation. SPE 1905272. Presented at the Unconventional Resources and Technology Conference in Denver, CO. 25-27 August, 2014.
- Das, B. (2012). *Fundamentals of Geotechnical Engineering*. Stamford, CT. Cengage Learning, 2012. *Google Books*. Accessed 14 September, 2014.
- Foley, I., Farooqui, S. A., Kleinberg, R. L. (1996). Effect of Paramagnetic Ions on NMR Relaxation Fluids at Solid Surfaces. *Journal of Magnetic Resonance*, 123 (1996), 95-104.
- Gips, J., Daigle, H., Sharma, M. (2014). Characterization of Shales Using NMR and Py-GC-MS. SPE 1917686. Presented at the Unconventional Resources and Technology Conference in Denver, CO. 25-27 August, 2014.
- Handwerger, D., Willberg, D. Pagels, M., Rowland, B., Keller, J. (2012). Reconciling Retort versus Dean Stark Measurements on Tight Shales. SPE 159976. Presented at the SPE Annual Technical Conference and Exhibition, San Antonio, Texas, 8-10 October, 2012.
- Kausik, R., Minh, C. C., Zielinski, L., Vissapragada, B., Akkurt, R., Song Y. Q., Liu, C.B., Jones, S., and Blaire, E. (2011). Characterization of gas dynamics in kerogen nanopores by NMR. SPE 147184. Presented at the SPE Annual Technical Conference and Exhibition, Denver, Colorado, 30 October - 2 November.
- Kenyon, W. E., Kolleeny, J. A. (1995). NMR Surface Relaxivity of Calcite with Adsorbed Mn²⁺. *Journal of Colloid and Interface Science*, 170 (1995), 502-514.
- Kleinberg, R.L., Horsfield, M. (1990). Transverse relaxation processes in porous sedimentary rock. *Journal of Magnetic Resonance*, 88, 9-19.
- Loucks, R., Reed, R., Ruppel, S., Jarvie, D. (2009). Morphology, genesis, and distribution of nanometer-scale pores in silicious mudstones of the Mississippian Barnett Shale, *Journal of Sedimentary Research*, 79, 848-861.

- Matteson, A., Tomanic, J.P., Herron, M.M., Allen, D.F., & Kenyon, W.E. (2006). NMR Relaxation of Clay/Brine Mixtures. *SPE Reservoir Evaluation and Engineering*, 3 (2006), 408-413.
- Oduşina, E., Sondergeld, C., Rai, C. (2011). An NMR Study on Shale Wettability. SPE 147371. Presented at the Canadian Unconventional Resources Conference, Calgary, Alberta, Canada, 15-17 November, 2011.
- Rylander, E., Singer, P. M., Jiang, T., Lewis, R. (2013). NMR T₂ Distributions in the Eagleford Shale: Reflections on Pore Size. SPE 164554. Presented at the SPE Unconventionals Resources Conference in The Woodlands, TX. 10 April – 12 April, 2013
- Santos, H., Gupta, A. (1997). Application of Thermal Analysis to Characterize Clay-Rich Formations. Presented at the Petroleum Conference of the South Saskatchewan Section of the Petroleum Society of CIM, Regina, SK, Canada. 19-22 October, 1997
- Tissot, B., Welte, D. (1984). *Petroleum Formation and Occurrence*, 2 ed. New York, Springer-Verlag. p 699.
- Washburn, K. E., & Birdwell, J.E. (2013). Updated methodology for nuclear magnetic resonance characterization of shales. *Journal of Magnetic Resonance*, 233 (2013), 17-28.
- Washburn, K., & Birdwell, J. (2013). A New Laboratory Approach to Shale Analysis Using NMR Relaxometry. Society of Petroleum Engineers. Presented at the Unconventional Resources Technology Conference, Denver, Colorado, 12-14 August, 2013.
- Zhou, J., Jung, C., Chenevert, M., Sharma, M. (2013). Petrophysical Characterization of Organic-Rich Shales: A New Standardized Protocol. ARMA 13-546. Presented at the U.S. Rock Mechanics / Geomechanics Symposium, San Francisco, California, 23-26 June, 2013.